Abstracts of the Annual Meeting of Planetary Geologic Mappers, Washington, DC, 2013

Edited by:

James A. Skinner, Jr.
U. S. Geological Survey, Flagstaff, AZ

David Williams
Arizona State University, Tempe, AZ

NOTE: Abstracts in this volume can be cited using the following format:

Graupner, M. and Hansen, V.L., 2013, Structural and Geologic Mapping of Tellus Region, Venus, *in* Skinner, J.A., Jr. and Williams, D. A., eds., Abstracts of the Annual Meeting of Planetary Geologic Mappers, Washington, DC, June 19-21, 2013.

SCHEDULE OF EVENTS

Wednesday, June 19 – Planetary Geologic Mappers Meeting

Time	Planet/Body	Topic
8:30 am		Arrive – 6th Street SW and Independence Ave SW
9:00		Welcome/Logistics
9:15		USGS Map Coordinator Remarks (K. Tanaka)
9:30		NASA HQ and Program Remarks (M. Kelley)
9:45		GIS and Web Updates (T. Hare)
10:00	Mercury	*Caloris Basin* (D. Buczkowski)
10:20	Venus	*Beta-Atla-Themis (BAT) region* (L. Bleamaster)
10:40	Moon	*LQ-29* (A. Yingst)
11:00	Moon	*LQ-30* (S. Mest)
11:20		POSTER VIEWING / DEPART FOR METEORITE TOUR
12:00 pm		LUNCH
1:00		POSTER VIEWING
2:30	Mars	*Nili Fossae: Possible Hot Springs?* (MESDT – Grosse Pointe)
2:40	Mars	*MSL Landing Ellipse* (F. Calef)
3:00	Mars	*Global Map, etc.* (K. Tanaka)
3:20	Mars	*Highland Resurfacing* (R. Irwin)
3:40		GROUP DISCUSSION
5:00		ADJOURN

Thursday, June 20 – Planetary Geologic Mappers Meeting

Time	Planet/Body	Topic
8:30		Arrive – 6th Street SW and Independence Ave SW
9:00	Mars	*Uzboi Vallis* (S. Wilson)
9:20	Mars	*Runanga-Jörn* (J. Skinner)
9:40	Mars	*Aeolis Dorsa* (R. Jacobsen)
10:00	Mars	*Terra Sirenum* (B. Anderson)
10:20		POSTER VIEWING
10:40	Mars	*Olympus Mons* (J. Bleacher)
11:00	Mars	*Arsia/Pavonis Montes* (B. Garry)
11:20	Mars	*MTM -35137* / *Daedalia Planum* (D. Crown)
11:40		POSTER VIEWING
12:00 pm		LUNCH (GEMS meeting)
1:00		POSTER VIEWING
1:30	Mars	*Nili Fossae: Methane Plumes* (MESDT – Kickapoo)
1:40	Mars	~~*Argyre basin* (J. Dohm)~~
2:00	Mars	*Huygens Crater Mineralogy* (S. Ackiss)
2:20	Vesta	*Numisia Quad (Av-9)* (D. Buczkowski)
2:40	Europa	*Global Map* (M. Bunte)
3:00		POSTER VIEWING
3:30		GROUP DISCUSSION
5:00		ADJOURN

Friday, June 21 – GIS Roundtable

Time	Topic
8:30	Arrive – 6th Street SW and Independence Ave SW
9:00 am to 4:00 pm	GIS Potpourri (email requested topics to Trent Hare: thare@usgs.gov)

CONTENTS *(sorted by body, then alphabetically by author)*

Print Only

GEOMORPHIC MAPPING OF THE CALORIS BASIN, MERCURY. D.L. Buczkowski, S. Edrich and K.D. Seelos, Johns Hopkins University Applied Physics Laboratory, Laurel, MD 20723, Debra.Buczkowski@jhuapl.edu.

Introduction: Two Mercury quadrangles based on Mariner 10 data cover the Caloris basin (Fig. 1): H-8 Tolstoj [1] and H-3 Shakespeare [2]. The dark annulus identified in MESSENGER data corresponds well to the mapped location of certain formations [3], primarily the Odin Formation. The Odin Formation is described in the quadrangle maps as a unit of low, closely spaced knobs separated by a smooth, plains-like material and was interpreted as ejecta from the Caloris impact. Schaber and McCauley [1980] observed that the intra-ejecta plains in the Odin Formation resemble the Smooth Plains unit that was also prevalent in the H-8 and H-3 quadrangles outside of Caloris. They state that these plains were included as part of the Odin Formation for mapping convenience, not because they necessarily shared the same formation mechanism.

Crater counts based on MESSENGER imagery indicate that the Odin intra-ejecta plains are younger than the Caloris floor plains within the basin [4,5]. This is inconsistent with the intra-ejecta plains being Caloris ejecta but is consistent with the plains being fingers of the smooth plains unit embaying the Odin ejecta knobs.

However, the intra-ejecta plains are not the same color as the smooth plains in Mercury Dual Imaging System (MDIS) data [3]; while the smooth plains are bright, the intra-ejecta plains are the same dark color as the ejecta knobs. A possible explanation is that the Odin knobs and intra-ejecta dark plains represent two facies of dark basement material excavated by the Caloris impact. Alternately, the intra-ejecta plains could represent a dark volcanic flow, distinct from the bright smooth plains volcanic flow; however, it would have to be a volcanic flow restricted to a region circumferential to the basin. A third possibility is that the intra-ejecta dark plains are a pre-Caloris smooth material (possibly the Intercrater Plains unit) darkened by a thin layer of superposed dark Odin material.

This abstract outlines the progress associated with a new mapping project of the Caloris basin and its associated intra-ejecta plains, intended to improve our knowledge of the geology and geologic history of the basin, and thus facilitate an understanding of the thermal evolution of this region of Mercury.

Previous Caloris basin mapping: A detailed analysis of the Odin Formation performed by [5] noted that the unit is easily recognizable circum-Caloris in the MESSENGER data and concluded that the Odin Formation knobs are Caloris ejecta blocks that have been mostly embayed and buried by younger volcanic deposits. They found that MDIS color data supported this hypothesis and divided the formation into two subunits: knobby plains and smooth plains. However, recent work by [6] suggests that there is still no definitive proof that the Odin-style plains have either an impact or volcanic origin.

High-resolution mapping of the intra-ejecta dark plains: We use high resolution imaging data from the MDIS instrument to create our geomorphic map of the Caloris basin, particularly the dark annulus around the basin (Fig. 2). We utilize a principle component map [3] to distinguish subtle differences in the color data. In the principle component map green represents the second principle component (PC2), which reflects variations between light and dark materials. Meanwhile, red is the inverted PC2 and blue is the ratio of normalized reflectance at 480/1000 nm, which highlights fresh ejecta.

We map all contacts between bright and dark materials within the intra-ejecta plains, as determined in the principle component map, as sub-units of the Odin Formation (Fig 3a). All knobs are mapped individually and their color (either dark or bright) is noted (Fig 3b). Ejecta blankets from local craters (both extent and color) are mapped separately (Fig 2a).

All craters are mapped according to a newly devised crater classification scheme. The crater classification used in the Tolstoj and Shakespeare quadrangles [1,2] and formalized in 1981 [7] was based on degree of crater degradation. Our classification scheme includes both degradation state and level and type of infilling. Current classifications include: 1) blue and pristine, 2) fresh but not blue, 3) intact rim and superposed, 4) intact rim and embayed, 5) degraded rim and superposed, 6) degraded rim and embayed, 7) very degraded and superposed, 8) very degraded and embayed and 9) little to no rim.

Observations: The Odin Formation shows two distinct sub-units: a dark sub-unit and a (relatively) bright sub-unit. The dark sub-unit has a higher concentration of knobs, knobs that are both bright and dark and craters that are both embayed and superposed. Meanwhile, the bright sub-unit has a lower concentration of knobs, knobs that are predominantly bright and craters that are fresh and/or superposed. Outcrops of the bright material can be associated with crater ejecta blankets, but are not always.

Crater counts on dark and bright sub-units may be affected by the relatively small size of craters (< 20 km). Work by [8] indicates that secondary craters on Mercury can be as large as 25 km. However, the observation that dark sub-unit craters encompass all crater classifications while bright sub-unit craters are almost uniformly fresh and superposed does imply that the bright sub-unit is younger.

References: [1] Schaber and McCauley (1980) USGS Map I-1199 [2] Guest and Greeley (1983) USGS Map I-1408 [3] Murchie et al (2008) *Science 321*, 73-76 [4] Strom et al (2008) *Science 321*, 79-81 [5] Fasset et al (2009) *Earth Planet. Sci Lett 285*, 297-308 [6] Denevi et al (2013) *JGR* doi:10.1002/jgre.20075 [7] McCauley et al (1981) *Icarus 47*, 184-202 [8] Strom et al (2011) LPSC abs 1079

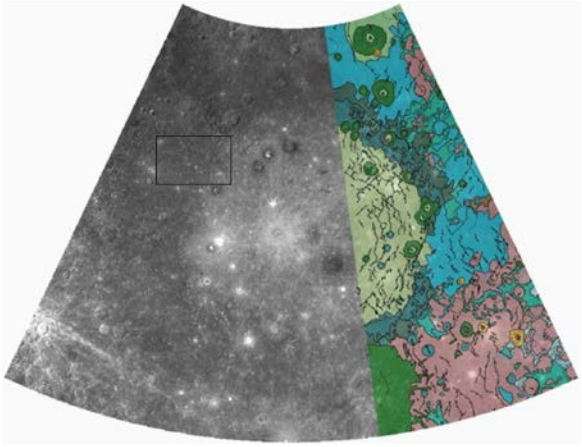

Figure 1. MESSENGER mosaic of the Caloris basin overlain by portions of the H-8 Tolstoj [1] and H-3 Shakespeare [2] quadrangles. Odin Formation is light blue; Smooth Plains are pink. Black box indicates location of Figure 2.

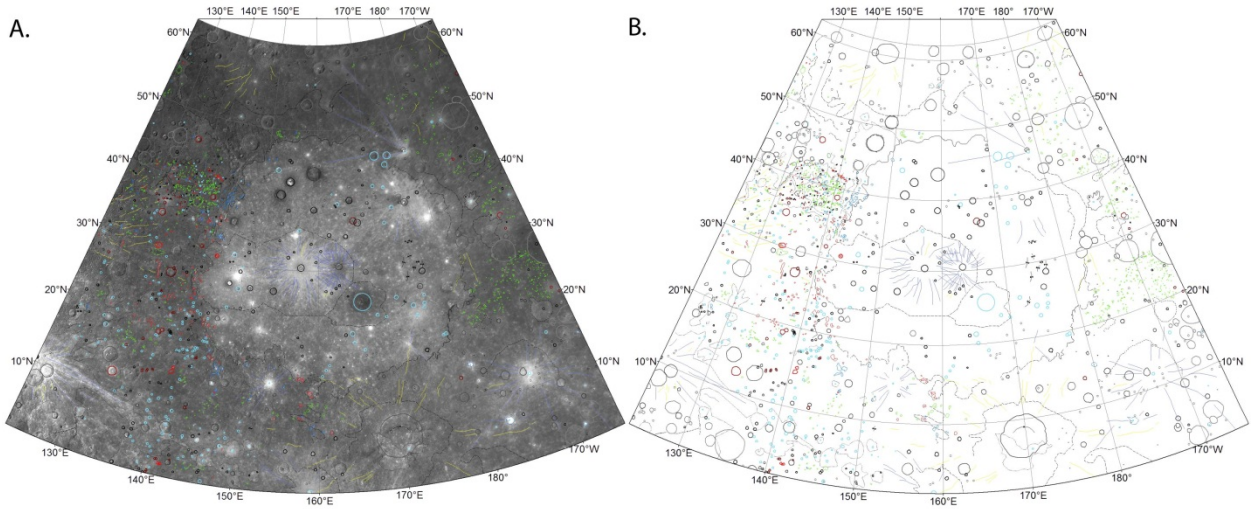

Figure 2. Geomorphic map of the Caloris basin, both over the MESSENGER mosaic (A) and without the background image (B).

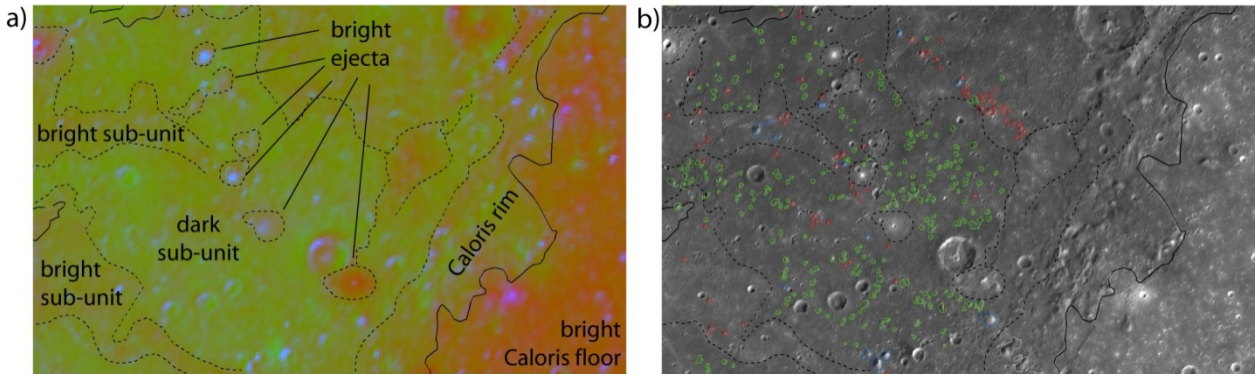

Figure 3. Part of Caloris dark annulus used as Odin Formation example in [5]. a) Principle component map, to demonstrate how bright and dark sub-units were mapped. Sub-units are labeled. b) Odin Formation knobs, shown with sub-unit contacts (dashed lines). Green knobs are dark in the MDIS principle component map; red are light. Note that the majority of knobs are identified in the dark sub-unit.

GEOLOGIC MAPPING OF THE BETA-ATLA-THEMIS (BAT) REGION OF VENUS. Leslie F. Bleamaster III[1,2], [1]Planetary Science Institute, 1700 E. Ft. Lowell Rd., Suite 106, Tucson AZ, 85719; [2]Trinity University Geosciences Department, One Trinity Place #45, San Antonio TX, 78212. (lbleamas@trinity.edu)

Introduction: The Beta-Atla-Themis (BAT) province is of particular interest with respect to evaluating Venus' geologic, tectonic, and volcanic history and provides the opportunity to test global paradigms regarding her thermal evolution. The BAT is "ringed" by three extensive volcano-tectonic troughs (**P**arga, **H**ecate, and **D**evana Chasmata), has an anomalously high-density of volcanic features with concentrations 2-4 times the global average [1], and is spatially coincident with relatively "young terrain" as illustrated by Average Surface Model Ages [2, 3]. The BAT province is key to understanding Venus' relatively recent volcanic and tectonic modes and may even contain sites of active volcanism, proposed by Dombard et al., [4] based on geophysical modeling and Smrekar et al., [5] based on Venus Express emissivity anomalies. Geologic mapping of the BAT is constraining the geologic and temporal relations of 100s of volcano-tectonic centers along the BAT's three major rift zones providing new insight into this relatively young setting. Mapping will also test the pseudo-coronae hypothesis [6] that states that lithospheric, and more importantly, crustal thickness variability plays and important role in the general spatial distribution of coronae as well as the spatio-temporal association of coronae and chasmata.

Mapping efforts include the construction of two 1:10,000,000 scale quadrangles that cover the entire BAT province – Guinevere Planitia (I-2457) in the north and Helen Planitia (I-2477) to the south (Figure 1a). The two mapping quadrangles have been merged into one ArcGIS geodatabase and a regional framework is being developed.

Helen Planitia (I-2477; 0-57°S/180-300°E) covers over 70 million square kilometers (approximately 1/8th) of the surface of Venus and contains the full length of the Parga Chasmata (~10,000 km long), which connects Atla Regio in the west to Themis Region in the east. Along its length are several hundred radial and circular structures and their associated digitate and lobate flows.

The majority of these radial/circular features lie within a few hundred kilometers of the Parga Chasmata rift system marking a southeast trending line of relatively young volcano-tectonic activity. Although some very localized embayment and crosscutting relationships display clear relative age relations between centers of activity and their flows, the majority of Parga Chasmata volcanism and tectonism overlaps in time along its length [7,8].

Four particular coronae: Maram (600 km), Atete (600 km), Kulimina (170 km), and Shiwanokia (500 km) display unique morphologic characteristics and map relations suggesting extremely youthful, possibly current, activity. Characteristics include superposing flows of hundred kilometers in length, fractures and faults that trend parallel to Parga Chasmata suggesting they post-date the main rift, and relatively high topographic relief with steep concentric bounding scarps [8].

Of particular interest is the correlation between the mapping relations of these particular coronae and geophysical analyses by Dombard et al. [4], which indentified these four coronae as "active." The four coronae are distributed (a few hundred to thousands of kilometers apart) along the central axis of Parga Chasmata suggesting that if these coronae do represent current volcanism and tectonism, that activity is spread out along the central axis of the chasmata and not focused at one end or the other.

Guinevere Planitia (I-2457; 0-57°N/180-300°E) covers an equally large proportion of the planet in the northern hemisphere. Atla and Beta Regiones mark the west and northern apices of the BAT triangle and are connected by discontinuous topographic troughs made up of **Z**evana (~1000 km), **H**ecate (~3200 km), and **L**atona (~550 km) Chasmata. Collectively, these chasmata along with their associated coronae and mons define a diffuse volcano-tectonic zone comparable to Parga Chasmata in the south, but perhaps to a less evolved state [8] as suggested by the chasmata's less integrated structure.

The degree to which coronae and chasmata are related and the nature of these volcano-tectonic rift zones remains elusive. However, local geologic studies within Guinevere Planitia, like in Helen Planitia, reveal geomorphic and structural features indicating relatively youthful activity. The Dombard et al. [4] work proposed three candidate sites of current activity in the north. Although, correlations between mapping relations and modeling are not a strong as in the south, two of the three proposed sites display similar morphologic and topographic characteristics, as well as locally young flows (Aruru and Zisa Coronae). The third site, an unnamed volcano-tectonic center of ~150 km diameter, rests in the middle of Žverine Chasma (a location consistent with the postulate that contemporary activity will be centered along the rift axis).

Devana and Rona Chasmata form a deformational belt along the eastern BAT that begins north of Beta Regio (in the Guinevere quad), extends south through Phoebe Regio, and ends near the northern edge of Themis Regio (in the Helen quad) (Figure. 1a). Kiefer and Swafford [9] proposed that Devana was a discontinuous rift by gravity analysis and lithospheric extension measurements. The slight bend seen along the study section in the rift (Figure 1b) was selected as an offset region connecting two distinct rift arms from the north and the south respectively. Detailed structural

mapping, including the locations and structural density of major fault systems, chasmata, and the distribution of coronae and pseudo-coronae confirms a morphologic difference between Devana and **Rona** Chasmata (**accepted new name, IAU 2012**). With two propagating rifts, three possible formation scenarios arise: the two legs were either formed synchronously; the northern leg formed first; or the southern leg formed first. Mapping of Devana/Rona Chasma overlap section supports the third scenario of rift development (Figure 1b). This conclusion, by proxy, supports the conclusion that activity associated with Beta Regio in the north is younger than rifting from the south in Pheobe Regio.

Future: These locations present ideal targets of opportunity for any future mission designed to investigate Venus' operative modes of volcanic resurfacing and tectonic activity. Increases in topographic and gravity field resolution would help constrain age determinations between rifting and volcanism; greater emissivity sensitivity, resolution, and coverage would improve detection of anomalously high or low thermal emission related to temperature or composition; and repeat path interferometric SAR may directly detect changes of the ground surface.

References: [1] Head et al., (1992) *J. Geophys. Res., 97(E8)*, 13,153-13,197. [2] Phillips, R.J. and Izenberg, N.R. (1995) *Geophys. Res. Lett., 22,* 1517-1520. [3] Hansen, V.L. and Young, D.A. (2007) *GSA Special Paper 419,* 255-273. [4] Dombard et al., (2007) *J. Geophys. Res., 112,* E04006, doi:10.1029/2006 JE002731. [5] Smrekar, S.E. et al., (2008) *EOS Trans. AGU, Fall Meet. Suppl.* 89, P22A-03 [6] Bleamaster III, L.F. and Hansen, V.L. (2004) *J. Geophys. Res., 109,* E02004, doi:10.1029/2003JE002193. [7] Bleamaster III, L.F. (2008), *Ann. Meet. Planet. Geo. Maps.* NASA/CP-2008-215469 [8] Bleamaster III, L.F. (2007) *LPSC XXXVIII,* abstract 2434. [9] Kiefer W.S. and Swafford, L.C. (2006) *J. Struct. Geo., 28,* 2144-2155.

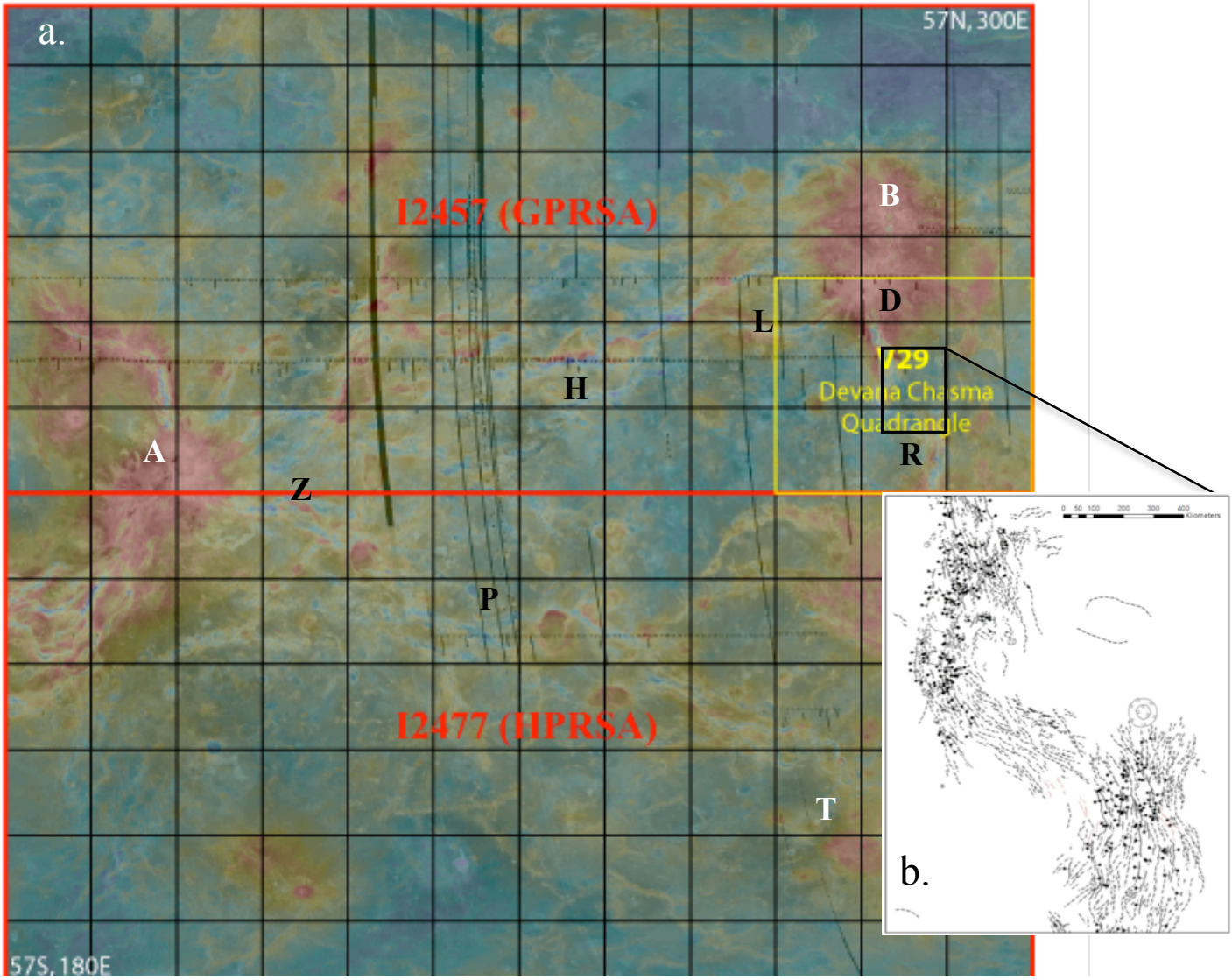

Figure 1a. The Beta Atla Themis province (apices identified by white letters) is a region of anomalously high volcanic, tectonic, and relatively youthful activity (major chasmata identified by black letters). Figure 1b. Devana/Rona Chasmata rift offset.

Terra Sirenum Region: Providing a Window into pre-Tharsis and Tharsis Phases of Mars Crustal Evolution

Robert. C. Anderson[a], James M. Dohm[b], S. Robbins[c], B. Hynek[c], [a]Jet Propulsion Laboratory, California Institute of Technology, Pasadena, CA 91109, [b]University of Arizona (jmd@hwr.arizona.edu), Department of Hydrology and Water Resources, Tucson, Arizona, USA, [c]Laboratory for Atmospheric and Space Physics, University of Colorado, Boulder, Colorado USA, **robert.c.anderson@jpl.nasa.gov.**

Introduction: Structural mapping is vital to unraveling the geologic histories at local to global scales on Earth as well as Mars. For the equatorial region of Mars, the formation of the Tharsis rise dominated the geologic and tectonic histories. A key region to assess this major part of the geologic history of Mars is Terra Sirenum region. As such, we are constructing a geologic map of the region at 1:5,000,000-scale in both digital and print formats that will detail, in particular, the stratigraphic and crosscutting relations among rock materials and tectonic structures.

The Terra Sirenum region, which is located to the southwest of Tharsis, records not only the early development of the Tharsis magmatic complex [1-3], but just as importantly, contains some of the oldest stratigraphic units found in the western hemisphere region of Mars. Detailed examination of the structures and units within this region provides an excellent window into identifying the tectonic processes that resulted from the formation of Tharsis, but also structures that influenced the geologic evolution of the ancient (pre-Tharsis) phase of the evolution of Mars. Here, we present recent results from our mapping effort detailing the geologic history of this region.

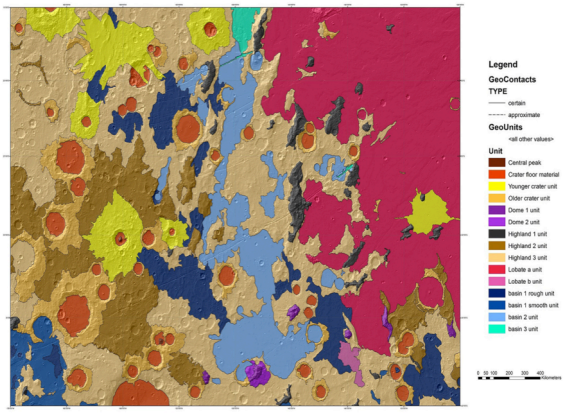

Fig. 1 Stratigraphic map of the Terra Sirenum region of Mars.

Overview of Pre-Tharsis Terrains: Pre-Tharsis tectonism identified in this region is expressed by 1) stratigraphic units displaying magnetic signatures, 2) a set of largely north-trending prominent complex faults (defined as macrostructures [4] due to their enormous geometric proportions including lengths reaching thousands of kilometers), and 3) numerous structurally-controlled basins (widths vary from kilometers to hundreds of kilometers) displaying water enrichment in the substrate reminiscent in many respects to the Basin and Range topography, found in the southwest United States. Some of the marcostructures might be related to the incipent development of Tharsis.

Tharsis-Influenced Terrains: Following the early dynamic ancient pre-Tharsis stage of Mars evolution, the growth of Tharsis intermingled with the pre-existing structures. Some of the structures attributed to the formation of Tharsis in this region include reactivation of ancient basement structures and the formation of the South Tharsis Ridge Belt, additional basin formation, the formation of large faults systems (e.g., Sirenum Fossae), and dike emplacement centered about Tharsis [2-5]. There is strong evidence suggesting interplay between the macrostructures, the water-enriched structurally controlled basins, and the Tharsis-centered faults and dikes. Examples of this interplay include Mangala Valles that sources from a Tharsis-centered fault in one of the north-trending basins and collapse structures along some of the Tharsis-centered faults, some of which display fluvial activity.

Impact Crater Perspective: Crater statistics have been recently completed for our stratigraphic map of the Terra Sirenum region (**Fig. 2 – Table 1**) using a new global impact crater database [6-7]. In addition, all impact craters with diameters ≥ 3 km were manually examined to identify only those superposed on the most recent resurfaced terrains: those impact craters that display pristine rims and ejecta blankets, and well-defined bowl-shaped basins with little to no infill that have no visible evidence of volcanic, fluvial, and tectonic resurfacing. The superposed impact craters were additionally verified through ConTeXt camera images where there was coverage [8]. The impact crater retention ages are shown in Table 1 partly based on the modeling schemes of [9] and [10].

The following is observed through Table 1 in conjunction with the geologic mapping: (1) ancient cratered highlands basements including

macrostructures are Early Noachian-Middle Noachian; (2) basin formation was established by the Middle Noachian with possible subsequent growth; (3) lavas on the western flank of Tharsis were emplaced during the Late Noachian to Late Hesperian (Stages 2-4, see [1-3]) and even as late as Middle Amazonian based on the superposed crater counts; (4) Late Noachian-Early Amazonian resurfacing of cratered highlands material, tectonic structures, and basins based on the superposed crater counts, correlative with the significant stages of Tharsis development (Stages 1-4), and (5) the source region of Mangala Valles has no superposed impact craters, which indicates Amzonian resurfacing.

SUMMARY. Ancient terrains, that record a dynamic phase in the evolution of Mars, merits further investigation. For example, what are the primary rocks that compose the ancient terrains and what caused the Basin and Range-like topography? Such a region could help us address whether Mars records and ancient phase of plate tectonism, perhaps very different then that of the Earth.

REFERENCES. [1] Dohm, J.M., et al., 2001. J. Geophys. Res. 106, 32 943-32 958. [2] Anderson, R.C., et al., 2001. J. Geophys. Res. 106, 20,563-20,585. [3] Dohm, J.M., et al., 2007. In Superplumes: beyond plate tectonics. D.A Yuen, S. Maruyama, S-I Karato, and B.F. Windley (eds.). Springer, London, 523-537. [4] Dohm, J.M.et al. (2002) Lunar Planet. Sci. XXXIII, 1639 (abstract). [5] Scott, D.H., and Tanaka, K.L. (1986) USGS Misc. Inv. Ser. Map I-1802-A (1:15,000,000), [6] Robbins, S.J., 2011. Ph.D. Thesis, CU, Boulder. Robbins, S., and Hynek, B., [7] Robbins, S.J.; and Hynek, B.M., 2011. Submitted to JGR-Planets. doi: 10.1029/2011JE003966. [8] Malin, M.C., et al., 2007. J. Geophys. Res. 112, doi: 10.1029/2006JE002808. [9] Hartmann, W.K., 2005. Icarus 174, 294-320. [10] Neukum, G., et al., 2001. In Chronology and Evolution of Mars (R. Kallenbach, J. Geiss, and W. K. Hartmann, eds.), Kluwer Academic Publishers, 55-8.

Table 1. Cumalative crater densities and unit ages of geologic units in the Terra Sirenum region.

Name	Area (km^2)	Type	*N*(3)*	*N*(5)*	*N*(16)*	*N*(3) Age	*N*(5) Age	*N*(16) Age	Epoch
Basin 1 Rough Unit	257,751	T, N	632±50	407±40	144±24	3.82±0.01	3.87±0.02	3.92±0.03	MN-LN
		T, H				3.66±0.01	3.76±0.01	3.93±0.02	MN-EH
		S, N	302±34	132±23	8±5	3.68±0.02	3.66±0.04	2.12±1.3	EH-EA
		S, H				3.45±0.04	3.47±0.05	2.21±1.0	MN-LN
Basin 1 Smooth Unit	69,673	T, N	459±81	287±64	100±38	3.77±0.03	3.80±0.04	3.92±0.06	MN-LH
		T, H				3.59±0.04	3.67±0.04	3.94±0.04	EH-LH
		S, N	244±59	129±43	29±21	3.64±0.06	3.64±0.08	3.50±1.0	LH
		S, H				3.34±0.15	3.43±0.14	3.46±0.60	MN-LN
Basin 2 Unit	310,578	T, N	557±42	345±33	171±23	3.80±0.01	3.84±0.02	3.94±0.02	MN-EH
		T, H				3.64±0.01	3.72±0.01	3.95±0.02	EH-LH
		S, N	229±27	93±17	19±8	3.63±0.03	3.58±0.05	3.55±0.16	LH-EA
		S, H				3.31±0.07	3.28±0.14	3.58±0.09	LH-EA
Basin 3 Unit	19,908	T, N	402±142	251±112	100±71	3.74±0.07	3.79±0.08	3.87±0.16	MN-LN
		T, H				3.56±0.08	3.66±0.08	3.88±0.10	MN-LH
		S, N							Not Superposed
		S, H							Not Superposed
Highland 1 Unit	81,363	T, N	762±97	504±79	86±33	3.85±0.02	3.91±0.02	3.77±0.07	MN-LN
		T, H				3.71±0.02	3.80±0.02	3.76±0.05	LN
		S, N	209±51	135±41		3.62±0.06	3.67±0.07		EH
		S, H				3.27±0.20	3.50±0.09		LH
Highland 2 Unit	365,221	T, N	849±48	553±39	197±23	3.87±0.01	3.92±0.01	3.97±0.02	EN-MN
		T, H				3.72±0.01	3.81±0.01	3.97±0.01	EN-LN
		S, N	367±32	156±21	19±7	3.72±0.02	3.70±0.03	3.48±0.21	LN-LH
		S, H				3.52±0.02	3.54±0.03	3.50±0.12	LH
Highland 3 Unit	1,197,850	T, N	852±27	585±22	171±12	3.87±0.01	3.93±0.01	3.95±0.01	EN-MN
		T, H				3.72±0.00	3.82±0.00	3.96±0.01	EN-LN
		S, N	276±15	143±11	18±4	3.66±0.01	3.68±0.02	3.48±0.10	LN-LH
		S, H				3.40±0.02	3.51±0.02	3.51±0.06	LH
Lobate A Unit	922,775	T, N	200±15	118±11	59±8	3.58±0.02	3.64±0.02	3.77±0.03	LN-LH
		T, H				3.11±0.09	3.43±0.03	3.78±0.02	LN-LH
		S, N	52±8	16±4	3±2	1.99±0.29	1.27±0.33	1.03±0.60	MA
		S, H				0.87±0.10	0.65±0.13	1.12±0.48	MA
Lobate B Unit	12,084	T, N		497±203	248±143		3.95±0.06	3.98±0.11	Basement not flow
		T, H					3.87±0.05	3.99±0.07	Basement not flow
		S, N							Not Superposed
		S, H							Not Superposed
Older Cratered Unit	305,477	T, N	593±44	344±34	72±15	3.81±0.01	3.84±0.02	3.81±0.04	MN-LN
		T, H				3.66±0.01	3.73±0.01	3.82±0.03	MN-EH
		S, N	249±29	121±20	13±7	3.65±0.03	3.64±0.04	3.42±0.62	EH-LH
		S, H				3.38±0.05	3.44±0.06	3.46±0.24	LH
Younger Cratered Unit	272,632	T, N	873±57	381±37	114±20	3.87±0.01	3.86±0.02	3.87±0.03	MN
		T, H				3.73±0.01	3.74±0.01	3.88±0.02	MNMN-LN-LN
		S, N	293±33	139±23	18±8	3.68±0.02	3.68±0.03	3.48±0.35	EH-LH
		S, H				3.45±0.04	3.51±0.04	3.50±0.16	LH

*Crater density is per 10^6 km^2

GEOLOGIC MAPPING OF THE LUNAR SOUTH POLE QUADRANGLE (LQ-30). S.C. Mest[1,2], D.C. Berman[1], N.E. Petro[2], and R. A. Yingst[1], [1]Planetary Science Institute, 1700 E. Ft. Lowell, Suite 106, Tucson, AZ 85719-2395 (mest@psi.edu); [2]Planetary Geodynamics Laboratory, Code 698, NASA GSFC, Greenbelt, MD 20771.

Introduction: We are using recent image, spectral and topographic data to map the geology of the lunar South Pole quadrangle (LQ-30) at 1:2.5M scale [1-7]. The overall objective of this research is to constrain the geologic evolution of LQ-30 (60°-90°S, 0°-±180°) with specific emphasis on evaluation of a) the regional effects of impact basin formation, and b) the spatial distribution of ejecta, in particular resulting from formation of the South Pole-Aitken (SPA) basin and other large basins. Key scientific objectives include: 1) Determining the geologic history of LQ-30 and examining the spatial and temporal variability of geologic processes within the map area. 2) Evaluating the distribution of volcanic materials within the map area. And 3) constraining the distribution of impact-generated materials, and determining the timing and effects of major basin-forming impacts on crustal structure and stratigraphy in the map area.

Methodology: This project utilizes ArcGIS (v. 10.1) to compile image, topographic and spectral datasets to produce a geologic map of LQ-30. The study uses the Lunar Reconnaissance Orbiter (LRO) Wide Angle Camera (WAC) mosaic (~100 m/pixel) as its primary base to characterize geologic units from surface textures and albedo, identify contacts and structures, and map impact craters (D>1 km). Additional datasets are being used to complement the base and include mosaics (Lunar Orbiter, Clementine UVVIS and NIR), images (LROC, Clementine UVVIS and HIRES, and Lunar Orbiter), Clementine color ratio data, Moon Mineralogy Mapper (M3) multispectral data, and LOLA topography.

Regional Geology: LQ-30 exhibits ~16 km of relief. The near side consists predominantly of cratered highlands, is more heavily cratered and displays higher elevations than the far side. This difference is due to the overwhelming presence of SPA, which encompasses nearly all of the far side map area.

SPA is the largest (D=2600 km, ~18 km deep) and oldest (pre-Nectarian) impact basin identified on the Moon [8-10]. Models suggest that SPA formed by an oblique impact that excavated material from the upper crust [11,12] to the lower crust or upper mantle [13,14]. Galileo and Clementine multispectral data show enrichment in mafic materials [15-19] and LP-GRS data show enhancements in both Fe and Th [20-23] within the basin relative to the surrounding highlands. The materials exposed within SPA, such as in central peaks or in crater walls, could be used to estimate the composition of the lower crust/upper mantle.

Mapping Results: LQ-30 hosts all or part of 46 impact features greater than 100 km in diameter that would have significantly affected the structure of the crust and redistributed large amounts of material across the surface [7]. Impact craters display morphologies ranging from simple to complex [7-9,24] and most contain floor deposits distinct from surrounding materials. Most of these deposits likely consist of impact melt; however, some deposits, especially on the floors of the larger craters and basins (e.g., Antoniadi), exhibit low albedo and smooth surfaces and may contain mare. Higher albedo deposits tend to contain a higher density of superposed impact craters.

Antoniadi Crater. Antoniadi crater (D=150 km; 69.5°S, 172°W) is unique for several reasons. First, Antoniadi is the only lunar crater that contains both a peak ring and a central peak, placing it morphologically between impact craters and multi-ring basins [8,9]. Second, it contains the lowest elevations on the Moon (-8.5 km), which may provide access to lower crustal/upper mantle materials via its central peak and peak ring. Its floor deposits consist of dark smooth material near the center of the crater, and brighter more rugged material between the peak ring and crater wall [7,25]. Recent mapping shows that the dark material embays the rugged material, as well as the peak ring and central peak. The rugged material likely includes impact melt. Superposition relationships indicate the dark material was emplaced after the rugged material and may consist of mare [7].

Crater size-frequency distributions for small craters (D<10 km) superposed on Antoniadi's ejecta blanket suggest an Upper Imbrian age, whereas craters greater than 10 km in diameter suggest a Lower Imbrian/Nectarian age [7,25]. It is important to note that Antoniadi's ejecta blanket also contains a significant number of secondary craters that are likely included in the counts and will affect age determination.

Schrödinger Basin. Schrödinger basin (76º S, 134º E) is one of the least modified lunar impact basins of its size, is believed to be Imbrian in age [6-8,26], and is likely one of the last major basin-forming impact events on the Moon, slightly older than the Orientale impact, which emplaced secondary craters on Schrödinger's floor [26]. The basin exhibits an outer ring (D=312 km) that defines its rim and an inner peak ring (D=160 km) represented by a discontinuous ring of mountains. LOLA topography shows the basin is ~8 km deep with elevations of ~2.5 km (max) along the western rim and -5.5 km (min) on the floor [6,7].

Arcuate to linear fractures are prominent on the basin floor and occur concentric and radial to the basin rim. Most fractures bisect plains-forming units, but some bisect the peak ring. These features are a few kilometers wide, and tens to a few hundred kilometers long and appear similar to other floor-fractured craters on the Moon and Mars [27].

Mapping has identified nine distinct units in the Schrödinger Assemblage organized into three groups - Basin Materials, the Plains Formation, and the Volcanic Formation [6,7].

Basin Materials: The oldest materials exposed in Schrödinger are *Schrödinger peak ring material* and *Schrödinger basin rim material* [6,7]. The peak ring material forms an incomplete ring of mountains around the center of Schrödinger. The basin rim material forms the topographic rim crest and interior wall of Schrödinger. These materials are interpreted to consist of pre-Schrödinger crustal materials uplifted following the impact event [6,7,12,28].

Plains Formation: The floor of Schrödinger is covered with plains-forming materials that display a variety of surface textures and albedos. *Schrödinger rugged plains material* is the oldest plains material on the basin floor. Most exposures are found outside of the peak ring and form heavily cratered and knobby plateaus and massifs of moderately high albedo [6]. *Schrödinger hummocky plains material* occupies much of the floor along the northern and western walls within Schrödinger, and in the south where the peak ring is the most discontinuous. Hummocky plains display moderately cratered, low albedo surfaces with gently rolling topography [6]. The rugged and hummocky plains materials are interpreted to consist of impact melt [6,7].

Schrödinger smooth plains material, found just inside the peak ring, embays the rugged plains, peak ring and basin wall materials. The smooth plains display moderate to high albedo and contain few craters [6]. *Schrödinger mottled plains material*, found primarily in the center of Schrödinger, displays a smooth surface that is lower in albedo and less cratered than the smooth plains. The smooth plains and mottled plains materials are interpreted to be volcanic (mare) in nature, possibly erupted via floor fractures [6,7].

Schrödinger knobby plains material forms two high-albedo deposits along the southern basin wall. These deposits exhibit lobate edges, and clusters of rounded and elongated knobs. Knobby plains material is interpreted to be (a) impact ejecta, (b) basin wall materials emplaced by landslides, and/or (c) more rugged exposures of the rugged plains [6,7].

Volcanic Formation: Volcanic materials are concentrated inside Schrödinger's peak ring. *Schrödinger dark plains material* displays a smooth, featureless, low albedo surface. Clementine UVVIS color ratio data show these deposits are more mafic relative to other Schrödinger plains [6]. Within one exposure, a long (10s of kilometers) sinuous rille emerges from the mottled plains and terminates within the dark plains. Dark plains material is interpreted to be composed of fluid basaltic lavas [5-7].

A small (D=5 km) well-preserved ovoidal cone is found in the eastern part of Schrödinger, just inside the peak ring. The cone displays ~500 m of relief above the surrounding plains and is ~400 m deep from its floor to its rim [6]. The cone has been characterized as a "maar" crater [26] and a "dark-halo crater" (DHC) [29], and has been identified as the source of pyroclastic eruptions [26,29]. *Schrödinger dark material* forms a small deposit that surrounds and forms the flank of the DHC. This deposit exhibits a relatively smooth, lightly cratered surface with lower albedo than the surrounding plains [6]. Schrödinger dark material displays an unusually strong mafic band (950/750 nm versus 750 nm) in Clementine UVVIS data, but also displays similarities to lunar highland soils [29]. Based on the unit's relationship with the DHC and its spectral signature, Schrödinger dark material is interpreted to consist partly of mafic materials emplaced via pyroclastic eruptions originating from the DHC [6,7]. The deposit's spectral signature suggests contamination by feldspathic highland-type materials either by superposed crater materials and/or vertical mixing [29].

Mare Deposits. Mare deposits are found on the floors of some impact craters, but are also found on the floor of Australe basin along the eastern limb near the northern edge of the map area (~62°S, 90°E). These deposits are dark and smooth in appearance, but some are brighter and more rugged suggesting they are older and have been modified since their emplacement by (1) mantling by ejecta, (2) mixing by subsequent impacts, and/or (3) gardening and regolith development [7,8].

References: [1] Mest, S.C. (2007) LPSC XXXVIII, **#1842**. [2] Van Arsdall, L.E. and S.C. Mest (2008) LPSC XXXIX, **#1706**. [3] Mest, S.C. and L.E. Van Arsdall (2008) NLSI LSC, NASA ARC, **#2089**. [4] Mest, S.C. (2008) GSA Joint Annual Mtg., **#324-3**. [5] Mest, S.C. (2009) Ann. Mtg. of Planet. Geol. Mappers, San Antonio, TX. [6] Mest, S.C. (2010) GSA Sp. Paper 447, SPE477-04. [7] Mest, S.C. et al. (2010) LPSC XLI, #**2363**. [8] Wilhelms, D.E. et al. (1979) USGS MISM I-1162, 1:5M scale. [9] Wilhems, D.E (1987) *USGS Prof. Pap*. **1348**. [10] Spudis, P.D. et al. (1994) *Science*, **266**, 1848-1851. [11] Schultz, P.H. (1997) LPSC, XXVII, **#1259**. [12] Schultz, P.H. (2007) LPSC, XXXVIII, **#1839**. [13] Melosh, H.J. (1989) Impact Cratering, 245 pp. [14] Cintala, M.J. and R.A.F. Grieve (1998) Met. and Planet. Sci., **33**, 889-912. [15] Belton, M.J.S. et al. (1992) *Science*, **255**, 570-576. [16] Head, J.W. et al. (1993) *JGR*, **98**, 17,149-17,182. [17] Lucey, P.G. et al. (1998) *JGR*, **103**, 3701-3708. [18] Pieters, C.M. et al. (1997) *GRL,* **24**, 1903-1906. [19] Pieters, C.M. et al. (2001) *JGR*, **106**, 28,001-28,022. [20] Lawrence, D.J. et al. (1998) *Science*, **281**, 1484-1489. [21] Lawrence, D.J. et al. (2002) New Views of the Moon, Europe, 12-14. [22] Lawrence, D.J. et al. (2002) *JGR*, **107**, doi:10.1029/200lJE001530. [23] Jolliff, B.L. et al. (2000) *JGR*, **105**, 4197-4216. [24] Wood, C.A. and L. Andersson (1978) Proc. Lunar Planet. Sci. Conf., 9th, 3669-3689. [25] Dominov, E. and S.C. Mest (2009) LPSC, XL, **#1460**. [26] Shoemaker, E.M. et al. (1994) *Science*, **266**, 1851-1854. [27] Schultz, P.H. (1976) *The Moon*, **15**, 241-273. [28] Spudis, P.D. (1993) The Geology of Multi-ring Impact Basins: The Moon and Other Planets. [29] Gaddis, L.R et al. (2003) *Icarus*, **161**, 262-280.

A REASSESSMENT OF THE VOLCANIC HISTORY OF WESTERN SOUTH POLE-AITKEN BASIN BASED ON GEOLOGIC MAPPING. R. A. Yingst[1], F. C. Chuang[1], D. C. Berman[1], and S. C. Mest[1], [1]Planetary Science Institute (1700 E. Fort Lowell, Suite 106, Tucson, AZ 85719; yingst@psi.edu).

Introduction: Constraining physical and mechanical models of lunar volcanic processes requires a full inventory, characterization and stratigraphic analysis of volcanically-produced surface materials. To this end, we are constructing a 1:2,500,000-scale map of Planck Quadrangle or Lunar Quadrangle 29 (Figure 1), which includes west SPA. Previous maps of the region [1, 2] were based on Lunar Orbiter images, which in most cases were oblique, low-resolution images and in every case did not contain mineralogical or elemental information. In this investigation, we document the stratigraphy, extent and characteristics of west SPA by incorporating regional morphology, composition, topography, elevation and elemental abundance data.

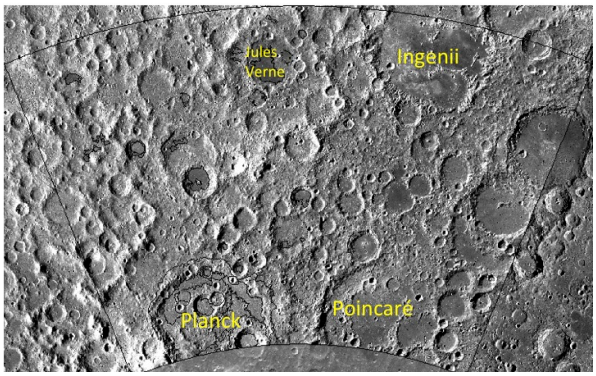

Figure 1. Planck Quadrangle (outlined in black) with large impact structures noted.

Geologic Setting: The quadrangle is dominated by the western portion of the pre-Nectarian South Pole-Aitken Basin. This basin is the oldest and deepest in the Solar System [e.g., 3-5]. The basin floor is dominated by multiple, overlapping impact structures from sizes below resolution to over 600 km across.

Previous work [1, 2] identified mare deposits as the primary volcanic product in the region. These deposits were dated as Imbrian-aged and mapped as discrete, non-contiguous deposits [6] occurring exclusively within or breaching the rims of craters or basins (areas of low crustal thickness [5]). Based upon assessment of the morphology [7] and subsequent compositional analysis [8, 9], the composition of these ponds was interpreted as basaltic, similar to the nearside maria, but low in mafic material such as Fe and Ti (possibly due to vertical or lateral mixing of non-mare soils beneath these thin, areally small deposits [10]). Potential pyroclastic deposits were mapped only in basins such as Poincaré. Cryptomare material (patches of basaltic material buried or mixed into the regolith as a result of impact activity [e.g., 11]) does not appear in previously-published geologic maps of the region [1, 2].

Data Sets and Collection: Morphology was determined using ~100 m/pixel Lunar Reconnaissance Orbiter Camera (LROC) images as the basemap (Figure 1). Clementine multispectral data was utilized to extract compositional information. Coverage includes ultraviolet/visible (5 bands between 415 and 1000 nm) and near-infrared (6 bands between 1100 and 2780 nm) data. We examined the 750/950 nm, 750/415 nm, and 415/750 nm band ratios. The 750/950 nm ratio (green channel) indicates FeO content; the deeper the absorption feature, the greater the FeO content. The other band ratios measure the red-to-blue "continuum slope;" the younger the soil, the flatter the slope. Data acquired by the Lunar Orbiter Laser Altimeter (LOLA) yields topographic data at 100 m/pixel.

Volcanic deposits were identified based on albedo, texture, morphology and spectral signature. Smooth, low-albedo surface materials with relatively sharp boundaries and elevated mafic content were mapped as mare deposits. Rougher surface deposits with very low albedo, diffuse or irregular boundaries, and elevated mafic content were mapped as pyroclastic deposits. Areas of heightened mafic content that otherwise showed little or no morphologic indication of volcanic origin were considered potential candidates for cryptomare materials and were tagged for further study.

Observations and Interpretations: Using these data sets, we identified ~40 potential volcanically-emplaced surface deposits. This total includes 22 smooth, low-albedo, higher-Fe deposits we interpret to be mare deposits or ponds, and ~18 rougher, very low-albedo, higher-Fe materials with irregular, diffuse boundaries we interpret to be pyroclastic materials. The uncertainty in the number of pyroclastic materials stems from the diffuseness of most boundaries; it is not always clear whether a deposit should be divided into multiple discrete deposits. Several candidate areas for the presence of cryptomare materials were also identified, including small patches in Planck.

We confirm the previous identification of most mare units based on morphologic characteristics, though we refined the boundaries of some of these deposits using higher resolution morphologic data, Clementine compositional data, and LOLA-derived topographic data.

However, in the work presented here we have identified additional mare materials, as well as several pre-

viously unmapped pyroclastic deposits. For traditional mare materials, our mapping indicates that 5% should be added to the previous areal total, due to the refining of boundaries and redefining of 1-2 smooth plains deposits as mare deposits. Additionally, we preliminarily add 3,000-5,000 km^2 of areal coverage to the volcanic inventory in the form of pyroclastic deposits. A greater surface area of west SPA is thus covered with volcanics than previously mapped. This increased area implies a higher volcanic flux. Higher resolution also reveals finer features than were previously identifiable, that may inform volcanic history. These include potential individual flows, wrinkle ridges, and fractures associated with pyroclastic deposits.

Discussion: Geologic mapping of west South Pole-Aitken (SPA) indicates that a larger area than previously indicated is covered by volcanic deposits; this would potentially place new constraints on our understanding of the global lunar thermal budget. We are refining crater frequency-derived ages to determine whether the period of volcanic activity in this area may be extended in time as well as space.

We infer from the broader morphologic range of identified and mapped volcanic products that mode of emplacement of volcanic deposits (an indication of conditions at depth) was more diverse in west SPA than previously assumed. Association of fractures with low-albedo deposits interpreted to be pyroclastic deposits might indicate a tectonic mechanism for emplacement, such as near-surface dike emplacement. Understanding the nature and stratigraphy of lunar volcanic activity will ultimately provide constraints on models of lunar volcanic generation and evolution.

References: [1] Stuart-Alexander, D. (1978) U.S. Geol. Surv. Map, I-1047. [2] Wilhelms, D. et al. (1979) U.S. Geol. Surv. Map, I-1162. [3] Wilhelms, D. (1987) The Geological History of the Moon, U.S. Geol. Surv. Prof. Pap., 1348, 302 pp. [4] Spudis, P., et al. (1994) Science, 266, 1848-1851. [5] Wieczorek, M.A. and Phillips, R.J. (1999) Icarus, 139, 246-259, 10.1006/icar.1999.6102. [6] Yingst, R.A. and Head, J.W. (1997) J. Geophys.Res., 102, 10,909-10,931. [7] Zuber, M., et al. (1994) Science, 266, 1839-1843. [8] Yingst, R.A. and Head, J.W. (1999) J. Geophys. Res., 104, 18,957-18,979. [9] Lucey, P.G. et al. (2005) Lunar Planet. Sci. Conf., 36th, Abs. #1520. [10] Li, L. and Mustard, J.F. (2005) J. Geophys. Res., 110, doi:10.1029/2004JE002295. [11] Hawke, B.R. et al. (1990) LPI-LAPST Wksp on Mare Volcanism and Basalt Petrogenesis, p. 5-6.

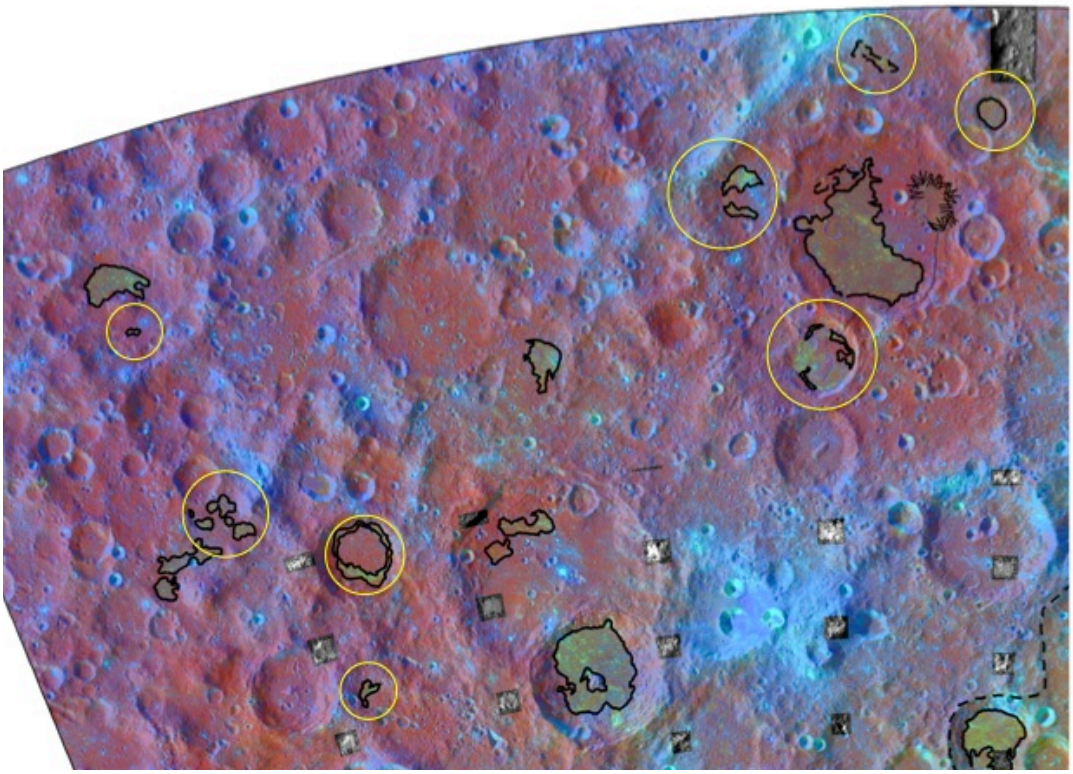

Figure 2. Volcanic surface deposits in western Planck Quadrangle. Yellow circles indicate deposits newly-identified or newly-classified. LROC Wide Angle Camera image mosaic constitutes the basemap; the Clementine color ratio mosaic (shown at 60% transparency) is superposed on the basemap.

MINERALOGIC MAPPING OF HUYGENS CRATER, MARS. S. E. Ackiss, K. D. Seelos, and D. L. Buczkowski, Johns Hopkins University Applied Physics Laboratory, Laurel, MD 20723 (Sheridan.Ackiss@jhuapl.edu).

Introduction: Huygens crater is a well preserved peak ring structure on Mars centered at 13.5°S, 55.5°E in the Noachian highlands between Terras Tyrrhena and Sabaea (Figure 1). With a diameter of ~450 km, it uplifted and exhumed Noachian crustal materials from depths greater than 30 km, likely including Hellas rim material (Figure 2).

In neighboring terrains, numerous small outcrops of aqueously altered minerals, such as phyllosilicates, have been identified [1-2] as well as frequent expanses of mafic-bearing plains [3-6]. By mapping the distribution of these different mineral types in and around Huygens, we hope to offer unique insight into emplacement and alteration history of the highlands crust.

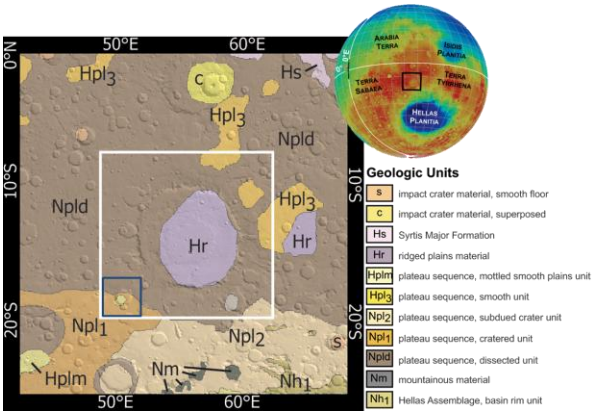

Fig. 1. Regional geologic units [7] surrounding Huygens crater; the study region (white box) spans approximately 7.5-20°S and 49-62°E. The global view is shown in the upper right corner. Blue box shows regional context for Figure 3.

Data sets and Methods: We utilize data from the Compact Reconnaissaince Imaging Spectrometer for Mars (CRISM) as well as multiple other global data sets. Basemap data include Thermal Emission Imaging System (THEMIS) daytime IR (100 meters/pixel) and nighttime IR (265 pixel/degree or ~230 meters/pixel), as well as Mars Orbiter Laser Altimeter (MOLA) topographic data (128 pixel/degree or ~460 meters/pixel) and MOLA shaded relief (128 pixel/degree). Each basemap was imported into ArcMap 10.1 where the geodatabase and mapping contacts were developed and stored.

The CRISM instrument [8] acquires visible and near infrared (0.36-3.9 μm) data that record information about primary mafic mineraology, ferric-bearing minerals, and hydrated minerals like sulfates and phyllosilicates. Twelve CRISM multispectral map-tiles (mosaicked at ~230 meters/pixel and corrected to Lambert Albedo) were used to understand regional mineralogic trends and define unit contacts. Summary parameters [9] showing spectral absorptions associated with the mafic minerals olivine (OLINDEX), low-calcium pyroxene (LCP, LCPINDEX), and high-calcium pyroxene (HCP, HCPINDEX) were examined. Figure 3A shows an RGB composite of these three parameters, respectively, for a subset of the map. Summary parameters that highlight the presence of hydrated minerals were also utilized. Specifically, the D2300 parameter aided in the identification of Fe/Mg phyllosilicate-bearing materials (Figure 3B) while the BD1900 parameter showed the presence of other hydrated minerals. Contacts were drawn where data is present and believable (spatially coherent, or inconsistent with noise) at 1:250K scale and in some cases inferred by morphology due to the lack of CRISM coverage. For reference, boundaries of large morphologic provinces, like Huygens rim and peak ring, were also outlined.

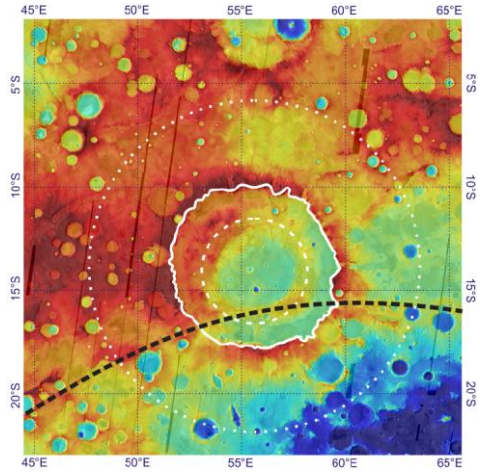

Fig. 2. Topography of the study region from MOLA. White lines indicate the locations of the crater rim (solid), peak ring (dashed), and one crater radius as the expected extent of the continuous ejecta (dotted). The black dashed line shows the rim of the Hellas basin [10].

Preliminary Mapping Results:

Units and Distribution: Four mineralogy-based units have been defined for the Huygens study region so far: olivine-, HCP-, LCP-, and Fe/Mg phyllosilicate-bearing material.

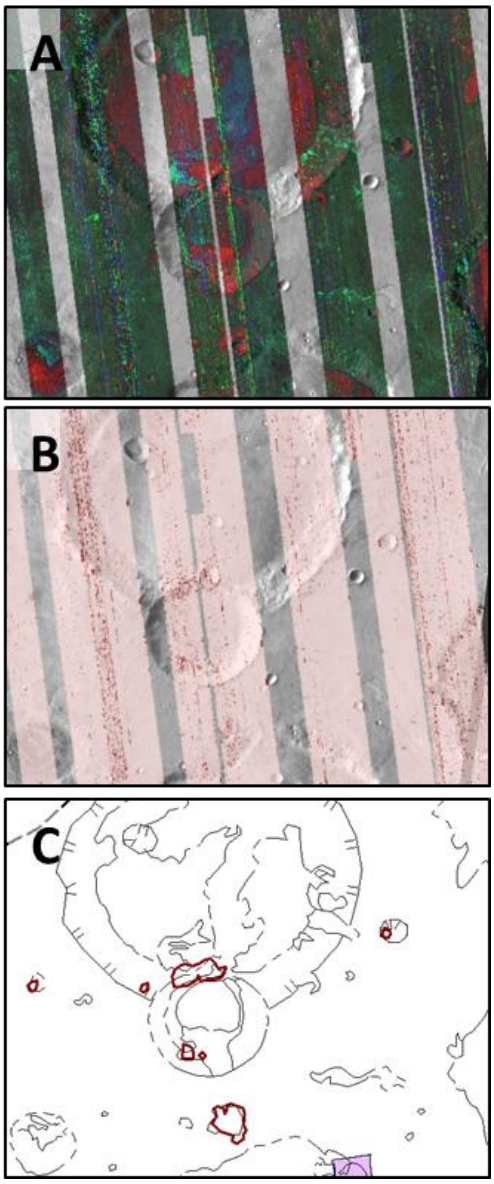

Fig. 3. Southwest corner of Huygens study region showing CRISM multispectral maps and contacts thus far. (A) Browse products composed of R = olivine, G = LCP, B = HCP over THEMIS daytime IR. (B) D2300 parameter stretched from 0.005 (pink) to 0.03 (red) over THEMIS daytime IR. (C) Black contacts show units within the mafics browse product with morphology outlines and red contacts show the D2300 map.

The olivine-bearing unit is associated with topographically lower, generally flat-lying plains, including the floor of Huygens and the infilled floors of smaller surrounding craters. It is also observed on intercrater plains consistent with high thermal interia, olivine-bearing "bedrock" units described by Rogers et al. [5]. Mapped occurrances of HCP-bearing material appear associated with similar plains morphology, also occurring in areas on the floor of Huygens as well as gradational with olivine-bearing plains within smaller, unnamed craters in the southwest part of the study region.

Exposures of LCP occur in distinct outcrops concentrated in the southern portion of the map area, interior to the Hellas rim boundary (Figure 3A). LCP is associated with a more erosionally-resistant material, usually forming knobs.

Fe/Mg phyllosilicate-bearing materials are localized and have been exposed by impact cratering, with signatures observed on crater rims, walls, and in ejecta blankets. Phyllosilicates are identified both inside (on the floor of) and outside Huygens.

Comparison to Existing Geologic Map: Olivine- and HCP-bearing units roughly correspond to two units of the Greeley and Guest [7] geologic map: superposed impact crater material (c) and Hesperian plains units (Hr and Hpl3; Figure 1). The olivine-bearing unit corrspondes to geologic unit c in the three larger craters in south. All of the other mineralogic units fall within areas mapped as Npld (Noachain dissected terrain).

Future Work: Unit contacts continue to be refined, especially in the north and west part of the map area where increased surface dust complicates the spectral signature. We are working to verify mineralogy inferred from the summary parameter maps using both CRISM multispectral mapping data and targeted hyperspectral data. The latter will allow determination of specific phyllosilicate mineralogy, for example. We are also characterizing the morphology of these units and combining this information with the mineralogy to develop an overall picture of geologic history of this region.

Acknowledgements: This work was supported by the NASA Mars Data Analysis Program (grant number NNX10AO25G) and in part by an appointment to the Postgraduate Research Participation Program at the Johns Hopkins University Applied Physics Lab (APL) administered by the Oak Ridge Institute for Science and Education (ORISE) through an interagency agreement between the U.S. Department of Energy and APL.

References: [1] Bibring, J.-P., et al. (2005) Sci., 307, 1576-1581. [2] Loizeau, D., et al. (2012) Icarus, 219, 476-497 [3] Koeppen, W. C., et al. (2008) JGR, 113, E05001. [4] Mustard, J. F., et al. (2005) Sci., 307, 1594-1597. [5] Rogers, D., et al. (2011) JGR, 116, E08005. [6] Rogers, D. et al. (in press) JGR. [7] Greeley and Guest (1987), USGS Misc. Invest. Series, Map I-1802-B. [8] Murchie, S. L., et al. (2007) JGR, 112, E05S03. [9] Pelkey, S. M. et al. (2007) JGR, 112, E05S14. [10] Wichman and Schultz (1989) JGR, 94, 17333-17357.

GEOLOGIC MAP OF THE OLYMPUS MONS VOLCANO, MARS. J.E. Bleacher[1], D.A. Williams[2], P.J. Mouginis-Mark[3], D. Shean[4], R. Greeley[2*], [1]Planetary Geodynamics Laboratory, Code 698, NASA GSFC, Greenbelt, MD, 20771, Jacob.E.Bleacher@nasa.gov, [2]School of Earth & Space Exploration, Arizona State University, Tempe, AZ, 85282, [3]Hawaii Institute of Geophysics and Planetology, University of Hawaii. [4]Malin Polar Science Center, Applied Physics Lab, University of Washington, Seattle, WA, 98105 [*]Deceased.

Introduction/Background: We have completed a first draft of a Mars Data Analysis Program-funded project to map the morphology of the Olympus Mons (OM) volcano, Mars, using ArcGIS by ESRI. The final product of this project is to be a 1:1,000,000-scale geologic map. The scientific questions upon which this mapping project is based include understanding the volcanic development, including identification of volcanic unit source areas, and subsequent modification by structural, aeolian, and possibly glacial processes.

Methods: To address our science questions we conducted morphology mapping at ~ 1:300,000 scale using the Context Camera (CTX) and High Resolution Stereo Camera (HRSC) image mosaic as our base data. This scale enables a distinction between sinuous rilles and leveed channels, which is fundamental for interpreting abundances among, and changes between, tube- and channel-forming eruptions. We have combined our map with Mouginis-Mark's Planetary Geology & Geophysics-funded geologic map of the Olympus Mons Caldera that was produced at 1:200,000 scale and provides additional detail of the summit region.

Results: We identified 34 units that are divided among Flank Units, Scarp and Apron Units, Plains Units, and Crater Materials. The Flank Units include 13 units, plus 7 caldera units. The basic morphological difference across the flank involves mottled and channeled units. The channel unit is typified by sub-parallel linear flows with levee structures. The mottled unit is hilly at the horizontal scale of 10s to 100s of meters. We did not delineate units that display the same morphology but appear to be the result of a different eruptive phase unless a unique source is inferred. Because a motivating question involves the identification of flank unit sources we subdivided channels and mottled units according to their apparent origin. These include Fan-sourced, Ridge-sourced, and Flank units (which can be traced to the caldera or have a source that is unclear). Fans and ridges are up to 100 m in height. Fans are delta-shaped whereas ridges are elongate, generally radial to the caldera. We identify a fan's apex as a location point.

We differentiate three scarp and three apron units. Generally, our Ravine Scarp unit and Etched Scarp units are comparable to the Slope 1 and Slope 2 units of Basilevsky et al. [1]. The Ravine Scarp Unit is steep (30-35 degrees) and displays sharp ravine-like features whereas the Etched Scarp Unit is shallower (7-15 degrees) and displays a less sharp, etched morphology. We also delineate Stepped Scarp which forms a series of topographic, down-stepped benches. This unit often separates the other scarp units from the Main Flank Units. Our Apron units include Chaotic, Arcuate Ridged, and Muted and generally follow the characterizations of Milkovich et al. [2].

The Plains Units are subdivided into Aureole units (including blocky, ridged and smooth), low shields, fissures, channel networks, smooth/platy unit and a knobby unit. Crater Materials include an impact crater cavity unit (and raised rim) and the ejecta blanket unit where identified. We also identify structural features, including scarps, ridges, and faults. We delineate sinuous chains of depressions or rilles from the channel unit as a linear feature. These generally form a trough that does not display levees.

Geologic History, New Insights: The volcanic history in the map area involves Olympus main flank eruptions followed by eruptions from low shields and fissure vents in the plains surrounding OM. These flows appear to embay main flank channels and tabular flows at the distal margin of the volcano, beyond the scarp materials, to the North, East, and South. Werner [3] conducted crater counts of select regions of the main flank and suggested that the volcano was largely in place by 3.8 Ga, and Basilevsky et al. [4] conclude that plains volcanism to the SE was occurring at 25-40 Ma. The main flank is dominated by mottled and channeled units of varied origin. We observe a transition from mottled- to channel-dominated surfaces with

distance from the caldera. The mottled units are in some cases distributed randomly about the main flank, but tend to be located proximal to eruptions sites (fan apex, ridge crest, or the caldera), whereas channels are located distally from eruptions sites. We interpret the mottled units to represent near vent lava flows in which significant channels and tubes have not developed (e.g., near vent sheet flows [5]). The dominance of this unit at the summit matches favorably with the subdued Aos1 unit of Morris and Tanaka [6]. In some cases we see that the mottled terrain results from channels that are below the detection limit for our mapping. In addition, these features might also be covered by dust or ash. With respect to azimuth around the main flank we observe that fans and rilles are less common on the NE and SW flanks of the volcano.

In contrast to our preliminary mapping [7], we do not map lava tubes as a unique unit. We identified four morphologies that we think are indicative of the presence of lava tubes, including 1) raised ridges, 2) sinuous chains of rimless pits or rilles, 3) lava fans, and 4) raised rim depressions of non-impact origin [8]. The features cited here are typically seen in terrestrial shield volcano flow fields in relationship with tubes. In general, the identification of one of these features alone is not indicative of a lava tube, but if two or more are identified together (adjacent or superposed) we feel confident that they reveal the presence of a tube. Based on this inference and superposition relations between inferred tubes and channels, we no longer identify a consistent burial of tubes by channels. Instead, we recognize that the apparent burial of some tubes is the result of ridge-sourced channels, which are essentially a product of the same eruption.

McGovern and Morgan [9] note asymmetries between the NW and SE flanks. They observe that the NW flank has the longest distance between caldera and scarp, displays lower flank extensional faults, where as the SE flank is shorter (caldera to scarp) and displays upper compressional terraces (also seen by [10]) and lower upthrust blocks. Both of these portions of the flank display concave up surfaces whereas the NE and SW flanks display more uniform slopes. They suggest that Olympus Mons has experienced volcano-wide spreading to the NW and SE as a result of a weaker, pre-Tharsis substrate. Mapping shows that the NE and SW scarps are completely embayed by young lavas, whereas the SE and NW flanks display exposed scarp material.

If the conclusions of McGovern and Morgan [9] are correct and the volcano is spreading to the NW and SE, then subsequent intrusion of magma into the volcano would likely exploit those spreading centers along the NE and SW flanks to reach the surface, as is seen on the Hawaiian volcanoes where rift zones open roughly parallel to the coast as the volcanoes spread into the ocean. Although we see a paucity of fans and possible eruption sites along these sections of the volcano it is possible that we have simply identified the readily noticed features related to lava tube breakouts and misinterpreted effusive spreading centers. If spreading centers exist along these sections of the volcano then magma might have been more easily delivered to these sections of the volcano, possibly explaining why the scarps are heavily buried in these sectors.

Future Work: Our current efforts are focused on additional higher resolution mapping and data analysis related to the map product. These efforts include 1) the identification of lava tubes and their products on the flanks of OM, 2) the interactions between volcanic rocks and frozen volatiles on OM, and 3) the volcanic-tectonic development and constraints of the eruptive frequency of the volcano.

References: [1] Basilevsky et al., (2005), Solar System Research, 39, 2, 85-101. [2] Milkovitch et al., (2006), Icarus, 181, 388-407. [3] Werner, S. (2009) Icarus, 201, 44-68. [4] Basilevsky et al. (2006) Geophys. Res. Lett., 33, L13201, doi:10.1029/2006GL026396. [5] Swanson, D. (1973) Geol. Soc. Am. Bull., 84, 615-626. [6] Morris and Tanaka (1994) USGS Misc. Inv. Series Map I-2327, Scale 1:2M and 1:1M. [7] Bleacher et al., (2007), JGRE 112, doi:10.1029/2006JE002826. [8] Bleacher et al., (2011), LPSC 42, #1805. [9] McGovern and Morgan (2009) Geology, 37, 139-142, doi:10.1130/G25180A.1. [10] Byrne et al., (2009) Earth and Planetary Sci. Lett., 281, 1-13.

GEOLOGIC MAPPING OF THE MARS SCIENCE LABORATORY LANDING ELLIPSE F. J. Calef III[1], W. E. Dietrich[2], L. Edgar[3], J. Farmer[4], A. Fraeman[5], J. Grotzinger[3], M. C. Palucis[2], T. Parker[1], M. Rice[3], S. Rowland[6], K. M. Stack[3], D. Sumner[7], J. Williams[7], and the MSL Science Team, [1]Jet Propulsion Laboratory, Pasadena, CA, [2]University of Calif., Berkeley, CA., [3]Calif. Institute of Technology, Pasadena, CA, [4]Arizona State Univ., AZ, [5]Washington Univ. St. Louis, MO, [6]Univ. of Hawaii, HI, [7]Univ. of Calif., Davis, CA., [7]Univ. of New Mexico, NM.

Abstract/Introduction: Geologic context is critical for interpreting observations from the many instruments onboard the Mars Science Laboratory (MSL) rover in Gale crater. Using orbital data initially compiled for engineering tests [1] and building on the earlier work done by [2], the MSL project "crowd sourced" a geologic mapping effort of the nominal landing ellipse in preparation for tactical and strategic mission operations. Six major geologic/geomorphic units in the landing ellipse were mapped after consolidating many similar units [4,5]: alluvial fan [3,4], smooth hummocky plains, bright-toned "rugged" units, flat-lying cratered plains/surfaces, "striated" light-toned outcrops, and light-toned fractured surfaces. Initial stratigraphic models of these units have been proposed based on our traverse from Bradbury Landing to Glenelg [6]. The spatial coincidence of three of these units at Glenelg serendipitously allows the MSL Team to explore most of the major geologic units within the landing ellipse and expand our geologic knowledge to similar outcrops surrounding the north half of the mound. The mapping effort is ongoing and will continue as Curiosity investigates rocks in Yellowknife Bay [4] and on the way to Aeolis Mons (informally known as Mt. Sharp) [5].

Methodology: As part of the entry, descent, and landing (EDL) modeling efforts for the final four Mars Science Laboratory (MSL) rover landing sites [1], comprehensive visual and topographic datasets were assembled for the landing ellipse in Gale crater. Initial mapping efforts by Anderson and Bell [2] were conducted primarily with 6m/pixel Mars Reconnaisance Orbiter (MRO) Context (CTX) camera imagery. For this mapping effort, twelve MRO High Resolution Science Experiment (HiRISE) 0.25 cm/pixel stereo pairs, three 6m/pixel stereo pairs from the MRO Context (CTX) camera, all processed in Socet Set by the U.S.G.S. Astrogeology Center [ref. in 1] and a crater-wide 50 m/pixel digital elevation model (DEM) made from the Mars Express High Resolution Stereo Camera (HRSC) images were georeferenced together and mosaicked to form the base of a geographic information system (GIS). These datasets formed a "resolution pyramid" to allow mapping at scales down to a few meters using orbital data alone. Datasets were projected into an Equidistant Cylindrical projection with a center longitude and center latitude of zero, on a spherical Mars of radius 3396190 m. Whereas simple cylindrical projections are typically not ideal for mapping efforts due to distortions at mid and higher latitudes, Gale crater's location so close to the martian equator and small area creates almost no disortion in shape or area and allow directions to remain true. A 17 km x 12 km grid was developed from areocentric latitude -4.5ºN to -4.75ºN and positive east longitude 137.225º to 137.575º composed of 140 1.2 x 1.2 km (0.025º) quadrants over the extent covering the final MSL landing ellipse. Each quadrant was used to extract 0.25 cm/pixel HiRISE visible, 1m/pixel elevation, and 100m/pixel thermal inertia data [7] and these data were provided to the 39 members of the Gale Quad Mapping Team. Each team member digitized boundaries separating areas with distinct tone, texture, and morphology over the assigned quadrant(s) which were later compiled into one comprehensive map (Fig. 1). The mapping efforts have been concentrated in areas where Curiosity was likely to traverse; north of a dark basaltic dune field which serves as a natural barrier between the lower reaches of Mt. Sharp and the landing ellipse. However, due to the position of the EDL ellipse at the toe of an alluvial fan [3,4], mapping was extended northward for additional geologic context.

Geology: The geologic map presented here (Figure 1) contains 6 major units: a texturally smooth unit that makes up the Peace Vallis alluvial fan unit [3,4] with many inverted channels that are several meters vertical ("low thermal inertia fan" in [2]), a light-toned unit with sub-meter width fractures of variable length and spacing that is further subdivided by [4] ("high thermal inertia fan" in [2]), flat-lying more heavily cratered surfaces ("mound skirting" in [2]), tonally-smooth though topographically hummocky plains ("hummocky plains" in [2]), bright-toned topographically variable 'rugged' terrain unit composed of material that is not fractured, and a 'striated' (layered?) light-toned unit. Units for eolian fill/bedforms and obvious continuous ejecta blankets that occasionally covered the major units were also designated, though they are minor components. Smooth hummocky terrain was distinguished as unique and separate from [2] "hummocky plains" that exists between the northern crater rim and the fan which can contains bright smooth fill in low-lying depressions, although the distinction between these units may be minor. The rugged terrain appears outcrop up through the smooth hummocky unit as ridge or mesas outcrops. Some of the rugged terrain may have been visited by Curiousity on its way to Yellowknife bay at bedrock exposures of what appears to be

fluvially deposited gravels, such as Link (http://mars.jpl.nasa.gov/msl/images/Williams-2pia16188-br2.jpg) [9]. The majority of the smooth hummocky terrain appears as a gravelly lag mixed with other centimeter-sized angular breccia fragements of unknown origin, though some visually look basaltic. Initial mapping of the complex array of geologic units as Curiosity descends into Yellowknife Bay has occurred, but future work will be conducted to confirm those relationships [4]. Intial stratigraphic relationships have been proposed based on this mapping [5,6] and the units are in approximate stratigraphic order on the map legend, though many relationships need ground confirmation. For example, there are several spatially and topographically distinct occurrences of cratered surfaces and it is unclear whether they are stratigraphically interbeded with the other units or part of one larger contiguous unit that has since been eroded [5,6]. We do know that fan-like sources appear to feed into cratered surfaces in the northern parts of Gale (e.g. [2]), so our mapping efforts and ground investigations will help decifer the larger geologic evolution of post-impact Gale crater.

Future work: With our initial mapping complete, the MSL mapping group continues to refine mapped units along a potential rover traverse into Yellowknife bay [4] and towards the lower reaches of Mt. Sharp [5]. Our mapping will be enhanced with in-situ science observations as we progress towards the ultimate goal of sampling clay and sulfate units in the main science area at the base of Mt. Sharp.

References: [1] Golombek et al. (2012) Space Science Review, [2] Anderson & Bell (2010) Mars, 5, 76-128, [3] Palucis et al. (2013) LPSC44 [4] Sumner et al. (2013) LPSC44 [5] Rice, et al. (2013) LPSC44 [6] Stack et al. (2013) LPSC44 [7] Fergason, et al. (2012) Space Science Reviews, 170, 739-773, [8] Parker, et al. (2013) LPSC44 [9] Grotzinger et al. (2013) LPSC44.

Acknowledgements: Gale Quad Mapping team: , R. Arvidson, J. Berger, J. Blank, J. Bridges, N. Bridges, T. Bristow, F. Calef, P. Conrad, B. Dietrich, G. Dromart, L. Edgar, K. Edgett, J. Eigenbrode, J. Farmer, M. Fisk, J. Grant, S. Gupta, V. Hamilton, A. Hayes, C. Hardgrove, K. Herkenhoff, J. Johnson, L. Kah, R. Leveille, K. Lewis, N. Mangold, R. Milliken, T. Parker, M. Palucis, M. Rice, S. Rowland , D. Rubin, M. Schmidt, K. Stack, D. Sumner, D. Vaniman, R. Williams, J. Wray, A. Yingst. JPL/Caltech Copyright 2013. All rights reserved.

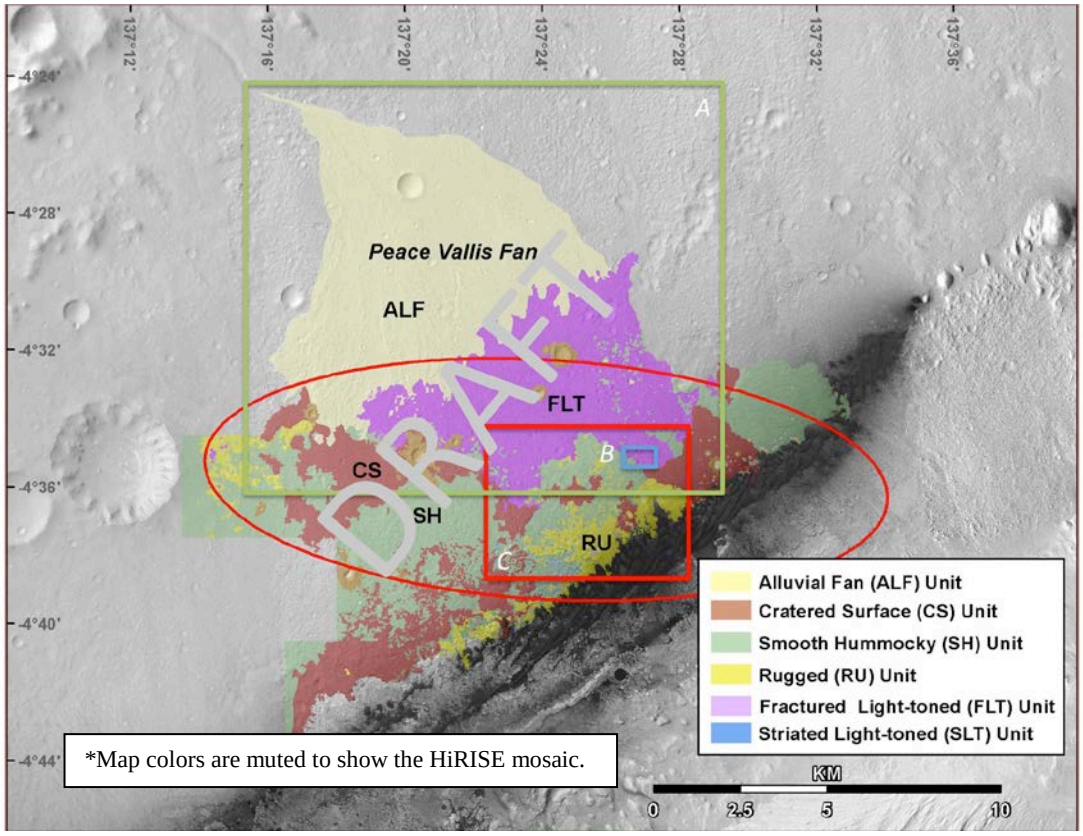

Figure 1 (below): Geology map of the MSL landing ellipse. Extent (A) overview of alluvial fan units [3,4], (B) for traverse and Yellowknife Bay units [4,6], and (C) for units along the traverse to Mt. Sharp [5]. The legend shows the approximate stratigraphic order as proposed by [6]. Red oval is the nominal landing ellipse.

GEOLOGIC MAPPING OF MTM -35137 QUADRANGLE: STYLES AND AGES OF VOLCANISM IN SOUTHERN THARSIS, MARS. David A. Crown, Daniel C. Berman, and Frank C. Chuang, Planetary Science Institute, 1700 E. Ft. Lowell Rd., Suite 106, Tucson, AZ 85719, crown@psi.edu.

Introduction: In the southern part of the Tharsis region of Mars a series of volcanic flows and plains is observed to embay and fill low-lying regions of the highlands. This investigation combines traditional geologic mapping of the 1:500K-scale MTM -35137 quadrangle [32.5°-37.5°S, 135°-140°W] with detailed flow field mapping at 1:50K-scale. This approach allows high-resolution datasets for Mars to be fully incorporated into mapping studies and documents both geologic history and the nature of volcanic processes.

Datasets: ConTeXt Camera (CTX; ~5 m/pxl) images imported into ArcGIS form the primary image base. Other datasets used for mapping are the Thermal Emission Imaging System (THEMIS) global mosaic and infrared multi-band images (~100 m/pxl), High Resolution Imaging Science Experiment (HiRISE; 0.25 m/pxl) images, and Mars Orbiter Laser Altimeter (MOLA; 128 pxl/deg) DEMs and PEDR profiles.

Mapping Overview: Geologic mapping of MTM -35137 quadrangle has been completed [1-4] (Figure 1). This includes definition of the major geologic units, identification of geologic structures, and evaluation of geologic history from stratigraphic relationships and crater size-frequency distributions. Flow field mapping is ongoing and includes delineation of flow surface textures and features, as well as identification and characterization of flow margins both within and at the edges of the flow field. MOLA PEDR profiles indicate sheet flows have thickness of 18-96 m near the flow front, with an average of ~51 m.

Stratigraphic relationships and crater counting results provide constraints on the geologic history of the map area, which includes: a) eroded Noachian cratered terrain (highlands) that stabilized in the Early Hesperian Epoch, b) an early episode of volcanism (volcanic plains) that embayed the highlands in the Early Hesperian (~3-3.5 Gy), and c) recent volcanism emplacing vast sheet flows during the Middle Amazonian Epoch (0.5-1 Gy) [2-3].

Geologic Mapping: Highlands occur as locally highstanding and rugged remnants of the heavily cratered terrain that characterizes the region south of Tharsis. The highlands appear to be extensively degraded, with surfaces exhibiting numerous fluvial channels and erosional troughs. Distinct embayment relationships are evident between the highlands and adjacent plains and flows.

Mapped plains units include: 1) a smooth unit with a mottled appearance in THEMIS IR images that covers a low-lying region at the SW corner of the map; the origin of this unit is unclear and its surface textures suggest the presence of mantling deposits typical of mid-latitudes zones on Mars; and 2) a smooth-surfaced unit that also exhibits numerous small impact craters as well as wrinkle ridges and graben; this unit is covered by younger flows but clearly embays the highlands and is interpreted to be volcanic in origin.

The majority of the quadrangle consists of young lava flows forming a large sheet complex that inundates the region [1-4]. Other mapped units include crater materials associated with the impact structures scattered across the region, crater floor materials, and a landslide deposit draped over the rim of a large crater.

Flow Field Mapping: CTX images are being used to generate detailed maps of the lava flow fields in order to interpret volcanic processes associated with their emplacement. Sheet flows typically have prominent ridged surfaces but also display knobby, platy, and smooth textures. Impact craters on the pre-flow surface influence the emplacement of flows as indicated by changes in surface ridge patterns. Formation of sheet flows partly by coalescence of large lobes is suggested in local zones where flow appears to have converged.

Zones of smooth texture containing prominent surface features are observed to disrupt local textural patterns on the sheet flows. Surface features include linear and curvilinear ridges and troughs. Some curvilinear troughs are sinuous and "channel-like" and may appear to branch or merge together. Other troughs are less sinuous and presumably related to modification of the flow crust due to differential flow; these ridges can be associated with "islands" of knobby texture. Morphologically simple linear ridges and troughs are also found within ridged, platy, and knobby textures. In some cases flow surface features change character along their lengths.

Sheet flow margins display various morphologies. Sheet flows that embay the highlands develop complex frontal shapes due to topographic irregularities in the pre-existing surface. Sheet flows emplaced over plains exhibit lobate margins suggesting lobe coalescence or differential flow at the front. A series of steep-sided, smooth plateaus is observed along sheet flow margins. Some appear to have small breakout flows at their edges. These smooth plateaus are attributed to inflation of the flow as the front stagnates. This hypothesis is consistent with their smooth surfaces, as low-velocity emplacement may limit formation of surface ridges.

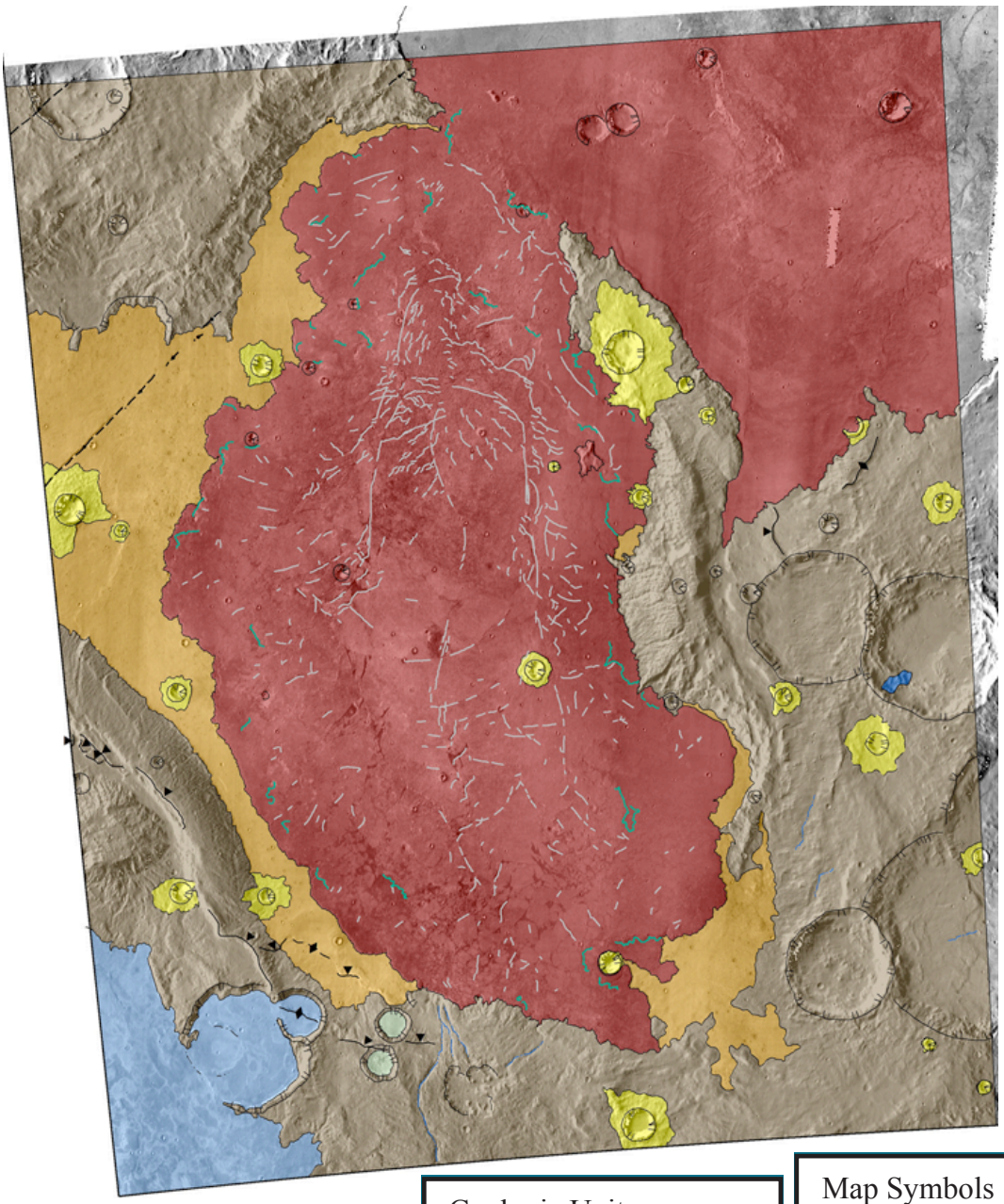

Figure 1. Geologic map of MTM -35137 quadrangle. Note that mapping of lava flow surface features is not yet complete for entire map area.

References: [1] Crown, D.A. et al. (2011), *AGU*, abstract V31A-2514. [2] Crown, D.A. et al. (2012), *LPSC XLIII,* Abstract 2138. [3] Crown, D.A. and D.C. Berman (2012), *LPSC XLIII,* Abstract 2055. [4] Crown, D.A. et al. (2013), *LPSC XLIV,* Abstract 2499.

Geology, hydrology, and astrobiological implications of Argyre, Mars

J.M. Dohm (1), R. El-Maarry (2)**,** R.J. Soare (3), J.-P. Williams (4), S.J. Conway (5), H. Miyamoto (6), and S. Maruyama (1)
(1) Earth-Life Science Institute, Tokyo Institute of Technology, Meguro, Tokyo, Japan 152-8551 (jmd@hwr.arizona.edu), (2) Physikalisches Institut, Bern Universität, Berne, Switzerland 3012, (3) Geography Department, Dawson College, Montreal, Canada H3Z 1A4, (4) Division of Geological and Planetary Sciences, California Institute of Technology, Pasadena, CA 91125, (5) Department of Physical Sciences, Open University, Milton Keynes, United Kingdom MK7 6AA, (6) The Museum, The University of Tokyo, Tokyo, Japan 113-003

1. Introduction

Using Viking and post-Viking data, the detailed geological investigation of the Argyre impact basin and surroundings (30°S to 65°S, 290°E to 340.0°E; Fig.1) has: (1) resulted in a new geologic map of the region (Fig.2); (2) revealed the stratigraphical history of the region, including distinct sequence stratigraphy marking a lake that formed shortly after the Argyre impact event and the subsequent growth of Tharsis; (3) identified local lake-containing basins (Fig.3); (4) mapped the extent of Argyre-related tectonism and its influence on the surrounding regions, which includes a geophysical perspective; (5) been compared to a CRISM-based perspective which supports impact harvesting of mantle materials and aqueous activity in drainage systems including catchment basins; and (6) detailed ancient and geologically-recent surface modification (Fig.4).

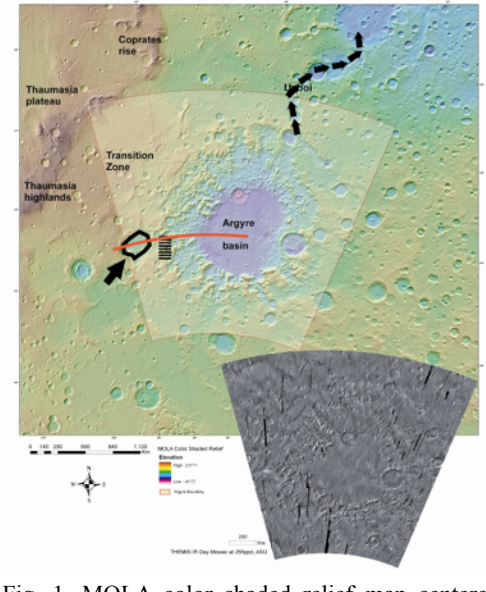

Fig. 1. MOLA color shaded relief map centered on the Argyre region (transparent outline). The image on the bottom right shows a 256 pixels/degree THEMIS IR day mosaic.The regional 1:5,000,000-scale mapping investigation includes the Argyre floor and rim, transition zone, and the southeast margin of the Thaumasia plateau [1]. Also shown is a newly identified paleolake basin (wide arrow) located on the western margin of the Argyre impact basin and the Uzboi drainage system (narrow arrows), possible spillway separating the paleolake basin from the Argyre basin at a present-day topographic interval nearing 1.5 km (dashed line), and a transect for topographic profile shown in Fig. 3 (red line).

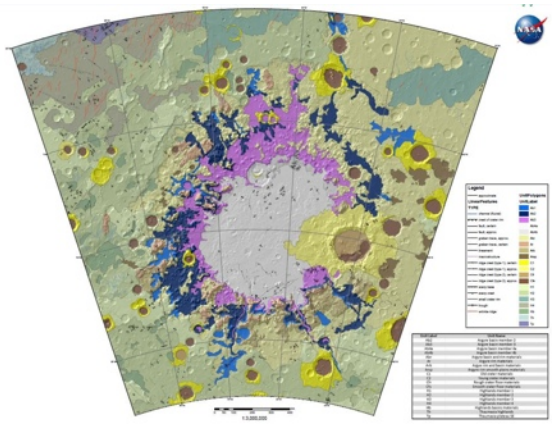

Fig. 2. Geologic map of the Argyre basin and surrounding region of Mars [2].

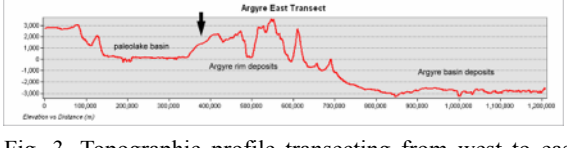

Fig. 3. Topographic profile transecting from west to east (see Fig. 1 for transect location) through paleolake basin and the Argyre rim materials and basin deposits. A topographic bench (arrow) occurs near an elevation of ~1.5 km nearing the elevation of the possible spillway divide.

2. Geology and hydrology

Argyre-impact and subsequent endogenic (Tharsis) and exogenic (impacts such as Lowell and changes in

obliquity and eccentricity) activity would contribute to the long-term water enrichment and related surface modification in and surrounding the Argyre basin until present-day. Examples of geologically-recent and/or present-day activity includes the formation of polygonal-patterned ground, gullies and possible open-system pingos [3], flow-like features of the valley-fill materials, which includes glacier-like features [4], and activity along graben-like features. Local precipitation events related to atmospheric cycling of water vapor such as from the south pole into the deep basin cannot be ruled out as a contributor to the water enrichment.

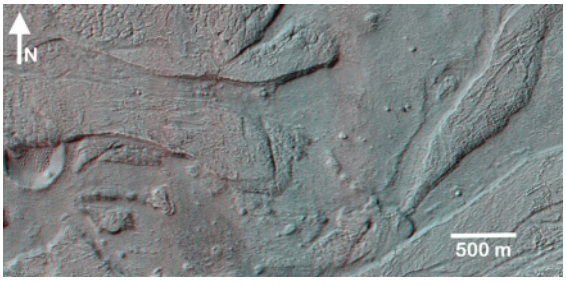

Fig. 4. Based from [4], HiRISE stereo (ESP_0028500_1425_ESP_028922_1425) image showing evidence for multiple resurfacing events by different processes (including possible glacial, alluvial, periglacial, fluvial) within the Moanda crater-valley system. The impact crater is buried by flow materials; the margin of the flow has slumped into the impact crater basin.

The Argyre impact event created a giant catchment for water and rock materials since approximately 3.93 Ga based on detailed stratigraphy and crater statistics. A giant lake was formed directly subsequent to the event, feeding the far-reaching Uzboi Vallis system [5,6], with a volume near that of the Mediteranean sea (Fig. 5); other lakes filled the impact-derived local basins as well (Fig. 3) [6]. The lakes would soon freeze and the once lacustrine environment would transition into glacial and periglacial environments [e.g., 7,8]. Through time, liquid water/water-ice would wane, though not totally being depleted, as there would be subsequent Tharsis-driven, transient hydrological cycling (including enhanced geological and climatic activities).

The giant impact produced a complex system of tectonic structures, many of which are observed to be thousands of kilometers in length and propogate all the way to the Brittle-Ductile transition. Such basement structures would serve as conduits for the migration of volatiles and heat energy into the basin region from as far away as Tharsis (tectonic structures that would transect the Argyre-Thaumasia highlands transition zone projecting into the Thaumasia plateau [1,9]).

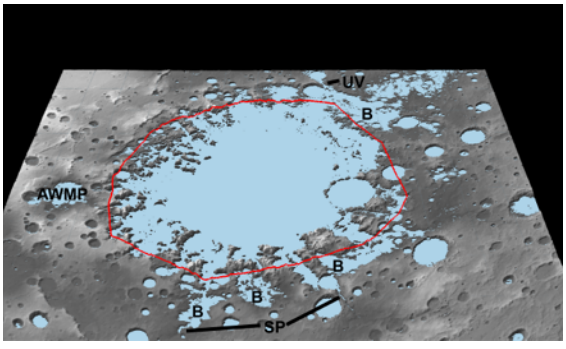

Fig. 5. Based from [6], schematic paleolake map of the Argyre basin using a maximum topographic elevation of 0 km based on MOLA topography (regions in blue). An estimated extent of the hypothesized Argyre lake based on geomorphologic and topographic analyses, as well as detailed geologic mapping is also shown (red line). In addition to the estimated extent, sapping channel systems (SP), local basins (B) which occur among the crater rim materials, and the Uzboi Vallis system (UV) correspond to the blue-highlighted region. Also shown is a small extent (near base level) of the paleolake basin located west of the primary Argyre basin. The volumes of the hypothesized AWMP and Argyre lakes are estimated to be 1.6 x 10^4 and 1.9x10^6 km^3, respectively, using MOLA. If the water level reached 1 km, then an estimated volume of is 3,051,121.6 km^3, nearing that of the Mediterranean Sea.

3. Astrobiological implications

The long-term water enrichment, heat generation from the Argyre impact, basement structures which piped water into the basin from far-reaching geologic provinces, potential nutrient-enriched primordial crustal materials [10], extant ice, potential near-surface groundwater in places, and potential venting of magma and volatiles collectively point to the Argyre basin region as a prime candidate for future exploration of possible life.

References

[1] Dohm, J. M., et al., US Geol. Survey Map I-2650, 2001. [2] Dohm, J. M., et al., US Geol. Survey Map, in preparation. [3] Soare, R.J., et al., GSA Annual Meeting and Exposition, Charlotte, North Carolina, 44, 7, 64, 2012. [4] El Maarry, M.R., et al., LPSC XXXXIV, #3064 (abstract) [CD-ROM], 2013. [5] Parker, T.J., and Gorsline, D.S., LPSC XXII, 1033-1034, 1991. [6] Dohm, J.M., et al., LPSC XXXIII, Abstract #2255 (CD-ROM), 2011. [7] Kargel, J.S., Mars: A Warmer Wetter Planet: Praxis-Springer, 557 p. [8] Kargel, J.S., and Strom, RG., Geology, 20, 3-7, 1994. [9] Dohm, J. M., et al., J. Geophys. Res. 106, 32,943-32,958, 2001. [10] Maruyma, S. et al., Geoscience Frontiers 4, 141-165, 2013.

GEOLOGIC MAPPING OF ARSIA AND PAVONIS MONTES, MARS. W. B. Garry[1], D. A. Williams[2], and J. E. Bleacher[1] [1]Planetary Geodynamics Laboratory, Code 698, NASA Goddard Space Flight Center, Greenbelt, MD 20771, william.b.garry@nasa.gov, [2]School of Earth and Space Exploration, Arizona State University, PO Box 871404, Tempe, AZ 85287.

Introduction: Arsia and Pavonis Montes are two of the three large shield volcanoes that comprise the Tharsis Montes on Mars. Detailed mapping of a limited area of these volcanoes using HRSC images (13-25 m/pixel) revealed a diverse distribution of volcanic landforms within the calderas, and along the flanks, rift aprons, and surrounding plains **[1]**. We are funded by NASA's Mars Data Analysis Program to complete digital geologic maps of both Arsia and Pavonis Montes based on the mapping style defined by **[1,2]**. Here, we report on progress from year 3 of the project **[3]**.

Data and Methods: We are mapping the two volcanoes in ArcMap 10 at 1:1,000,000 scale to produce two geologic maps for the USGS. A CTX mosaic serves as the basemap, supplemented by HRSC, THEMIS daytime IR, HiRISE, and MOLA data. Our primary objective is to show the areal extent, distribution, and stratigraphic relations of the different lava flow morphologies across each volcano to better understand their evolution and geologic history.

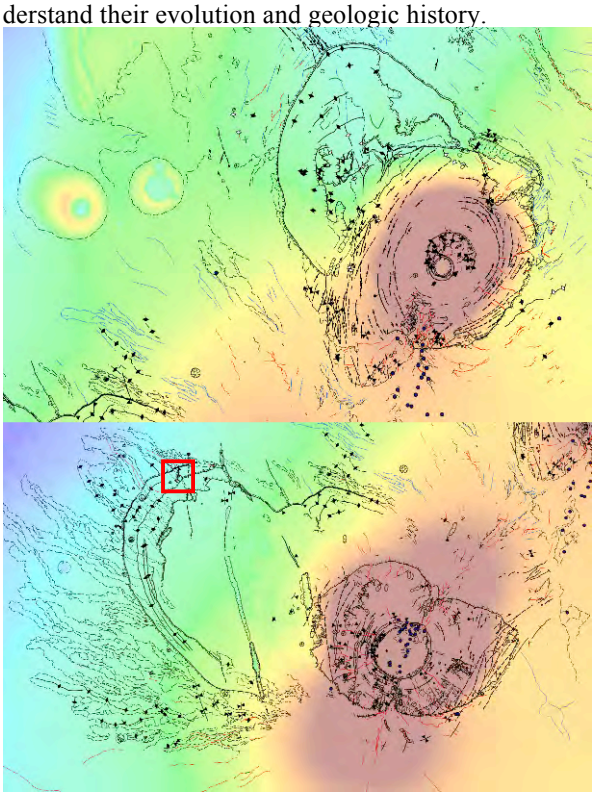

Figure 1. Current progress of the geologic mapping of Pavonis Mons (top) and Arsia Mons (bottom). Basemap is MOLA colorized topography. Location of linear cones, shown in Fig. 2, marked by red box.

Geologic Observations: Mapping objectives this year were to establish the contact between the two volcanoes and outline the boundaries of the morphologic provinces: calderas, shield, rift aprons, surficial deposits, and long lava flows (Fig. 1).

Caldera. Arsia Mons has a series of small shields on the floor of the caldera with channels that flow from the rim into the caldera and flows that breach the northeast rim. The caldera floor on Pavonis is comprised of a series of sheet-like or ponded flows.

Main Shield. The eastern flank of Arsia Mons is comprised of channeled flows, ridged units with collapsed tubes along the crest, and lava fans, while the western flank is dominated by rille-like channels and surfaces affected by processes related to the surficial deposit. Pavonis Mons is relatively featureless surrounding the caldera, but several channels and lava fans are observed along the flanks, including eruptions that occurred after formation of the circumferential graben that also overlie/embay flows that emanate from the rift aprons.

Rift Aprons. Rille-like channels separated by featureless plains occur near the chasmata on NE and SW flanks of each volcano. Flow margins begin to develop further down slope on the rift aprons. Long lava flows extend for 100s of kilometers and embay or partially bury the main flank of each volcano. We are attempting to define the boundaries of the flow fields for each rift apron to determine their spatial extent. The SW rift apron on Pavonis Mons is comprised of a small shield field and extensive series of flows that wrap counterclockwise around the base of the main flank toward Ascraeus Mons. An extensive series of flows have been mapped on the western side of Arsia Mons that have been partially buried by the surficial deposits but it is unclear if they are related to initial eruptions from the main flank or the rift aprons (Fig. 2).

Surficial Deposits. The deposits in Arsia Mons extend ~500 km away from the base of the main shield and extend ~200 km at Pavonis Mons. These deposits have been mapped and described by **[e.g. 4-6]**. Three facies within these areas are ridged, knobby, and smooth units **[4-6]**. The ridged units are found along the distal boundary of the deposits, with the knobby units occurring within the central area, and smoother facies near the base of the main flank. These are interpreted to be deposited during the retreat of cold-based glaciers **[4,5]**.

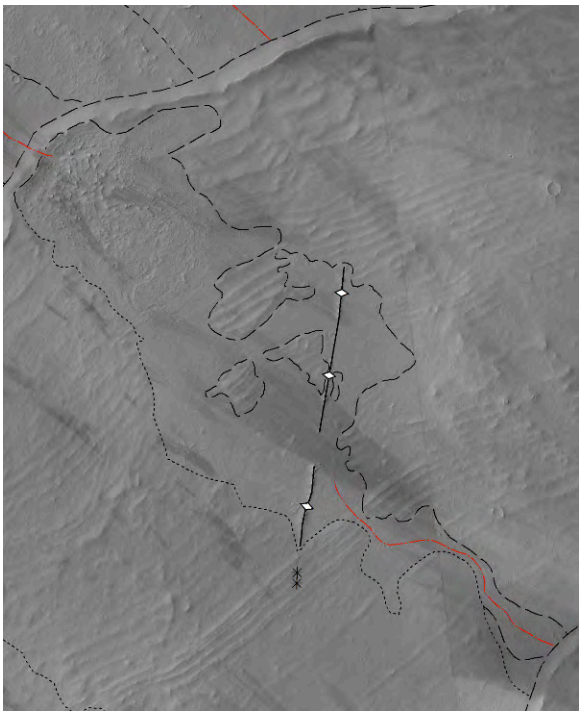

Figure 2. Linear cones and associated lava flows that appear to embay the ridged unit of the surficial deposit on Arsia Mons. Basemap is CTX mosaic.

Discussion: Mapping reveals a similar sequence of events for the evolution of both volcanoes: 1) main shield forms, 2) eruptions from the NE/SW rifts emplace long lava flows that surround the main flank, 3) eruptions wane and build up the rift aprons and shield fields, 4) glaciers deposit surficial material, and 5) localized recent eruptions along main flanks, in the calderas, and within the fan-shaped glacial deposits.

An example of recent volcanism occurs within the surficial deposits of Arsia Mons (Fig. 2). Flows emanate from a narrow, linear chain of cones in the northern extent of the deposit (Fig. 1). The flows appear to embay the ridged unit (Figs. 2,3) indicating they were emplaced after the interpreted periods of glaciation in the region. The surficial deposits at Arsia Mons have a cratering model age of <100 Ma **[4]**. This suggests the volcanism associated with the linear cones occurred within the last several 10s of Ma. We do not have a cratering model age on the linear cones at this time. However, the recognition of post-glacial volcanism would agree with previous work that suggested volcanism occurred in the last 100-200 Ma within the calderas of Arsia and Pavonis **[7]**.

Mapping of the different volcanic morphologic features has revealed a complex and diverse evolution of these volcanoes. We will continue to map the details of these volcanoes and finalize the digital geologic maps in the 4th and final year of the project.

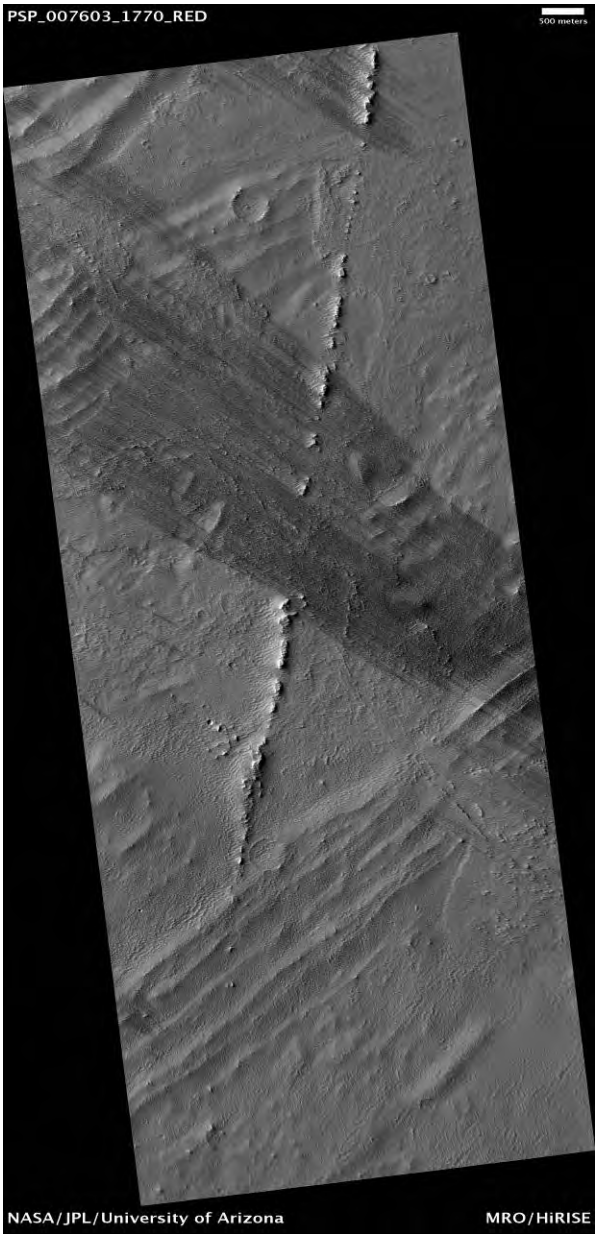

Figure 3. Linear cones and associated lava flows within the fan-shaped deposit on Arsia Mons. HiRISE Image PSP_007603_1770_RED [NASA/JPL/UofA].

References: **[1]** Bleacher J. E. et al. (2007) *JGR,112,* E04003, doi:10.1029/2006JE002826. **[2]** Bleacher J. E. et al. (2007) *JGR, 112,* E09005, doi:10.1029/2006 JE002873. **[3]** William D. A. et al. (2012) *LPSC 43,* Abstract 1528. **[4]** Shean D.E. et al. (2007) *JGR,112,* E03004, doi:10.1029/2006JE002761. **[5]** Shean D.E. et al. (2005) *JGR, 110,* E05001, doi:10.1029/ 2004JE002360. **[6]** Head J.W. and Marchant D. R. (2003) *Geology, 31,* 641-644. **[7]** Robbins et al. (2011) *Icarus, 1179-1203.*

Acknowledgements: This research is funded by NASA Mars Data Analysis Program (MDAP) grant to D.A. Williams.

NOACHIAN RESURFACING IN THE MARTIAN HIGHLANDS: ANALYSIS OF NEW GLOBAL GEOLOGIC MAP AND CRATER DATABASE. R. P. Irwin III[1], K. L. Tanaka[2], and S. J. Robbins[3], [1]Center for Earth and Planetary Studies, National Air and Space Museum, Smithsonian Institution, MRC 315, 6th St. at Independence Ave. SW, Washington, D.C. 20013, irwinr@si.edu, [2]U. S. Geological Survey, Astrogeology Science Center, Flagstaff, Arizona 86001, ktanaka@usgs.gov. [3]Laboratory for Atmospheric and Space Physics, 3655 Discovery Dr., University of Colorado, Boulder, Colorado 80309, stuart.robbins@colorado.edu.

Introduction: Previous geologic mapping and analysis of impact crater populations have identified substantial Noachian resurfacing and loss of craters in the Martian highlands. Based on Mariner 4 data, Öpik [1] noted that older Martian craters were more degraded than those on the moon and Mercury, and many small craters had been concurrently lost, a result that later studies confirmed [e.g., 2–5]. Global mapping of Mars at 1:5,000,000 and 1:25,000,000 scales based on Mariner 9 imagery included a distinction between rough ("hilly and cratered material") and smooth ("cratered plateau material") intercrater plains in the highlands, although the contacts were approximately mapped [6]. The Viking-based 1:15,000,000 global geologic map further subdivided the highlands into similar hilly, cratered, and subdued cratered units, as well as dissected, etched, and ridged units that were defined by secondary morphological features [7]. Both global maps also included mountain, basin rim, crater, and smooth plains units in the highlands.

The new 1:20,000,000 global geologic map of Mars divides highland units by age and thus has implications for the resurfacing history [8]. The map distinguishes rugged, high-relief outcrops of the Early Noachian highland unit (eNh) from the uneven to rolling, commonly layered Middle Noachian highland unit (mNh) and the plains-forming Late Noachian highland unit (lNh). These descriptions acknowledge the variable amounts of relief and resurfacing within the highlands, as prior maps had noted, but with better contact placement enabled by new mission datasets.

The purpose of this study is to evaluate highland resurfacing events and processes using the new global geologic map of Mars [8], a crater database that is statistically complete to 1 km diameter [9], and Mars Orbiter Laser Altimeter (MOLA) topography [10].

Methods: The contacts between the eNh and mNh units were commonly mapped at a break in slope separating high-relief, rugged surfaces (eNh) from sloping, less densely cratered plains (mNh) (Fig. 1). These contacts were mapped as certain along escarpments and approximate where the eNh outcrops had a less sharply defined margin. The lNh unit included buried to partially buried cratered surfaces that were typically confined to highland basins and delimited mostly by certain contacts [8, 11].

We examined the crater densities for these units in diameter (D) bins of $D–D*2^{0.5}$ km to determine if they had statistically distinct relative ages (i.e., the bin error bars, ± the square root of the crater count normalized to 1 million km^2, did not overlap). Craters that overlapped or contained unit contacts were assigned to one unit or another by inspection, and craters in the superimposed Amazonian and Hesperian impact unit (AHi) were reassigned to their subjacent unit. We used crater depth/diameter ratios from [9] and a single-factor analysis of variance to test whether crater degradation varied with unit relative age. The elevation distributions of the Noachian units in 500 m bins provided information on whether resurfacing was gravity-driven or independent of topography. Finally, we determined the relative ages of the Hellas, Isidis, and Argyre basins by counting craters superimposed on their respective highland massif units, in order to evaluate a possible link between resurfacing and basin ejecta [11].

Results: The eNh, mNh, and lNh units had statistically distinct crater retention ages in diameter bins >16 km, whereas their crater densities converged between 4 and 16 km (Fig. 2). At D<4 km, all three units had a mid-Hesperian age in Hartmann's scheme [5], consistent with the loss of all Noachian craters <4 km in diameter to ubiquitous resurfacing by that time.

Crater depth/diameter ratios were not significantly different between the eNh and mNh units. Craters in the lNh unit were mostly buried, so this analysis was not done for that unit.

We found distinct and complex elevation differences between the units, associated with their regional and local spatial distributions. The eNh unit was concentrated in the high-standing Hellas basin annulus (within one inner ring diameter, 2400 km, of the inner basin ring) and in outcrops in the region of high crustal magnetization around 180º E, where the effects of Early to Middle Noachian basin-scale impacts were minimal. The mNh unit was extensive in Arabia Terra and in highland corridors between eNh outcrops. The lNh unit mostly occupied highland basin floors.

The sequence of the largest impact basins was Hellas, then Isidis, and finally Argyre, consistent with prior work [12–14]. Hellas ejecta may have resurfaced the eNh unit, but other basins could not account for the age and full extent of Middle Noachian resurfacing.

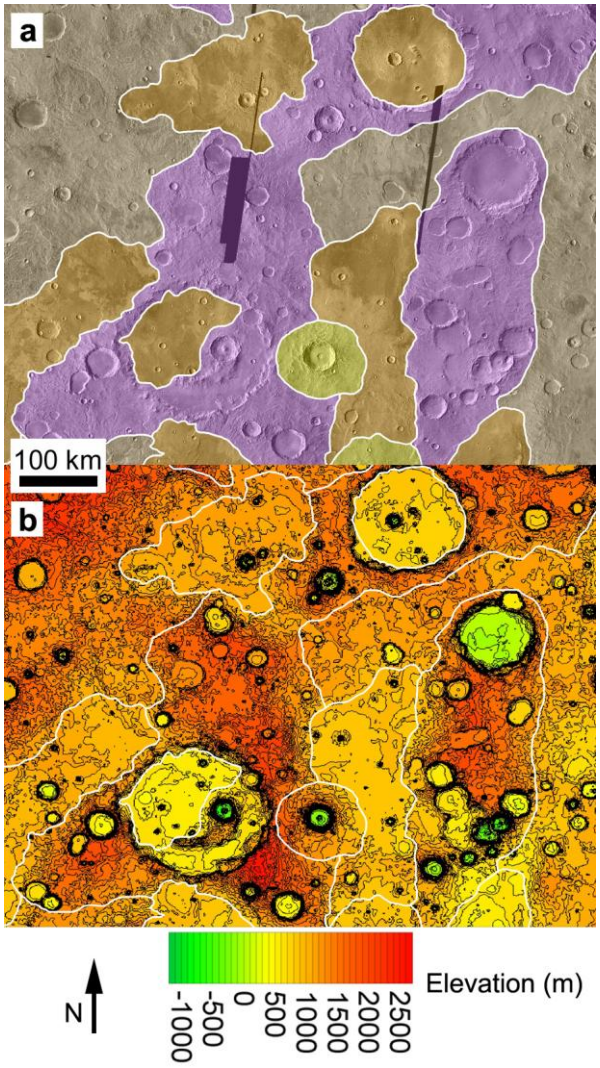

Fig. 1. (a) Example of map units eNh (purple shade), mNh (dark brown), lNh (orange-brown), and AHi (yellow) at 20–30ºS, 145–158ºE in Terra Cimmeria. (b) Same area on MOLA contour map, 100 m interval.

Discussion: The distinct relative ages of the units show that Noachian resurfacing was not spatially uniform. The lack of a relationship between crater infilling and crater density in the eNh and mNh units suggests that age was not the only important factor in crater degradation. The regional concentrations and elevation differences among the units show that Middle Noachian resurfacing was more significant in certain regions (Arabia Terra, Argyre vicinity, dichotomy boundary) and in lower-lying areas of the highland plateau than it was in higher-standing areas. Although Early Noachian Hellas ejecta resurfaced much of Mars, the Early to Middle Noachian Isidis and Middle Noachian Argyre impacts had more limited effects.

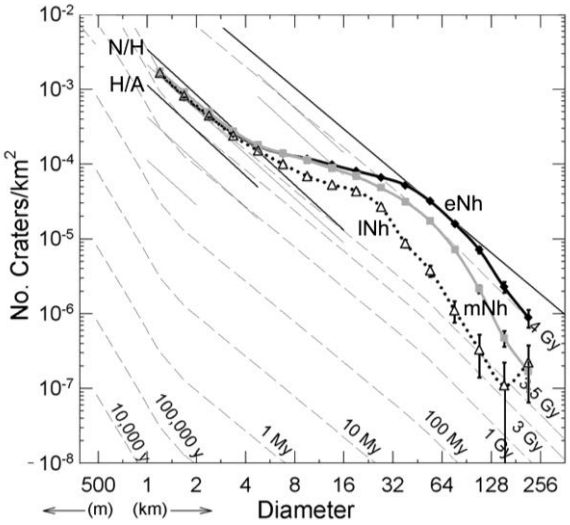

Fig. 2. Crater populations for highland units, shown on Hartmann isochron plot [5]. The Noachian/Hesperan (N/H) and Hesperian/Amazonian (H/A) boundaries are labeled. Figure adapted from [11].

These relationships along with the concentration of lNh outcrops in basins are consistent with preferential erosion of highs and deposition in lows, i.e., a gravity-driven resurfacing process. Uniform airfall mantling on a scale needed to fully resurface a cratered region could have occurred in Arabia Terra [15], but it does not appear to have been important on most of the highland plateau. Evidence for Noachian or Hesperian glaciation is lacking in the equatorial region. The most suitable candidate resurfacing processes for the mNh and lNh units are fluvial erosion and volcanism, likely with contributions from aeolian sand transport.

References: [1] Öpik E. J. (1965) *Science*, *153*, 255–265. [2] Murray B. C. et al. (1971) *JGR*, *76*, 313–330. [3] Chapman C. R. and Jones K. L. (1977) *Ann. Rev. Earth Planet. Sci.*, *5*, 515–540. [4] Malin M. C. and Dzurisin D. (1977) *JGR*, *82*, 376–388. [5] Hartmann W. K. (2005) *Icarus*, *174*, 294–320. [6] Scott D. H. and Carr M. H. (1978) *USGS map I-1083*. [7] Scott D. H. et al. (1986–1987) *USGS map I-1802*. [8] Tanaka K. L. et al. (in revision) *USGS map*. [9] Robbins S. J. and Hynek B. M. (2012) *JGR*, *117*, E05004, doi:10.1029/2011JE003966. [10] Smith D. E. et al. (2001) *JGR*, *106*(E10), 23,689–23,722, doi:10.1029/2000JE001364. [11] Irwin R. P. et al. (2013), *JGR*, *118*, 278–291, doi:10.1002/jgre.20053. [12] Werner S. C. (2008) *Icarus*, *195*, 45–60, doi:10.1016/j.icarus.2007.12.008. [13] Fassett C. I. and Head J. W. III (2011) *Icarus*, *211*(2), 1204–1214, doi:10.1016/j.icarus.2010.11.014. [14] Robbins S. J. et al. (2013) doi:10.1016/j.icarus.2013.03.019. [15] Tanaka K. L. (2000) *Icarus*, *144*, 254–266.

LOCAL-SCALE MAPPING & STRATIGRAPHY REVEAL FLUVIAL HISTORY OF AEOLIS DORSA, WESTERN MEDUSAE FOSSAE FORMATION, MARS. R. E. Jacobsen[1] and D. M. Burr[1], [1]Earth and Planetary Sciences Department, University of Tennessee, Knoxville, TN (RJacobsen@utk.edu and dburr1@utk.edu).

Background: Aeolis Dorsa (AD) are between the two westernmost lobes of the Medusae Fossae Formation (MFF). AD comprise numerous inverted fluvial features, which are interpreted to have formed by orographic precipitation, channelized run-off, induration, burial by MFF material, and exhumation by aeolian erosion [1-5 and refs. therein]. Most inverted fluvial features in AD are observed within the lowest member of the MFF [6], implying that precipitation and fluvial activity occured during the formation's early emplacement [1-5]. This abstract describes 4 stratigraphies in Aeolis Dorsa derived from local-scale mapping [5]. Local-scale mapping was coupled with a regional-scale map of the MFF [6], which provided numerical age constraints for MFF units and the inverted fluvial features. The stratigraphies are used to test 3 hypotheses about the history of fluvial activity in AD.

Hypotheses: (1) Fluvial activity was confined to a single time-interval, and by implication was the product of a unique event/process (e.g., impact). Inverted fluvial features contained within one MFF stratum would support hypothesis 1. (2) Fluvial activity was confined to separable time-intervals, and by implication occurred due to repeated events/processes (e.g., volcanism, obliquity). Inverted fluvial features in multiple non-adjacent MFF strata would support hypothesis 2. (3) Fluvial activity was successive through multiple time-intervals, and by implication occurred due to prolong conditions. Inverted fluvial features found in multiple adjacent strata would support hypothesis 3.

Methods: The testing of hypotheses involved observations of visual images from the Context Camera (CTX, 6 m/px) and High Resolution Imaging Science Experiment (HiRISE, 0.3 m/px), and topographic data from the Mars Orbiter Laser Altimeter (MOLA, 80 m spot radii) and CTX digital elevation models.

Units were mapped over visual images in ArcMap software. Fluvial units included interpreted inverted paleochannels, scrolled floodplains, and alluvial or deltaic fans [1]. Aeolian units included elongate hills of MFF material, interpreted as yardangs [7].

Topographic data, 3-point solutions for strike/dip, and principles of superposition and cross-cutting were used to determine relative stratigraphic relationships between units. These relationships were then used to sequence units into stratigraphic columns. Stratal units containing inverted fluvial features were interpreted as periods of MFF deposition, fluvial activity, induration, and inversion by aeolian erosion [1-3]. Yardangs were interpreted as periods of MFF deposition and aeolian erosion, with a wind direction interpreted from the yardang orientation [2, 8].

Four mapping areas were chosen to sample the geospatial and morphological distribution of inverted fluvial features in AD. Area identifiers are from [1, their Table 1]; locations shown in figure below. Area 35 contains large branching networks and stacked assembleges of inverted fluvial features in eastern AD. Area 43 is a fan-shaped plateau of inverted fluvial channels near the highland/lowland boundary (HLB). Area 45 contains several fan-shaped inverted fluvial landforms, ~250 km north of the HLB. Aeolis Serpens (AS) is a ~600-km-long fluvial feature in central AD that contacts several mapped geologic units [6].

Stratigraphic Observations:

Area 35: 5 units (a-e) are observed. Smooth-to-rippled surfaces comprise the lowest unit (a). Inverted channels and scrolled floodplains (unit b) stand ~110 m above the lower unit. Highly sinuous inverted channels (unit c) and a large fan-shaped network of inverted channels (unit d) superpose some inverted fluvial features of unit b. NE-SW yardangs (unit e) contact and superpose all other units (a-d).

Area 43: 3 units (a-c) are recognized. The lowest unit has NE-SW elongate textures (a) and is observable in topographic depressions, ~80 m below the plateau surface. The plateau contains N-S oriented yardangs (unit b) and inverted channels (unit c). Some yardangs on-lap and cut inverted channels of unit c, but many inverted channels are ~20 m above the plateau surface.

Area 45: 5 units (a-e) are observed. Smooth-to-rippled surfaces are the lowest unit (a) and 3-point solutions give a near horizontal slope for unit a. Above the smooth-to-rippled unit are irregular yardangs (unit b), followed by inverted fluvial channels (unit c), NW-SE oriented yardangs (unit d), and a linear cluster of exhumed fans (unit e).

Aeolis Serpens (AS): We observe 2 units recognized by [6]. Yardangs and AS are positive relief features within an Amazonian-Hesperian, lower MFF unit (HAml1). However, there are few yardangs and AS has no relief, but retains fluvial morphologies, in a mapped unit of early Amazonian, lower MFF (Aml2).

Stratigraphic Interpretations:

Area 35: At least 4 stratal units are interpreted. The topographically low smooth-to-rippled unit (a) is interpreted as eolian sedimentary fill and/or aeolian erosion with exposure of an underlying MFF stratum. One depositional episode of MFF material (≥110 m thick) is required for the formation of inverted fluvial channels and scrolled plains (unit b). A second stratum of

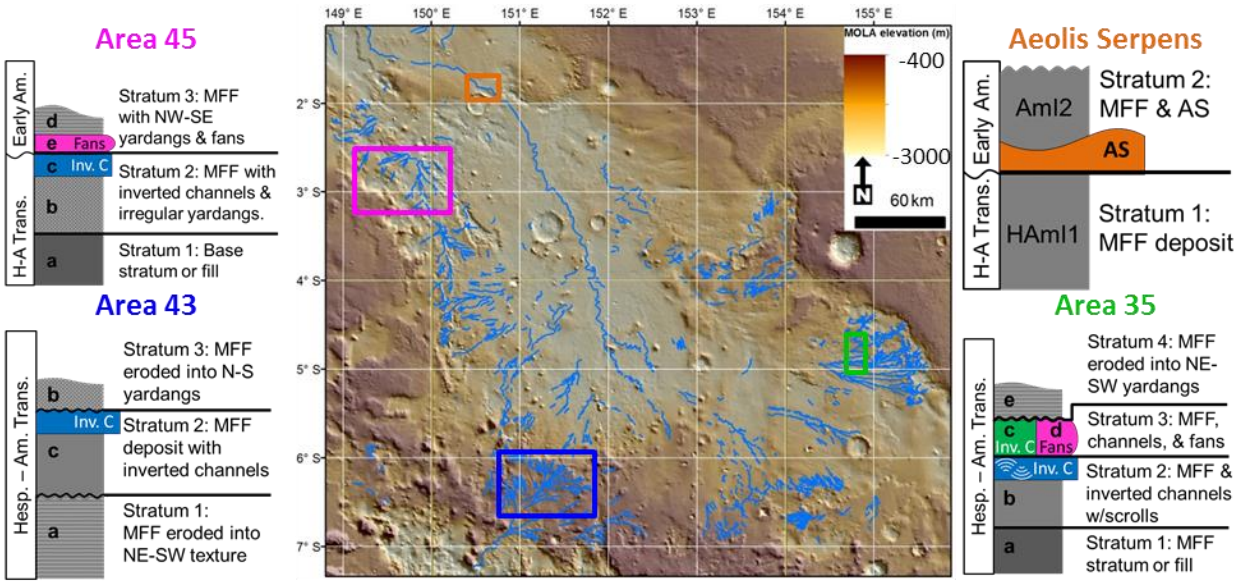

Stratigraphy in Aeolis Dorsa: Center image shows the MOLA topography and shaded relief of Aeolis Dorsa. Inverted fluvial features are delineated in blue [4]. Colored boxes correspond to local-scale mapping areas and the 4 derived stratigraphic columns (left and right). Relative ages are from crater-size freq. distributions by [6].

MFF material is required to explain the highly sinuous inverted channels (unit c) and the large fan-shaped network (unit d). Geospatial separation precludes identification of stratigraphic relationships between units c & d. NE-SW yardangs (unit e) comprise the uppermost deposit of MFF, which filled in topography, and was subsequently eroded by a NE-SW paleo-wind.

Area 43: 3 stratal units are interpreted. Topographic lows (unit a) are interpreted as areas of preferential erosion, revealing a subjacent MFF stratum that was abraded by a NE-SW paleo-wind. Following this erosion, a second stratum of MFF (≥100 m thick) was deposited. Inverted channels (unit c) indicate fluvial run-off and subsequent inversion processes occurred within this second stratum. Afterwards, a third stratum of MFF material was laid down and abraded by N-S paleo-winds, forming the on-lapping yardangs (unit b).

Area 45: At least 3 stratal units are interpreted. The smooth-to-rippled unit (a) is interpreted as eolian sedimentary fill or aeolian erosion with exposure of an underlying unit (e.g., volcanic plains). Formation of irregular yardangs (unit b) and the inverted channels (unit c) requires the deposition and erosion of at least one MFF stratum. NW-SE yardangs (unit d) and exhumed fans (units e) require the deposition and erosion of at least a second MFF stratum.

Aeolis Serpens (AS): Two MFF strata are interpreted with respect to AS. That AS cuts the early Amazonian stratum (Aml2) indicates AS formed within this younger unit. Yardangs indicate that aeolian erosion likely removed Aml2, leaving AS in positive relief above the Amazonian-Hesperian stratum (AHml1).

Discussion: The 4 areas reveal different stratigraphies. In **Area 35**, at least two adjacent strata (units b and c + d) contain inverted fluvial features, which is consistent with hypothesis 3. Based on mapping by [6], fluvial activity in Area 35 occured during the Hesperian-Amazonian transition. In **Area 43**, the single MFF stratum with inverted channels (unit c) is bound by strata with no evidence for fluvial processes, which is consistent with hypothesis 1. The age of Area 43 also corresponds to the Hesperian-Amazonian transition [6]. In **Area 45**, the two adjacent strata with inverted channels and fans are consistent with hypothesis 3. Fluvial activity in Area 45 occured during the Amazonian-Hesperian transition and the early Amazonian period [6]. Fluvial activity associated with **AS** occurred within one stratum of early Amazonian MFF material, which is consistent with hypothesis 1.

Conclusion: Local-scale stratigraphies indicate that fluvial activity in AD was geospatially diverse, hydrologically diverse (channels, fans, and AS), and temporally diverse. Fluvial activity in AD began no later than the Hesperian-Amazonian transition, with some activity also occurring in the early Amazonian.

References: [1] Burr et al. (2009) *Icarus 200*, 52-76. [2] Zimbelman and Griffin (2010) *Icarus 205*, 198-210. [3] Burr et al. (2010) *JGR 115*, E07011. [4] Jacobsen and Burr (2012) *LPS XCIII*, Abstract #2398. [5] Jacobsen and Burr (2013) *LPS XCIV*, Abstract #2165. [6] Zimbelman and Scheidt (2012) *Science 336*, 1683. [7] de Silva et al. (2010) *PSS 58*, 459-471.

EFFICIENCY OF SCALE IN PHOTOGEOLOGIC MAPPING USING THE RUNANGA-JÖRN BASIN, MARS AND THE VERDE BASIN, ARIZONA: YEAR 1 RESULTS AND YEAR 2 WORK PLAN. J. A. Skinner, Jr. and C. M. Fortezzo, Astrogeology Science Center, U.S. Geological Survey, 2255 N. Gemini Dr, Flagstaff, AZ, 86001 (jskinner@usgs.gov).

Introduction: Mars geosciences are thriving due to the recent and ongoing release of diverse, global datasets. The abundance and diversity of post-Viking Orbiter data sets – including thousands of high-resolution, single and multi-band visible and infrared images, mineralogical and compositional information, and topographic datasets – provides an unprecedented window through which we can peer into Mars' geologic past. Of particular interest insofar as the identification of evolving geologic environments are the exceptional exposures of layered strata identified in multiple locations across Mars [1-7]. It is clear that these strata reveal compelling details about local to potentially regional geologic histories. However, it is less clear that we are obtaining and propagating the most robust geologic story using current photogeologic mapping techniques or properly allowing for the cross-comparison of regions of interest. To assist in advancing the observational method and scientific value of mapping strata within highland basins, we are conducting a geologic investigation that compares the evolution of a selected Martian basin with a comparably sized, geologically similar terrestrial basin. This abstract summarizes regional details of the areas of interest as well as the progress of the investigation to date.

Regional Settings: Our investigation focuses on mapping well-exposed basin-related layered sequences on both Earth and Mars, leveraging one against the other in order to improve our understanding of local and regional geologic processes as well as photogeologic mapping techniques and approaches.

Runanga-Jörn basin, Mars. The informally named Runanga-Jörn basin (RJB) is located in Noachian- and Hesperian-age terrains on the northern margin of Hellas basin, west of Hadriaca Patera (**Fig. 1A**). RJB is 160 km long by 80 km wide. The basin's eastern margin is dissected by channels with implied drainage of the Noachian-age cratered plains from the north, east, and south. The basin surface ranges in elevation from -2450 to -2700m, with a very slight west-southwest slope (<0.1°). The western margin of RJB is generally un-dissected except for a single groove-like channel that debouches into 171.5-km-diameter Terby crater. The region is characterized by Noachian-age mountains (Early Noachian highland massif unit – eNhm of [8]), which rise >1500 m above adjacent cratered plateaus and rugged plains (Middle Noachian highland unit – mNh) and relatively lower-standing, basin-filling plains (Late Noachian highland unit – lNh). Local to regional mountains have been interpreted as crustal blocks that were uplifted and exposed by the Hellas forming giant impact [9]. Inter-montane regions are defined by topographic and structural basins that are occupied by smooth to rugged and locally dissected cratered plains of diverse (and unknown) origin.

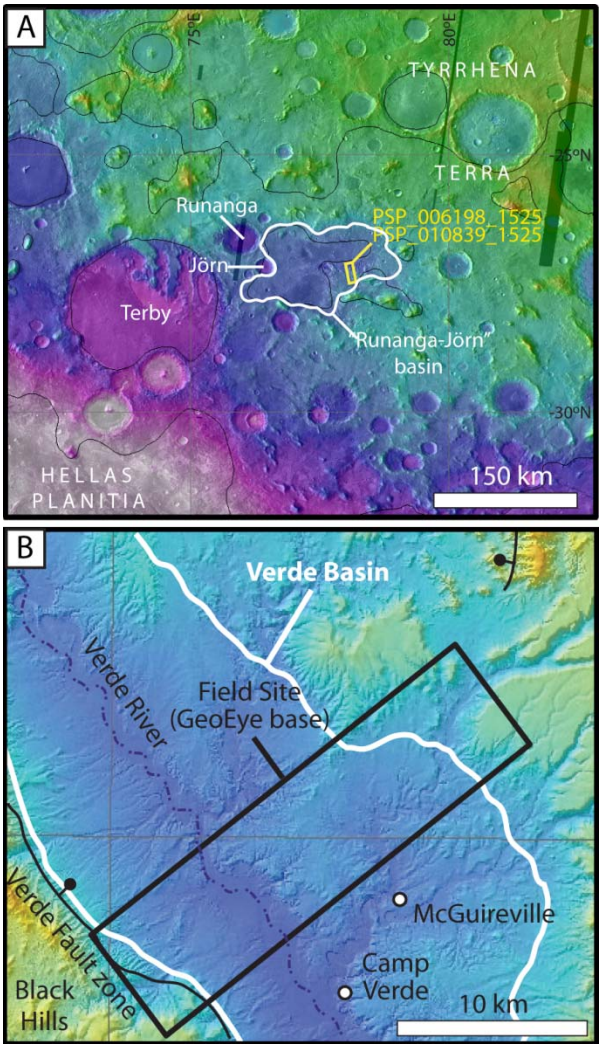

Figure 1. Regional setting of each study. (A) The Runanga-Jörn basin (RJB), Mars in MOLA shaded-relief, showing northern rim of Hellas basin. (B) The Verde Basin (VB), Arizona in NED shaded-relief, showing bounding faults and drainages. GeoEye base map extent shown by black box.

Verde Basin, Arizona. The Verde Basin (VB) is located in the southern Transition Zone province of north-central Arizona, which demarcates the structural and tectonic transition between the southern Basin and Range and the Colorado Plateau (**Fig. 1B**). The VB is

approximately 50 km long and 35 km wide and is drained by the Verde River, which runs to the southeast, sub-parallel to the southern edge of the Colorado Plateau. The VB formed by 2-3 km of normal offset along the Verde fault zone, forming a half graben (down to the northeast) that is filled with Miocene and Pliocene strata [10-14], likely accumulated due to volcanic eruptions east of VB (near Hackberry Mountain) that repeatedly blocked the southeast-flowing ancestral Verde River [14]. Periodic endorheic conditions resulted in the accumulation of lacustrine and evaporite deposits, intercalated with fault-related breccias, alluvial fans, and basaltic lava flows. These are collectively mapped as the Verde Formation [10-11], though a lack of subdivision therein inhibits a detailed reconstruction of environmental conditions through time.

Year 1 Results: Our approach to detailing, reconstructing, and conveying the geologic evolution of RJB centers on integrating both contextual mapping and local observations in order to produce a balanced (proposed to be 1:5,000 scale) geologic map of the RJB related layered strata. One element of our proposal is to determine the boundary and scale of geologic mapping, being cognizant of the stratigraphic details that require conveyance. As such, we have focused Year 1 work on the production of base maps for both areas as well as performing contextual geologic mapping for RJB and VB. Completed Year 1 work includes:

- Acquisition of GeoEye Basic Stereo product for 100 km^2 area of Verde Valley, including south-facing ramp and north-facing footwall (**Fig. 1**).
- Processing of HiRISE and GeoEye stereo-pairs into 150 cm/pixel digital elevation models using SOCET Set® software in USGS Photogrammetry Lab.
- Targeting and acquisition of HiRISE stereo-pairs for supplementing RJB geologic mapping.
- Adaptation of globally-occurring units described by [8] and [15] to the RJB at 1:250,000 scale. Base map for adaptation is a High Resolution Stereo Camera (HRSC) image mosaic and stereo-derived digital HRSC terrain models (100 m/pixel).
- Eight CraterStats-based crater counts [16] within the RJB to temporally bracket basin-related activity with model absolute ages (**Fig. 2**). Areas include regions marginal to basin floor, on the basin floor, and within the exposed layered strata. Each provides statistically meaningful primary ages, with several implicating a secondary resurfacing age.
- Geologic mapping of units and features within HiRISE image and DEM, including layer orientation measurements using LayerTools GIS plug-in [17].
- Nomenclature request submitted for RJB.

Remaining Year 1 work focuses on completing the 1:10,000 scale photogeologic mapping of units in RJB and preliminary construction for measured sections and fence diagrams with RockWorks® software. Work on the VB includes adaptation of the published 1:100,000 scale regional map [11] and preliminary mapping and layer analyses.

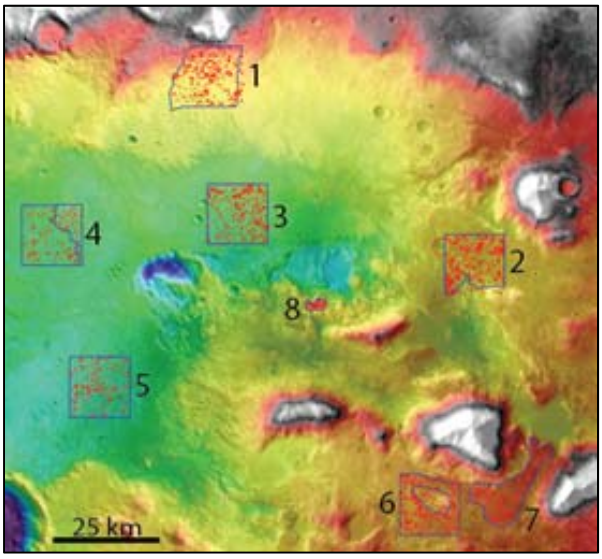

Figure 2. HRSC color-shaded relief overlying HRSC images showing western RJB. Blue boxes indicate extent of areas counted. Red circles indicate craters counted.

Year 2 Work Plan: The second full year of this three-year investigation focuses on completing 1:10,000 contextual maps and 1:1,000 scale measured stratigraphic sections for both RJB and VB. Once completed, we will conduct field-based components of VB to check the validity of our mapping strategy and the accuracy of measured sections and correlated units.

References: [1] Wilson, S.A. et al. (2007) *JGR*, 112, E08009. [2] Grant, J.A. et al. (2008) *Geology*, 36, 195-198. [3] Hynek, B.M. and Phillips, R.J. (2008) *Geology*, 29, 407-410. [4] Lewis, K.W. et al. (2008) *JGR*, 113, E12S36. [5] Pondrelli, M. et al. (2008) *Icarus*, 197, 429-451. [6] Wray, J.J. et al. (2009) *Geology*, 37, 1043-1046. [7] Ansan, V. et al. (2011) *Icarus*, 211, 273-304. [8] Tanaka, K.L. et al. (in review), *USGS SIM*. [9] Schultz, P.H. et al. (1982) *JGR*, 87, 9803-9820. [10] Twenter, F.R. and Metzger, D.G. (1963) *USGS Bulletin*, 1177, 132 p. [11]Weir, G.W. et al. (1989) *USGS I-1896*, 1:100K scale. [12] Karlstrom T.N.V. et al. (1983) *USGS MF-1567-A*. [13] Ulrich, G.E. et al. (1983) *USGS MF-1558-A*. [14] Nations, J.D. et al. (1981) *AZ Geo Soc. Digest*, 13, 133-150. [15] Greeley, R. and Guest, J. (1987) *USGS I-1802-B*, 1:15M scale. [16] Michael, G.G. and Neukum, G. (2010) *Plan. Sci. Lett.*, 294. [17] Kneissl, T. et al. (2011) *Plan. Space Sci.*, 59.

THE NEW GLOBAL GEOLOGIC MAP OF MARS AND A REVISED RESURFACING HISTORY. K. L. Tanaka[1], C. M. Fortezzo[1], J. A. Skinner, Jr. [1], T. M. Hare[1], and S. Robbins[2], [1]U.S. Geological Survey, Astrogeology Science Center, 2255 N. Gemini Dr., Flagstaff, AZ, 86001, USA, [2]University of Colorado, Boulder, CO, USA, (ktanaka@usgs.gov).

Introduction: A new global geologic map of Mars has been completed in a digital, geographic information system (GIS) format using geospatially controlled altimetry and image data sets [1]. The map reconstructs the geologic history of Mars, which includes many new findings collated in the quarter century since the previous, Viking-based maps [2] were published, as well as other discoveries that were made during the course of the mapping using the new data sets. The technical approach enabled consistent mapping that is appropriate not only for the map's 1:20,000,000 scale but also for its likely widespread use. Each geologic unit outcrop includes basic attributes regarding identity, location, area, crater densities, and chronostratigraphic age. In turn, units are grouped by geographic and lithologic types, which provide synoptic global views of material ages and resurfacing character for the Noachian, Hesperian, and Amazonian Periods.

Digital Map Product: The new global geologic map of Mars at 1:20,000,000 scale [1] was produced using Esri's ArcGIS software. Map layers are registered to the Mars Global Surveyor's (MGS) Mars Orbiter Laser Altimeter (MOLA) global digital elevation model (DEM; 463 m/pixel resolution at the equator) [3]. Mapping efforts relied heavily on morphologic observations from the MOLA DEM as well as global mosaics of Mars Odyssey (ODY) mission's Thermal Emission Imaging System (THEMIS) daytime and nighttime infrared images at 100 m/pixel [4]. We applied photogeologic mapping techniques similar to those described in [5-6] to identify and discriminate 44 geologic units (forming ~1300 outcrops) and 12 linear feature types (~3500 individual features mapped). These map layers collectively document major episodes of material emplacement, terrain development, and surface modification.

Units are delineated by primary morphologic, thermal/albedo, and topographic characteristics that we interpret were established during unit emplacement, avoiding, where possible, secondary features resulting from subsequent tectonic and (or) erosional modification (i.e., resurfacing). Each map unit is assigned an age according to the Martian chronostratigraphic periods and epochs [7-8], as governed by superposition relations and impact crater densities. In addition, the units are grouped into geographic (highland, lowland, transitional, basin, polar, and apron) and lithologic (volcanic and impact) categories.

Age Dating: Each Martian chronologic epoch has crater-density defined boundaries that are fit to widely used crater production and chronology functions [9-10]. Crater counts were obtained using two approaches. The first consisted of counts of selected typical unit surfaces for craters as small as 100 m; results from this approach are described in [11]. The other method involved the intersection of the geologic map units with the global crater database of Robbins and Hynek [12] that documents the location, diameter, and other morphologic attributes of >300,000 craters larger than 1 km in diameter.

Overall, these age determinations enabled grouping the units by age, resulting in a chronostratigraphic map (Fig. 1), as well as summaries of the areas (Fig. 2) and resurfacing rates (Fig. 3) for each unit group by epoch. Areas and rates are calculated on an age-based proportion scheme that relies on model chronologies. Here, we show example results using the Neukum chronology function, but we have also calculated results based on the Hartmann function. (More results are shown in [13].)

Chronostratigraphic Map Summary (Fig. 1): The Noachian (46% of total surface area) shows the dominance of exposed ancient highland terrain on Mars with relatively minor volcanic and basin materials. Some isolated outcrops occur within the northern lowlands. Crater preservation as a function of age and terrain indicates that fluvial erosion and local infilling such as by sedimentation and volcanism were dominant Noachian resurfacing processes [14].

Exposed Hesperian rocks (22% areal coverage) infill the northern lowlands and large impact basins and form the earliest polar deposits and major extents of the Tharsis and Elysium volcanic rises. Parts of the highland boundary retreated, and canyons and chaotic terrain formed by tectonism, incision, and collapse in Valles Marineris and nearby highland areas. Scattered impact craters dot the highland landscape.

The Amazonian (32% areal coverage) shows continued volcanism in the Tharsis and Elysium regions and local mass-wasting and accumulation of sediments along the highland-lowland transition region. Also, aprons formed around Olympus Mons and Tharsis Montes. Remnants of a Middle Amazonian lowland unit [15] and other basin and volcanic materials cover large patches of the northern plains. A proportion of the scattered outcrops of impact material in the highlands are Amazonian age. The polar plateaus largely formed at this time.

Resurfacing History (Figs. 2 and 3): We find that Noachian highland surfaces overall have high percentages of their areas now dated as an epoch or two older

than in the Viking mapping [2] (with consequently modified resurfacing rates of those reported by [16]). Pristine impact craters ≥3 km in diameter occur in greater density on (1) Hesperian terrain (which is volcanically rich) and (2) in a vast Amazonian and Hesperian volcanic unit. This contrasts with their deficit on heavily cratered and otherwise softened Noachian terrain. These observations are likely due to the relatively stronger, less-impacted yet lava-rich materials making up the younger units. Reconstructions of resurfacing of Mars by its eight geologic epochs using the Hartmann and Neukum chronology models indicate high rates of highland resurfacing during the Noachian, modest rates of volcanism and transition zone and lowland resurfacing during the Hesperian, and low rates of mainly volcanic and polar resurfacing for the Amazonian. An increase in Late Amazonian resurfacing rates may be due in part to exposure bias, in which a higher proportion of younger surfaces remain exposed versus that of older surfaces. This bias may be especially effective in volcanic regions where recurrent eruptive activity has taken place for most of the history of the planet.

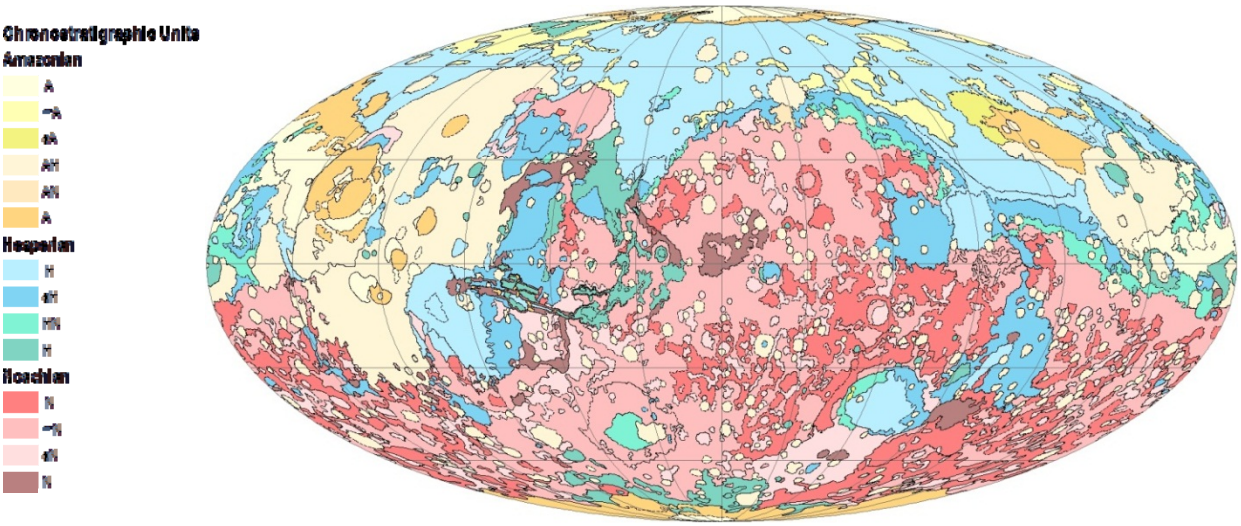

Figure 1. Chronostratigraphic map of Mars. Some units span multiple epochs or periods.

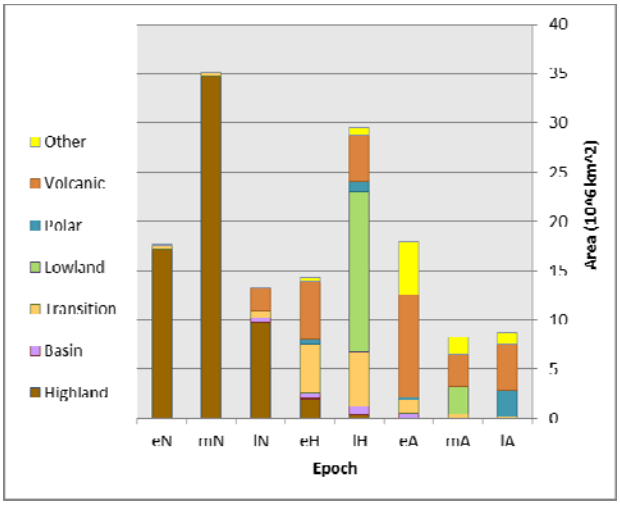

Figure 2. Resurfaced areas on Mars per unit group and epoch, Neukum chronology model.

References: [1] Tanaka K.L. et al. (in review) *USGS SIM.* [2] Scott D.H. et al. (1986-87) *USGS Map I-1802-A-B-C.* 004. [3] Smith D.E. et al. (2001) *JGR, 106,* E10. [4] Edwards C.S. et al. (2011) *JGR, 116,* E10008. [5] Tanaka K.L. et al. (2005) *USGS SIM-2888.* [6] Tanaka K.L. and Fortezzo C.M. (2012) *USGS SIM-3177.* [7] Scott D.H. and Carr M.H. (1978) *USGS Map I-1083.* [8] Tanaka K. L. (1986) *JGR, 91,* E139-E158. [9] Hartmann W.K. and Neukum G. (2001) *Space Sci. Rev. 96,* 165–194. [10] Werner S.C. and Tanaka (2011) *Icarus, 215,* 603-607. [11] Platz T. et al. (in press) *Icarus.* [12] Robbins S. J. and Hynek B. M. (2012) *JGR, 117,* E05. [13] Tanaka K.L. et al. (in review) *PSS.* [14] Irwin R.P. III et al. (2013) *JGR, 118,* doi:10.1002/jgre.20053. [15] Skinner J.A. Jr. et al. (2012) *Geology, 40,* 1127-1130. [16] Tanaka K.L. et al. (1988) *PLPS XVIII,* 665-678.

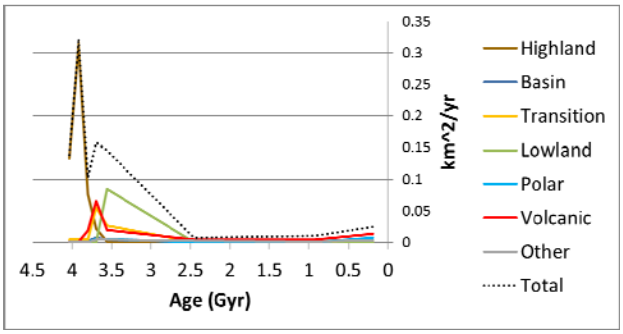

Figure 3. Resurfacing rates on Mars per unit group and mean age of epoch, Neukum chronology model.

THE HALE IMPACT EVENT AND ASSOCIATED MODIFICATION OF SOUTHERN MARGARITIFER TERRA, MARS S. A. Wilson[1] (purdys@si.edu) and J. A. Grant[1] (grantj@si.edu), [1]Center for Earth and Planetary Studies, National Air and Space Museum, Smithsonian Institution, 6th at Independence SW, Washington, DC, 20560.

Introduction: The southern Margaritifer Terra region on Mars preserves a long geologic history of water-related activity. The evolution of Uzboi Vallis (centered ~28ºS, 323ºE, **Fig. 1**), adjacent plains, and alluvial deposits, as mapped in USGS quadrangles -20037, -25037, -30037 and -30032, will help constrain the relative timing and duration of fluvial modification and lacustrine processes in the surrounding area (**Fig. 1**).

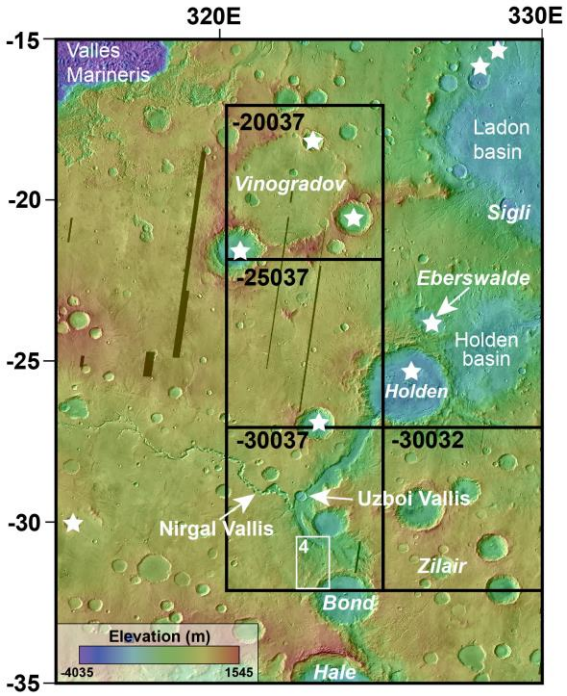

Figure 1. Southern Margaritifer Terra indicating USGS map quadrangles (black boxes), major place names, and location of Fig. 4 (white box). Craters hosting alluvial fans (stars) [12-13] are ~500+ km from Hale crater. MOLA over THEMIS day IR.

Regional Geologic History: Uzboi Vallis is the southernmost segment of the northward-draining Uzboi–Ladon–Morava (ULM) meso-scale outflow system that dominates drainage in southwest Margaritifer Terra [1-4]. The ULM drainage was likely incised during the late Noachian to Hesperian [2]. Craters Hale (125 x 150 km diameter) and Bond (111 km diameter) interrupt the southern end of the system and have destroyed the probable source outlet from Argyre basin [2-3] (**Fig. 1**). The northern end of Uzboi is blocked by Holden crater, thereby creating an enclosed basin that filled as a large paleolake in the Hesperian [5]. Morphologic evidence suggests the Uzboi lake reached to ~ -350 m relative to the MOLA datum and exceeded 4000 km^3 [5] before overflowing and draining into Holden crater [6]. Hale crater formed near the Amazonian-Hesperian boundary [7] or perhaps during the early-to-middle Amazonian [8].

Hale likely formed as an oblique impact from the southeast [8-10] and its ejecta and associated deposits have been mapped in the southern portion of the map area [8]. Modeling of Hale suggests the impact dispersed melts and intense winds over an area exceeding 5 million km^2, creating a field of secondary craters, wind streaks and scours as far north as Valles Marineris [9]. Previous geomorphic mapping of Hale crater indicates that channels originating from, incising and transporting material from its ejecta were created or modified by water that was mobilized during the impact event, emplacing fluidized debris flow lobes over an extensive region [8]. We present morphologic evidence that deposits associated with the Hale impact are likely more extensive than previously mapped [8], reaching into and modifying Uzboi Vallis and the surrounding plains.

Possible Hale-Related Deposits in Uzboi Vallis and Surrounding Plains: The deposits are sourced near the rim of Hale and flow into pre-existing valleys, topographic depressions, and craters [7]. Many craters in the circum-Hale region are significantly infilled by the deposits [8], possibly burying evidence of older alluvial deposits [11]. The deposits are often darker-toned than bounding surfaces, smoother (at scales of 10s to 100s of meters), and embay secondary craters from Hale, thereby constraining the timing of their emplacement. West of Bond crater, the deposits locally form lobes with distinct margins after passing through topographic constrictions (**Fig. 2**).

Although most of the deposits are relatively smooth and featureless, the surfaces of some flow lobes are characterized by ridges. Some of the ridges are roughly parallel and oriented perpendicular to the presumed direction of flow, similar to morphologies associated with some lava flows (**Fig. 3**). Light-toned, meter-scale boulders, aeolian bedforms and extensive cracks (some that cross-cut ridges) are common on lobe surfaces, and layering is not evident. Local aeolian erosion of the distal margins of the lobes implies a fine-grained component, perhaps produced by weathering. The surface of the lobes and associated deposits lack obvious secondary craters from Hale, suggesting these deposits post-date the initial formation of Hale.

These materials flowed into Bond crater and low-lying terrain to the north, occupying pre-existing valleys (**Fig. 4**). Although the deposit appears to thin

considerably with distance from Hale, the material continues to embay secondary craters from Hale and the margins of this smooth, dark-toned deposit on the southern bank of Uzboi can be readily mapped (**Fig 4**).

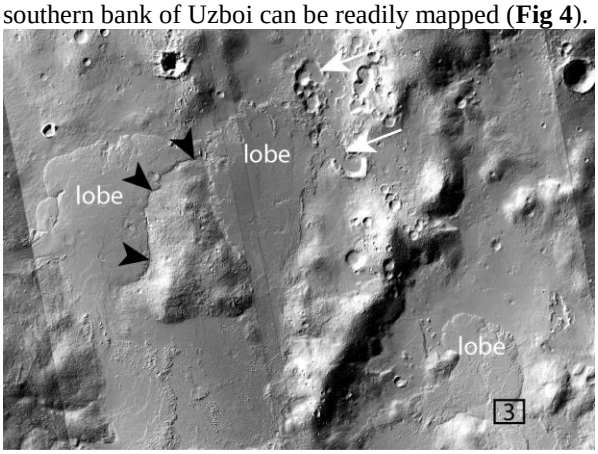

Figure 2. Flow lobes in low lying terrain west of Bond (see Figs. 1 and 4 for context) form distinct margins (black arrows) and embay secondary craters from Hale (white arrows). Box shows location of Fig. 3. Image width is ~37 km across, subframes of CTX images P18_008259_1473 and P21_009050_1472.

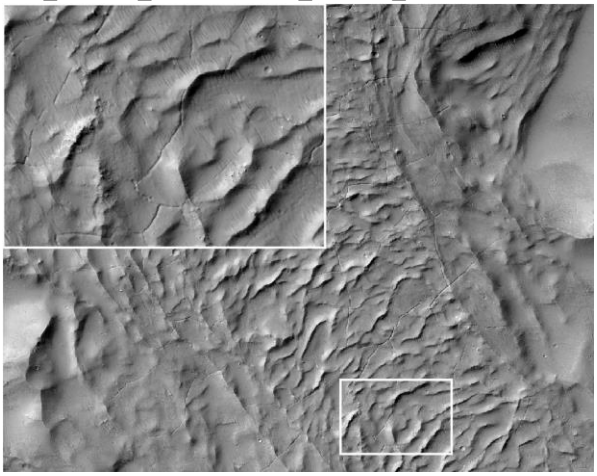

Figure 3. Roughly parallel ridges are oriented perpendicular to the direction of northerly flow (image ~1.7 km across, see Fig. 2 for context). Inset shows light-toned boulders, cracks and small aeolian bedforms. Subset of HiRISE P07_003565_1479 (~50 cm/pixel).

Implications: Because the Hale-related deposits are younger than deposits previously associated with Uzboi Vallis, they provide an additional, later chapter in the history of the ULM system. The Uzboi lake [5] formed and drained before the Hale impact and provided the mechanism for localized resurfacing of the trunk and tributaries of Uzboi Vallis. Nirgal Vallis is the largest tributary to Uzboi (**Fig. 1**), but its relative age, origin and role in the formation of the lake in Uzboi is not well understood [e.g., 5]. Older deposits at the confluence of Nirgal and Uzboi associated with the initial incision of Nirgal may be buried by the later Hale-related flows. There are no obvious Hale secondaries on the floor of Nirgal Vallis, but this may be due to the small width of the valley, subsequent backwasting of valley walls, infilling by aeolian or Hale-related deposits, or inadequate coverage by high-resolution images.

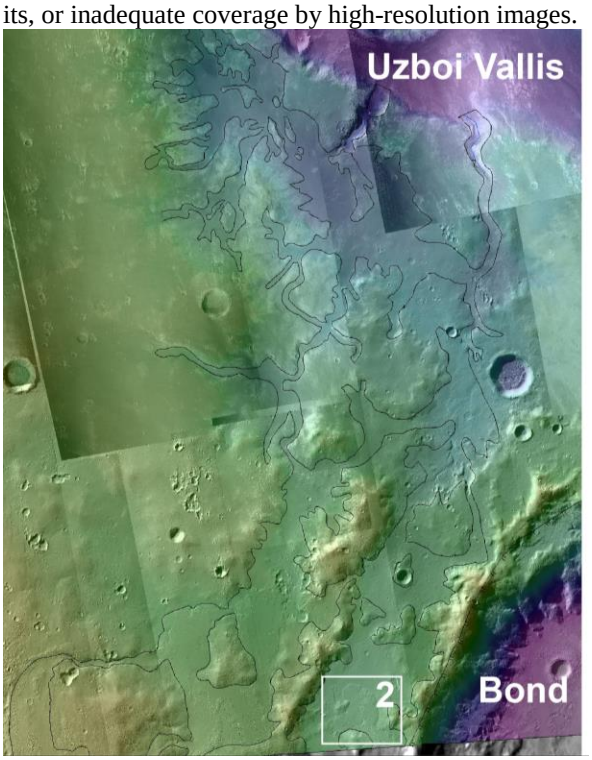

Figure 4. Preliminary draft of linework showing margins of possible Hale-related deposits that flowed north into pre-existing depressions and valleys toward Uzboi Vallis (see Fig. 1 for context). Image is ~80 km across. MOLA over CTX mosaic.

References: [**1**] Grant, J.A., 1987, Advances in Planetary Geology, NASA Tech. Memo. 89871, 1–268. [**2**] Grant, J.A., Parker, T.J., 2002, JGR, 107, doi:10.1029/2001JE001678 [**3**] Parker, T.J., 1985, M.S. Thesis, California State University. [**4**] Saunders, S.R., 1979, USGS Map I-1144. [**5**] Grant et al., 2011, Icarus, doi:10.1016/j.icarus.2010.11.024 [**6**] Grant, J.A. et al., 2008, Geology, 195–198, doi:10.1130/G24340. [**7**] Cabrol, N. A., et al., 2001, Icarus, 154, 98–112, doi:10. 1006/icar.2001.6661. [**8**] Jones et al., 2011, Icarus, doi:10.1016/j.icarus.2010.10.014. [**9**] Herrick, R.R., Hessen, K., 2006, Meteorit. Planet. Sci. 41 (10), 1483–1495. [**10**] Schultz, P.H., K.E. Wrobel, 2012, JGR, 117, doi:10.1029/ 2011JE003843. [**11**] Grant, J.A. and Wilson, S. A., 2011, *GRL*, 38, L08201, doi:10.1029/2011GL046844. [**12**] Moore, J.M., and A.D. Howard, 2005, *JGR*, 110, doi:10.1029/2005 JE002352. [**13**] Wilson et al., 2013, LPSC Abstract #2710.

THE GEOLOGY OF VESTA QUADRANGLE AV-9 NUMISIA. Buczkowski, D.L.[1], Wyrick, D.Y.[2], Yingst, R.A.[3], Williams, D.A.[4], Garry, W.B.[5], Mest S.[3], Kniessel T.[6], Scully, J.E.C[7], Nathues, A.[8], LeCorre, L.[3], Reddy, V.[3], DeSanctis, M.C.[9], Ammannito, E.[9], Frigeri, A.[9], Preusker, F.[10], Roatsch, T.[10], Raymond, C.A.[11], Jaumann, R.[10], Pieters, C.M.[12] Russell, C.T[7]. [1]JHU-APL, Laurel, Maryland, USA; [2]SwRI®, San Antonio, Texas, USA; [3]PSI, Tucson, Arizona, USA; [4]ASU, Tempe, Arizona, USA; [5]Goddard Space Flight Center, Greenbelt, Maryland, USA; [6]Freie Universitaet Berlin, Berlin, Germany; [7]UCLA, Los Angeles, California, USA, [8]Max Planck Institute, Katlenburg-Lindau, Germany, [9]INAF-IAPS, Rome, Italy;; [10]DLR, Berlin, Germany; [11]JPL, California Institute of Technology, Pasadena, California, USA; [12]Brown University, Providence, Rhode Island, USA

Introduction: NASA's Dawn spacecraft arrived at Vesta on July 16, 2011, and collected imaging, spectroscopic, and elemental abundance data during its one-year orbital mission. As part of the geological analysis the Dawn Science Team created geologic maps of Vesta at the global scale [1] and as a series of 15 quadrangle maps. We here concentrate on our mapping and analysis of quadrangle Av-9 Numisia (Fig. 1).

Geologic Setting: The Av-9 Numisia quadrangle is located in the equatorial region of Vesta, extending from ±22° latitude and from 216º - 288º E longitude. The quadrangle is dominated by Vestalia Terra (VT).

Data: Clear filter (monochrome) Framing Camera (FC) Low-Altitude Mapping Orbit (LAMO) images (spatial resolution ~20-25 m/p) were mosaicked to make the quadrangle base. Topography of Av-9 is observed in a colororized Digital Terrain Model (DTM) derived from Survey orbit FC data [2]. Variations in surface composition are revealed by Visible & Infrared Spectrometer (VIR) hyperspectral images from Survey (700 m/pixel) and Low-Altitude Mapping Orbit (HAMO) (200 m/pixel) and FC color ratio images (250 m/pixel) from Survey orbit.

Compositional Information: FC color ratio images using standard *Clementine* ratios [Red (750/430 nm); Green (750/920 nm); Blue (430/750 nm)] [3] show compositional variations within the Numisia quadrangle. Further evaluation with VIR investigated the significance of these color variations and identified deposits of OH [4] and diogentite [5] against a primarily howarditic background [6].

Geologic Units and Features: We use the material units and structures produced for the HAMO-based global geologic map of Vesta [1], except where updated and modified to take into account the unique features of Av-9 quadrangle.

Vestalia Terra: VT is a distinct, topographically high region of Vesta bound by steep scarps (Fig.2). The region is albedo-bright in clear filter FC images, compared to surrounding terrains. The large number of craters with "colorful" ejecta on VT implies that the region has a diverse composition. Although crater counts of the surface of southern VT suggests an age similar to the other cratered highlands on Vesta (3.7 Ga using the lunar-derived chronology [7]), superposition principles suggest that the VT plateau itself is older than the crater dating would suggest. The plateau is cut on all sides by ancient basins (e.g. Rheasilvia, Veneneia, Ferralia) indicating that the plateau is even older [8].

"Dark ribbon": The "dark ribbon" is a feature primarily evident in FC color ratio data but also discernable in clear filter data as a roughly linear unit of albedo-dark material crossing VT from the northwest to the southeast. The ribbon is cut by Numisia crater, whose wall stratigraphy shows a dark layer that displays the thickness of the dark ribbon material.

It has been suggested that the dark ribbon is ejecta from Drusilla crater directed into a channelized flow within a linear topographic low on the top of the VT plateau [8]. Drusilla is an OH-bearing craters [4] and so it is hypothesized that the great extent the dark ribbon travels from the crater is due to channelization in combination basal glide over impact-released gases [8].

Pit crater chains: While the other equatorial quadrangles on Vesta display numerous wide and flat-floored troughs, Av-9 does not [9]. There are, however, three large pit crater chains: Robigalia and Albalonga Catena, and an unnamed feature. Component merged pits show signs of collapse but distinct fault faces can also be observed. A strong correlation between pit crater chains and fault-bounded graben has been observed on other planetary bodies [10]. The VT pit crater chains are roughly aligned with the equatorial flat-floor troughs [9].

Brumalia Tholus: The topography of Av-9 reveals the presence of an elongate hill named Brumalia Tholus in the southeast of the quadrangle [11]. Albalonga Catena is in line with the axis of Brumalia to both the west and east. FC color data shows material of a distinct composition which appears to be moving downslope on the northern flank of the hill. Teia crater, which impacted Brumalia, has albedo-bright and "colorful" ejecta with a distinct geomorphic texture; VIR analysis has established that this ejecta is diogenitic [5]. These observations have led to the suggestion that Brumalia Tholus represents a magmatic instrusion on Vesta, possibly a dike or a laccolith [11].

References: [1] Yingst et al (in review) *JGR* [2] Preusker et al (2012) LPSC abs 2012 [3] Reddy et al

(2012) *Science* 336, 700-704 [4] De Sanctis et al (2012) *ApJ* doi:10.1088/2041-8205/758/2/L36 [5] De-Sanctis et al (2013) *EPSC* abs [6] DeSanctis et al (2012) *Science* 336, 697-700 [7] Schedemann et al (in review) [8] Buczkowski et al (in review) *Icarus* [9] Wyrick et al (2004) *JGR* doi:10.1029/2004 JE002240 [10] Buczkowski et al (2012) *GRL* doi:10.1029/2012 GL052959 [11] Buczkowski et al (2013) *LPSC* abs 1996.

Additional Information: The authors gratefully acknowledge the support of the Dawn Instrument, Operations, and Science Teams. This work was funded by the Dawn at Vesta Participating Science Program.

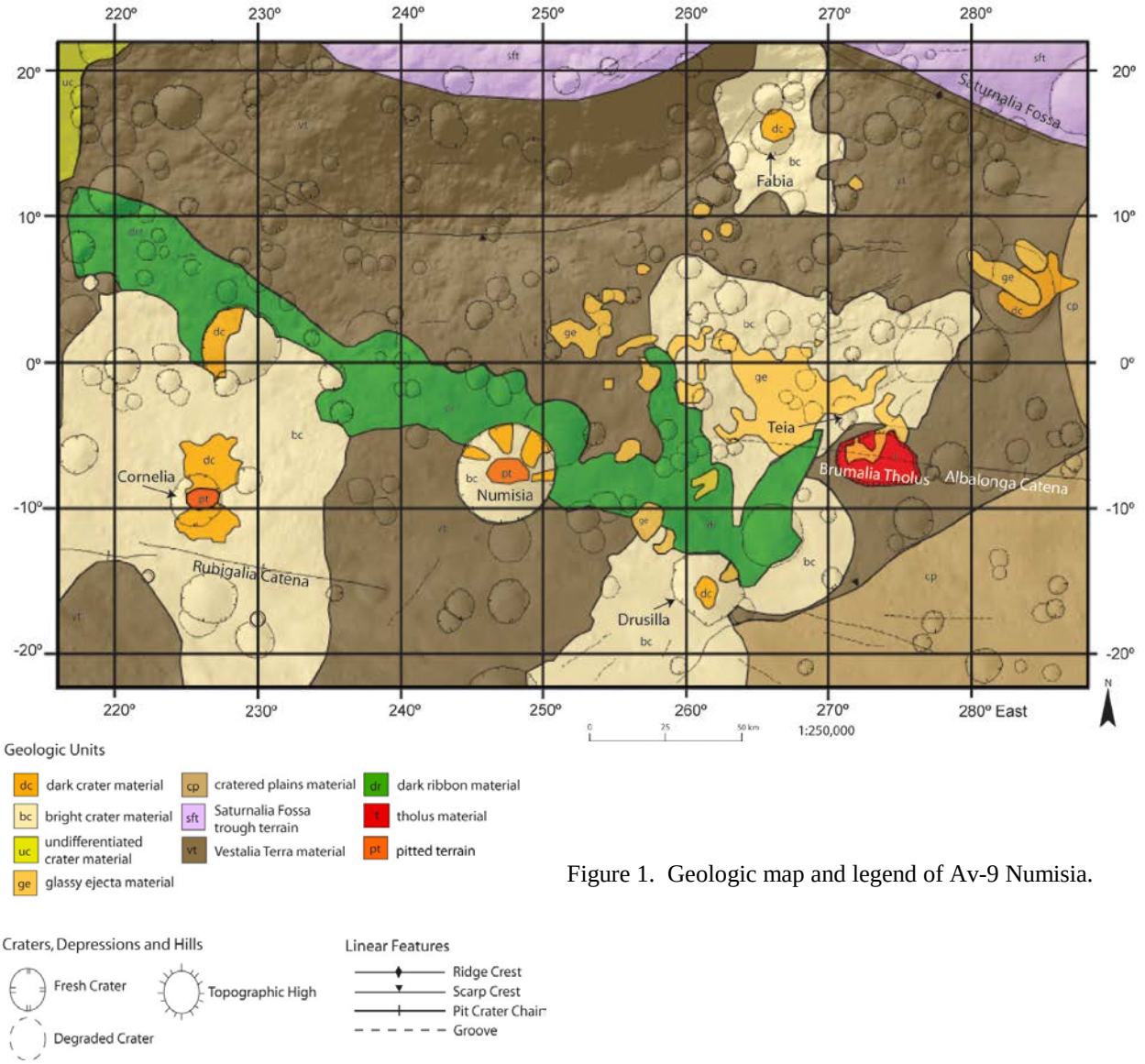

Figure 1. Geologic map and legend of Av-9 Numisia.

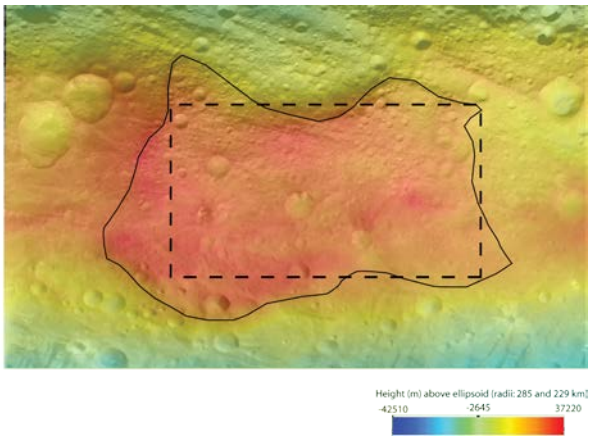

Figure 2. Global-scale topography map of Vesta centered on Vestalia Terra. Solid line marks outline of Vestalia Terra. Dashed line marks location of Av-9 quadrangle.

FINALIZATION OF THE GLOBAL GEOLOGIC MAP OF EUROPA. M. K. Bunte[1] R. Greeley[1,*], T. Doggett[1,**], P. Figueredo[1,***], K. Tanaka[2] and D. Senske[3], [1]School of Earth and Space Exploration, Arizona State University, Box 871404, Tempe, AZ 85287 (mbunte@asu.edu), [2]U.S. Geological Survey, Flagstaff, AZ, [3]Jet Propulsion Laboratory, California Institute of Technology, Pasadena, CA, (*deceased; **currently at Northern Virginia Community College; ***currently at the ExxonMobil Research Company, Houston, TX).

Introduction: Europa's extremely young surface age, evidence for extensive resurfacing, and indications of a sub-surface ocean elevate its astrobiological potential for habitable environments, making it a compelling focus for planetary geological study. Knowledge of the global distribution and timing of material units is a key step for understanding the satellite's history and for identifying features relevant for future study.

We have produced an updated 1:15M global geologic map of Jupiter's moon Europa. This contribution builds upon the global map presented by [2] and incorporates the interpretations of material units and sequences of events presented by [3-8] in local to subregional perspectives. Unified guidelines for the identification, mapping and naming of Europan geologic units were put forth by [9] and employed in regional-to-hemispheric scale mapping [10, 11] and the first global geologic map [2]. This effort provides a more complete understanding of the material surface units, their stratigraphic relationships, and the resurfacing history associated with their formation.

Methodology: A global photomosaic utilizing the best available *Galileo* and *Voyager* regional and high resolution (12.6 to 0.23 km per pixel) coverage was used as a basemap [1], following suggested methodology of stratigraphy for planetary mapping [12]. We have defined units based on characteristics which can be compared in both low and high (better than 1.7 km/px) resolution images, then extrapolated those characterists to low resolution and varied illumination areas rather than establishing "undifferentiated" units. Consideration was given to viewing geometries when determining units; [13] has shown incidence angle to control the visibility of texture. To portray stratigraphic relationships, we present the map in two parts: the first illustrates material units; the second portrays prominent linear features, which are mapped as structures at 1:15M scale, though they would otherwise be separate material units.

Material Units: Geographic regions are characterized in terms of the main surface units summarized by [9]: plains, chaos, band, ridge, and crater materials.

Plains Material. Globally extensive plains appear smooth at regional or global resolution but are intensely *ridged* at higher resolution. Plains are characterized by cross-cutting ridges and troughs at multiple scales with various geometries including arcuate, sinuous and anastomosing. Some localities are disrupted by pits and domes; however, plains are sparsely cratered. Varying degrees of texture, deformation, albedo, topographic relief, embayment and are prevalent.

Chaos Material. Disrupted terrain which forms dark albedo features in global or regional resolution and has sharp embaying contacts with brighter, smoother plains units are termed chaos. At low resolution, regions of chaos also have transitional areas of dark albedo spots in a high albedo matrix. At higher resolution, the chaos is seen to be hummocky plains with plates of younger plains units in a matrix of dark, knobby material. Variations in elevation, degree of disruption, and density of lenticulae establish the differences between *chaos*, *lenticulae*, and *plains* [14].

Band Material. Linear, curvilinear, or cycloidal zones distinguished by contrast in albedo and/or texture to surrounding terrain are termed bands. Typical bands exhibit sharp margins and an internal structure of subparallel ridges and troughs which may be subdued.

Ridge Material. Linear features which occur as single crests, central troughs bounded by a ridge pair, and complex subparallel ridges are ridges. They range in length from a few to >1000 km with widths up to several km and are convex to trapezoidal in cross-section. Ridges may exhibit tapering, flank slopes, mass wasting, dilation, sinuous margins, anastomosing and discontinuous sets, or bifurcation. Some are cycloidal. These materials are mapped as structural symbols though they correspond to a specific formation process and time. Widely spaced linear features that consistently cross-cut younger plains units and are distinct from the densely spaced ridges in plains units are used as stratigraphic markers, or *framework lineaments*.

Lenticulated Terrain. Regions where individual lenticulae have been emplaced in dense populations represent a transitional unit from *plains* to *chaos*.

Crater Material. All material comprising a crater's floor, central peak (when present), wall, raised rim, and ejecta deposits is mapped as crater material.

Stratigraphy: The paucity of impact craters on the surface of Europa prevents a determination of relative age between material units based solely on crater density frequencies. Rather, we establish stratigraphic markers as a function of linea cross-cutting relationships [15] and attempt to illustrate the surface history through four periods of formation based these linea relationships. These *framework lineaments* (Figure 1 bottom) indicate the most important stratigraphic

markers for formation periods and represent a simplification of stratigraphy while preserving overall geologic units and major structural features (Figure 1 top).

The earliest preserved material units on Europa are dominated by the intricate *ridged plains* materials, typified by Balgatan and Falga Regio where bright plains are crisscrossed by ridges. The second period of formation is typified by the emplacement of many prominent linea and the *bands* or "wedges" of Argadnel Regio. The Tyre and Callanish impacts occurred during this period. The third period of formation is typified by broad regions of chaos as seen in Dyfed and Powys Regio and widespread emplacement of *lenticulae*. The youngest materials on Europa include *lineaments*, *chaos*, and the prominent *crater* Pwyll.

Formation Processes: Full understanding of the formation and evolution of each material unit and structural group requires reflection on globally consistent origins for each feature or an interpretation of potential local conditions or controls not excluded by a global process as all units and structures are represented globally. We have undertaken a comparison of all previously proposed formation mechanisms to attempt to establish the most likely scenarios of unit formation and evolution. To augment the basic description and interpretation of geologic units and features and to aid in our understanding of formation mechanisms so that we may appraise each model for its merit, we are examining the Galileo NIMS data to assess correlations between composition and geology or topography as in [16]. In addition, we are reviewing all photoclinometry and stereo imaging results from [17].

Acknowledgements: We acknowledge the contributions to this mapping effort by E. Kolb, K. Mullins, and S. Weiser. We also acknowledge T. Hare and C. Bradbury for technological support, J. Blue for help in establishing nomenclature, and D. Ball of the Ronald Greeley center for Planetary Studies for image processing assistance. This work was supported by NASA through the Planetary Geology and Geophysics Program and the Outer Planets Research Program. Additional funding to make this work possible is provided by a NASA Earth and Space Science Fellowship.

References: [1] USGS, I-2757, 2002; [2] Doggett et al., in *Europa:* 727, 2009; [3] Lucchitta and Soderblom, in *The Satellites of Jupiter*: 521, 1982; [4] Senske et al., *LPSC* XXIX, #1743, 1998; [5] Prockter et al., *JGR., 104*:16531-16540, 1999; [6] Kadel et al., *JGR*, 105, 22657-22669, 2000; [7] Figueredo et al., *JGR*, 107, 10.1029/2001JE001591, 2002; [8] Kattenhorn, *Icarus*, 157, 490-506, 2002; [9] Greeley et al., *JGR*, 105, 22559, 2000; [10] Figueredo and Greeley, *JGR*, 22629-22646, 2000; [11] Figueredo and Greeley, *Icarus*, 167, 287-312, 2004; [12] Skinner and Tanaka, *LPSC XXXIV*, #2100, 2003; [13] Neish et al., *Icarus* 221, 72-79; [14] Collins and Nimmo, in *Europa*: 259, 2009; [15] Doggett et al., *LPSC* XXXVIII, #2296, 2007; [16] Shirley et al., *Icarus*, 210, 358-384, 2010; [17] Schenk, *Atlas of the Galilean Satellites*, 406, 2010.

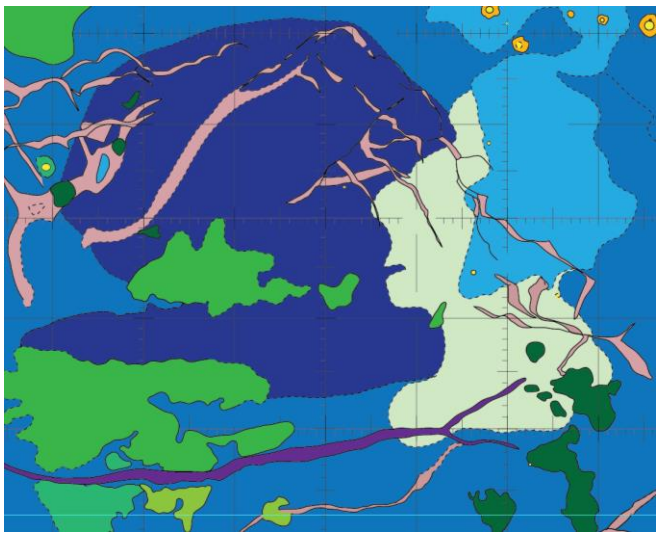

Fig. 1. Excerpt from Europa map illustrating material units near Argadnel Regio (top; see bounding box on map below) and 100 *framework lineaments* that establish a stratigraphic framework (bottom).

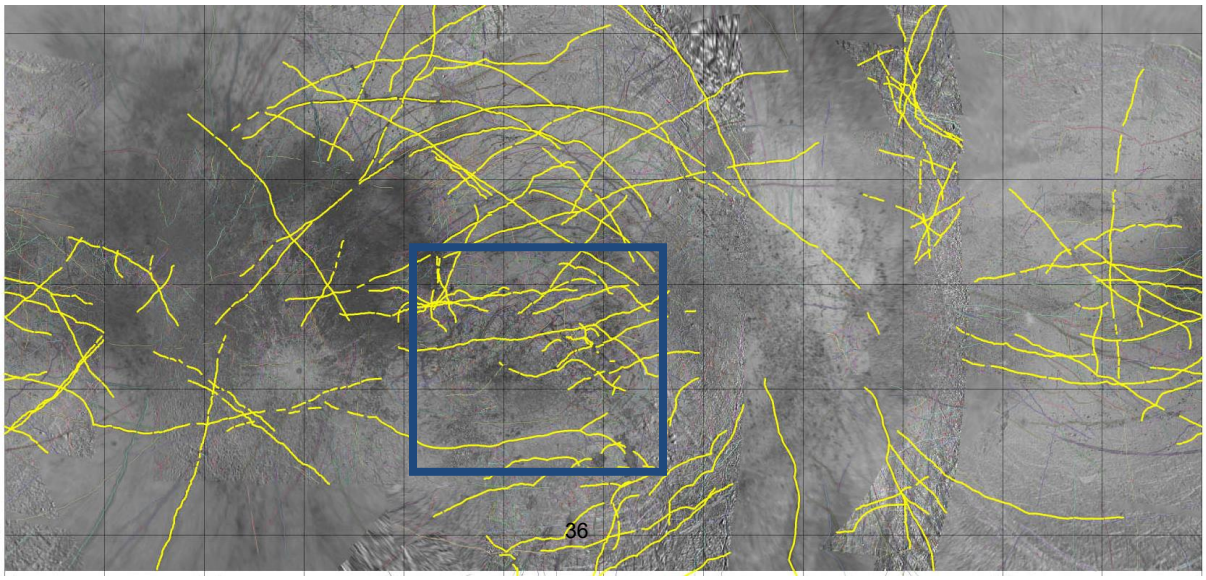

NORTHWEST NILI FOSSAE: A POSSIBLE ANCIENT HOT SPRINGS AREA. T. Colborg [1], Z. Kaiser[1], C. Konen[1], J. Lackner[1], J. Begin[1], G. Feeny[1], K. Kalina[1], V. Carrion[1], K. Gabriel[2], C. Walsh[2], H. Brennan[2], B. Good[2], M. Licari[2], T. Lombardi[2], R. Green[2], G. Teftsis[2], K. Vanderbilt[2], R. Kyles[2], S. Easterday[2] and A. Henderson[2],[1]The Grosse Pointe Mars Research Team, [2]The Grosse Pointe North Astronomy class (North HS, 707 Vernier Rd, Grosse Pointe Woods, MI 48236)

Introduction: Our research team searched for possible hot springs on Mars that could have once hosted ancient life. Sulfur rich hot springs found on Earth are teeming with life. They would be an ideal place to look for life forms on Mars. [1] Hot springs have been tentatively identified in Vernal Crater, and a volcanic cone in the Nili Patera caldera on Mars has been identified to contain potential hydrothermal mineral deposits. [2]

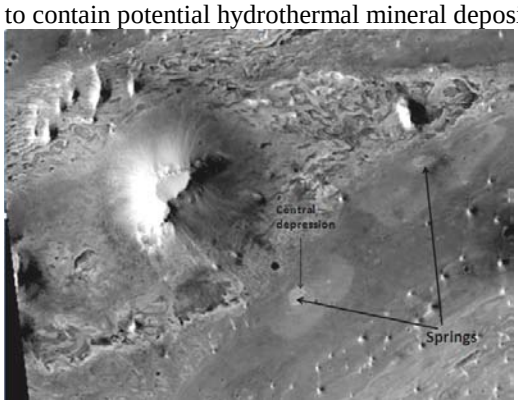

Figure 1 HiRISE image PSP_002812_1855 with potential hot springs.

Procedure: We started by examining 132 HiRISE hydrothermal images. We also used geological maps to examine the sites. We focused on northwest Nili Fossae because it had evidence of desiccation cracks, methane releases, mounds, oxidized iron minerals, phyllosilicates, and Noachian-aged rocks.

We studied features on an IRB non-map projected version of HiRISE image PSP_008637_2035 using the HiView program. We constructed 3-D and profile maps from MOLA to get geospatial relationships. We then used JMARS to do mineralogical, thermal, and dust analysis. We used CRISM stamps and the JCAT tool, with reference spectra from USGS and ASTER spectral libraries, to determine the specific rocks and minerals at our site. We looked for phyllosilicates, hydrated silicates, sulfates, and carbonates.

We looked specifically for minerals with Al, Mg, Ca, and Fe cations. We believed that these cations would be the most abundant because of preliminary CRISM stamp analysis, and the presence of aluminum in the sulfates previously found on Mars. As on Earth, life could have been associated with these martian hot water sulfates. [3]

Phyllosilicates form in a prolonged wet and often warm environment. [4] Clays are great at holding and preserving organic matter. [5] With phyllosilicates in our area, there is a chance that we could find the chemistry of life. [6]. Phyllosilicates have been found in Nili Fossae, but most publications seem to focus on areas east of it or in the main depression. [7] Phyllosilicates have been found concentrated on the slopes of mesas and along canyon walls, which shows that water played a sizable role in changing the minerals in a variety of terrains. [6] Iron oxides have been altered by water and are typically found in places where there are hot springs. [8] Sulfate minerals form in a relatively acidic environment. A common environment involves contact with hot water solutions. [9] Hydrated silicates can be dissolved by hot water and transported via hydrothermal vents into hot springs. [10] Some hydrated silicates such as opal have been found on Mars in deposits that are younger than Noachian-aged rocks, implying that hot springs may have been active in more recent times. [11] We also looked for carbonates, since the ones previously found in Nili Fossae are like the Pilbara carbonates that are in Australia which contain stromatolites. [12] Carbonates had been a missing rock type on Mars and are not very common there. [13] Carbonates can form from buried and decomposed organisms. [14]

Sample data: HiRISE imagery shows a light blue area near the base of a cliff (Fig. 2)- its diameter is 247 meters. It closely resembles the Vernal crater mounds that are suspected hot springs. There, the elliptical features are 200 meters wide and up to 600 meters in length. [15]

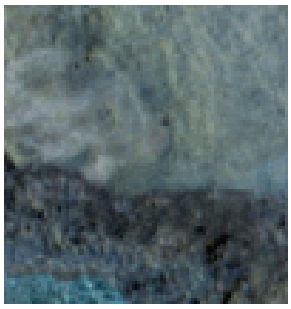

Figure 2 HiRISE image PSP_008637_2035 showing a possible martian hot spring mound.

The structure in Figure 3 appears to be a mound eroding with different sedimentary layers being exposed. It has a diameter of 453 meters. This is consistent with other images in Nili Fossae showing layered bedrocks. [16] Hydrothermal mounds on Earth show

similar layering, supporting the hypothesis that this martian mound formed in a hot spring.

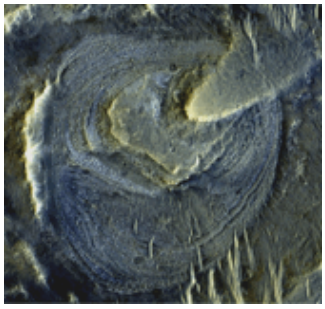

Figure 3 HiRISE image PSP_008637_2035 shows an eroding mound with sedimentary layers exposed.

Figure 4 shows a channel with high lands on either side. We chose four points (A, B, C and D) on the image to get a range of spectra (Fig. 5) A and B are on the cliffs above the channel. C and D are on the bottom of the channel. Phyllosilicates were detected at all locations, making it a potential hydrothermal site.

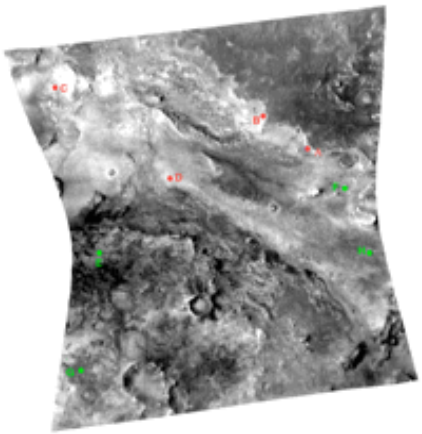

Figure 4. CRISM image FRT0000D6D6. Locations where spectra in figure 4 were sampled are labeled A, B, C and D.

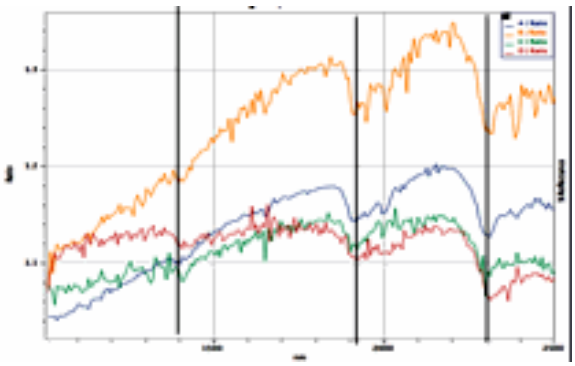

Figure 5. JCAT spectra from NW Nili Fossae. The orange line corresponds to site B in Figure 4, blue line to site A, green line to site C, and red line to site D.

Conclusions: We conclude that northwest Nili Fossae was a hot spring (hydrothermal area) based on these criteria: 1) Observed mounds range in diameter from 3 meters to 453 meters, making them a suitable size to be considered as hot springs or stromatolite reefs.

2) The phyllosilicates saponite, nontronite, chlorite, glauconite, biotite and phlogopite were detected. They seem to be eroding out from a layer of rocks along the cliffs and filling the bottoms of low channel areas. This layer is not associated with the youngest surface, so it may agree with Noachian aged rocks. The phyllosilicates do not seem to be from impact ejecta because they are all in a uniform layer.

3) The presence of large quantities of water is supported with the detection of desiccation cracks. 4) We did not detect any kaolinite, sulfates or hydrated silicates, which suggests these waters were not acidic in pH, but more neutral. This implies the environment of Mars at the time of their formation was wetter and at temperatures more hospitable to life. [2, 17, 18]

We also conclude northwest Nili Fossae has not undergone serpentinisation, because there was no spectral detection of olivine, magnetite, serpentine, or talc. Therefore methane could not have formed through serpentinisation on our site, leaving the possibility open that it is of biological origin.

Magnesite and dolomite were detected. Since carbonates were found, there is a very slim possibility that they may be associated with a biological origin. However, carbonates can form as a result of geological processes as well. [19]

References: [1] Allen,C.C. & Oehler,D.Z. (2009, February 21). *Science Daily*. [2] Webster,G. et al. (2010) *JPL News*, 361. [15] Thompson,A. (2009) *Space.com*, Article 4910. [16] Cowling, K. (2012. May 21) *Spaceref.com*. [3] Fan, C. et al. (2006) *LPI Workshop on Matian. Sulfates*, pdf 7033. [4] Mangold,N. et al. (2008) *LPI Workshop on Martian Phyllosilicates*, pdf 7024. [5] Des Marias, D. (n.d.) *MSL 4th workshop* , Talk 9 [6] Herkenhoff,K. (2012) *HiRISE LPL*, ESP_026992_2025. [7] Ehlmann,B.L. et al. (2008) *LPI Workshop on Martian Phyllosilicates*, pdf 7019 [8] Ralph,J. & Chau, I. (n.d.) *Mindat* , topic 1896. [9] "Sulfate Mineral" (n.d.) *Encyclopedia Britannica*, topic 572471. [10] Ehlmann, B.L. (2012) *LPI Meeting on Early Mars*, pdf 7084. [11] Milliken,R.E, et al. (2010) *Geology*, 36(11), 847-850. [12] Gill, V. (2010*) BBC News*, Article 10790648. [13] Amos, J. (2008) *BBC News*, Article 7791060 [14] Ehlmann, B.L. (2009) *JGR, 114*(E). [17] Bishop, J.L. (2008) *LPI Workshop on Martian Phyllosilicates*, pdf 7038. [18] Smith, M. R. et al. (2010) . *41st Lunar and Plan. Sci. Conf, 4, pdf 2194.* [19]Deelmann, J.C. (2010) *Low Temp. Form. of Dolomite. & Magnesite*, vers. 2.3.

Methane Gas Plumes as Indications of Subsurface Aquifers in Nili Fossae.

Wu, Simin, Girton, Ally, Hinkle, Annalise, Arnold, Lauren, Johnson, Barrett.
Kickapoo High School. 3710 South Jefferson Avenue, Springfield, MO 65807.

High-concentration atmospheric methane plumes are currently being detected on the Martian surface. Multiple hypotheses have been proposed to explain possible sources of these methane plumes. Thirty high resolution images and spectral analyses obtained from CRISM, HIRISE, and THEMIS of the Nili Fossae region were analyzed in an attempt to identify a possible source of origin. Morphological analysis indicates extensive megabreccia formations, faulting, horst and graben systems, and volcanic landforms and structures. Additionally, high concentrations of Fe/Mg olivine as well as elevated bound water deposits were also found in association with previously identified serpentine and serpentinite deposits in this region.

It is believed that these results are consistent with the methane gas plumes originating by abiogenic processes. We propose that these plumes result from the exothermic process of serpentinization of high Fe/Mg olivine melting subsurface ice deposits releasing stored methane gas deposits. Correlations between the methane gas plumes, abundant Fe/Mg-olivine deposits, significant bound water deposits, and morphological environments conducive to serpentinization are indications that these plumes being a result of this process. Ongoing methane gas releases are a result of the serpentinization processes due to the interactions of olivine with the atmospheric carbon dioxide and an extensive subsurface aquifer in the Nili Fossae region.

COMBINING COMPOSITIONAL AND MORPHOLOGIC DATA TO MAP THE COPERNICUS LUNAR QUADRANGLE. J. J. Hagerty[1], J. A. Skinner[1], L. R. Gaddis[1], C. M. Fortezzo[1], and T. D. Glotch[2], [1]USGS Astrogeology Science Center, 2255 N. Gemini Drive, Flagstaff, AZ 86001, [2]Stony Brook University, Stony Brook, NY, email: jhagerty@usgs.gov.

Introduction: The recent flood of lunar data has provided unprecedented views of the lunar surface, which in turn has shown us that portions of the lunar surface, such as the Copernicus lunar quadrangle, contain numerous lunar lithologies with several possible origins [e.g., 1 – 10]. However, with increasingly abundant and complex data comes increasingly varied models for lunar surface processes. In fact, interpretations of the origin of specific units or features can vary depending on the data being used. In an effort to provide a comprehensive understanding of the evolution of the lunar crust within the Copernicus quadrangle (Fig. 1), we are integrating multiple data sets via end-member methodologies.

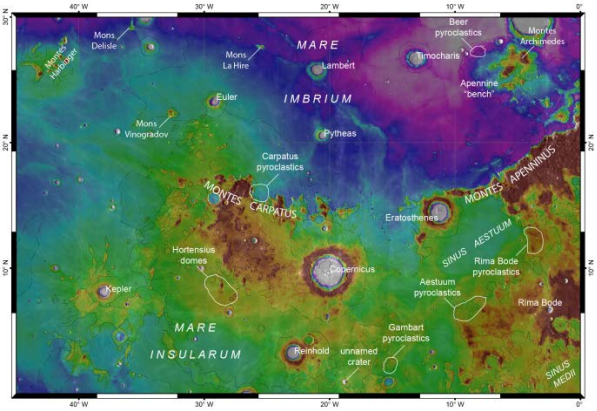

Figure 1. The base image is a color-coded version of the LRO LOLA topographic map (100 m/pixel). Also shown are features with major compositional variations that will serve as key locations to investigate.

Traditionally, two investigative strategies have been employed to determine the distribution and origin of specific geologic features and lithologies on the Moon: geologic/morphologic mapping and compositional mapping. Rarely, however, have the two methods been seamlessly integrated for lunar science investigations with the specific intent of producing a USGS geologic map. The abundance of high-resolution lunar data, in combination with the integration of the two end-member mapping methodologies, has the potential to provide significant new constraints on the formation and evolution of the lunar crust, to establish a comprehensive geologic and stratigraphic context wherein subsequent studies can be conducted, and to delineate refined approaches for the systematic production of geologic maps of the Moon.

This mapping project addresses several major lunar science issues including: 1) examination of the heterogeneity of lunar crustal materials and their vertical and horizontal distribution, 2) spatial and temporal variation of lunar lithologies, 3) refinements of the geologic and stratigraphic architecture of referent lunar materials, and 4) efficiency assessments of lunar mapping methods, including the role of data set type and resolution within the 1:2.5M scale quad-based mapping scheme. New constraints on the composition and structure of the lunar crust will follow which will improve estimates of the bulk composition of the Moon and allow new tests of models for the origin and evolution of the Moon.

Results from Pilot Study: PG&G funded a pilot investigation program in 2003 (PI L. Gaddis, USGS) wherein the chief objectives were to research the map-based needs of the lunar science community, to establish a systematic mapping program, to help define the technical requirements of a rejuvenated program, and to promote such a program in advance of recent lunar missions. The pilot mapping project examined the discrete geologic materials within the Copernicus quad and the methods by which the materials could be identified and described. Results, as detailed in Skinner and Gaddis [11], include:

- Validation of the 1:2.5M map scale for systematic mapping based on the resolution of continuous basemaps and the digital mapping environments where they are analyzed;
- Subdivision of crater materials into facies, based on combined morphology and spectral signature;
- Retention of facies indicators in unit name but abandonment of ruled patterns indicative of unit-specific albedo;
- Retention of surface brightness stipples using a threshold determined by Clementine data;
- Improvement of criteria for delineating volcanic vent materials, including domes and dark-halo craters;
- Abandonment of (where not critical) the widespread use of concealed contacts;
- Retention of cross-sections to demonstrate vertical and lateral relationships of stratigraphic horizons (currently, cross-sections are not common components of planetary geologic maps);
- Application of a 5 km lower limit of the functional delineation of unit outcrops;

- Application of discrete units and stipples to resolvable, unit-specific impact ejecta (e.g., excavated and redistributed mare material);
- Retention of detailed geologic unit explanations (correlation of map units), with appropriate variations to account for the inclusion of discrete, superposition, time-transgressive, and unconformable units.

While the pilot study provided needed refinements to geologic mapping methodology, much work remains for the Copernicus quad, including detailed unit delineation and analysis. Our current efforts will expand upon the previous work to provide a methodical examination of a lunar quadrangle that is critical to the reinvigorated effort to map the Moon.

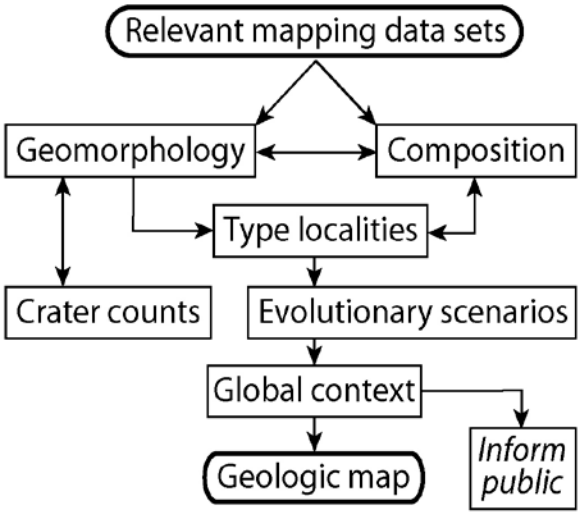

Figure 2. Conceptual flow chart for our two-pronged mapping effort.

Current Mapping Effort: As noted above, we are using a two-pronged mapping approach that hinges on buttressing the well-vetted and "classical" methodologies of morphologic mapping with compositional mapping. The integration of end-member approaches, in combination with robust lunar data, will result in a powerful tool for understanding the formation and evolution of the lunar crust in the quad. Figure 2 demonstrates a conceptual flow chart for how the proposed integration effort will proceed. Compositional data sets will rely on both regional- and local-scale spectral and elemental data sets. Note the circular iterations of geomorphology ⇨ type-locality ⇔ composition. Geomorphology will provide the geologic context for compositional assessments. Crater counts will supplement morphologic studies for assessment of relative unit age and stratigraphy.

Compositional Mapping: Individual data sets (e.g., Diviner, Clementine, and M^3 spectral data) are being used to identify and assess lithologic diversity but are also being combined with lunar sample data to conduct forward modeling of low-resolution thorium (Th) and iron (Fe) data from the Lunar Prospector Gamma Ray Spectrometer (LP-GRS). Combining these compositional data sets can be difficult due to the fact that each has a different spectral resolution and each provides unique information. However, by combining these data sets it will be possible to accurately determine the compositions of individual features in the quadrangle.

Determining the compositions of features in the quad is critical for evaluating their importance to lunar science. For instance, the pyroclastic deposits are important because they provide a window into lunar mantle, while the Th-rich impact ejecta provide windows into the structure and composition of lower crust. Meanwhile, Th-rich volcanics (basaltic but also possibly silicic) provide information about crustal formation processes and the bulk composition of the crust [e.g., 4, 5]. Lastly there are several anomalous regions within the quad that do not have clear origins and have not been previously explored. These features, which will be investigated in detail for the first time, may provide new information about lunar crustal processes.

Year 1 Goals and Progress: Funding for the project was allocated to the USGS at the beginning of Fiscal Year 2013 and a subcontract was established with Co-I Glotch (Stony Brook University). Co-Is Glotch and Gaddis have begun generating mosaics of Diviner and Kaguya data respectively. Co-I Skinner has begun pulling together the project-specific GIS. The bulk of the remaining work (i.e., regional scale geologic and compositional mapping will be accomplished in the 3rd and 4th quarter of the fiscal year).

Acknowledgements: This work is supported by NASA through the Planetary Geology and Geophysics program via grant NNH12AU82I.

References: [1] Cahill et al. (2009) *J. Geophys. Res., 114*, E09001; [2] Chevrel et al. (2009) *Icarus, 199*, 9; [3] Glotch et al. (2010), *Science, 329*, 1510; [4] Hagerty et al., (2006) *J. Geophys. Res., 111*, E06002; [5] Hagerty et al., (2009) *J. Geophys. Res., 114*, E04002; [6] Lawrence et al. (2007) *Geophys. Res. Lett., 34*, doi: 10.1029/2006GL028530; [7] Matsunaga et al., (2008) *Geophys. Res. Lett., 35*, L23201; [8] Spudis, P. and Taylor, G.J. (2009) *Lunar. Planet. Sci. Conf., 40*, abstract #1039; [9] Woehler et al. (2011) *Planet. Space Sci., 59*, 92; [10] Yamamoto et al. (2010), *Nat. Geosci., 384*, doi:10.1038/NGEO897; [11] Skinner, J. and Gaddis, L. (2008) *GSA, 40*, 518.

SOUTHERN TELLUS REGIO, VENUS: GEOLOGIC AND STRUCTURAL MAPPING AND IMPLICATIONS FOR VENUS CRUSTAL PLATEAU FORMATION HYPOTHESES. M. Graupner Bergmann and V. L. Hansen, Department of Geological Sciences, University of Minnesota, 1114 Kirby Drive, Duluth MN, 55812, USA, graup044@d.umn.edu

Introduction: Crustal plateaus are quasi-circular, flat-topped plateaus with heights ranging 1-4 km. These crustal plateaus are host to distinctive tectonic terrain, referred to as ribbon tessera terrain. Crustal plateau formation on Venus is subject to animated debate, centered on plateau support and resulting surface deformation. Four formation hypotheses exist, mantle downwelling [1-3], mantle upwelling [4-8], pulsating continents [9] and the lava pond hypothesis [10]. Detailed mapping of southern Tellus Regio provides critical clues for plateau evolution. Tellus Regio is one of two isolated crustal plateaus on Venus. Tellus Regio, centered at 42.6N/76.8E, is nearly oval with a slightly smaller and tapered southern part, has a long axis dimension of ~2300 km, is bordered by lowlands, and sits ~2-3 km above the regional plains with the highest elevations in the eastern, western, southern portions, and steep eastern and western margins and gently sloping northern and southern margins [11, 12]. The northern margin of Tellus Regio is not well defined and may represent a transitional area with the lowlands. North-central Tellus is host to a low-lying interior showing complex surface deformation. High resolution SAR data reveals an overall rough surface topography on Tellus Regio marked by ribbon tessera terrain. Structural and geologic mapping of southern Tellus Regio (43N/73-90E, 26N/74-86E) provides an excellent opportunity to examine the rich surface deformation history, preserved during crustal plateau formation, enabling the evaluation of crustal plateaus hypothesis.

Regional Geologic Relations: Geologic and structural mapping revealed that tessera terrain includes various combinations of long-, intermediate-, and short-wavelength (λ) folds, intra-tessera basins, ribbon structures, graben complexes, fault scarps, and undefined lineaments. Long- λ folds (20 km to >150 km) dominate the plateau generally occurring along the margins of Tellus Regio, although a few long, NW-trending wavelength folds occur in the center of the plateau. Intratessera basins are broadly distributed across the plateau, and occur at a range of sizes, shapes and orientations. Large intratessera basins are widely distributed across the plateau and commonly represent fill of long-λ fold troughs. Intermediate-λ folds (5 - 15 km) occur across the plateau defining a general fluid pattern [13]. Relatively broad elongate embayments also form in the troughs of intermediate-λ folds. Along the limbs and crests of long-and intermediate-λfolds short, narrow basins occur within the troughs of short-λ folds (λ<1 km) and ribbon structures. Ribbon structures occur across the plateau, whereas graben complexes generally appear in suites throughout the central and western regions of southern Tellus Regio. The regional distribution and orientation of structural elements collectively define a fluid-like pattern across the southern Tellus map area. Detailed analysis of targeted regions provides detailed temporal constraints.

Detail Map areas: Six detail map areas contribute to provide a detailed geologic history of the crustal plateau. Each area was selected for characteristic structural elements and was mapped using full-resolution Magellan cycle-1 and -2 SAR data, in normal and inverted modes, and combined for true stereo views [14]. Generally short- and intermediate-λ folds, ribbon structures and basin fill material occur throughout each of the detailed map areas. Fewer long-λ folds, graben and fault scraps occur throughout the areas. Broadly, all detail map areas record generally parallel short-, intermediate and long-λ folds, and ribbon structures that trend orthogonal to fold axes. Troughs of short-, intermediate-, long-λ folds and ribbons are commonly filled with flood deposit material. Although short-λ folds were previously associated with local intratessera basins within Tellus Regio [15, 16], the extent and abundance of short-λ folds across Tellus has not been previously documented. Each of the detail map areas record similar geometric structural relations, and relative timing of strucutractral elements, yet each region highlights different structural orientations and 2D bulk strain. The geologic mapping results are broadly in accord with previous studies on portions of Tellus Regio [15-18].

Broadly, fold λs show a progression from short-, to intermediate-, and long-λ over time, ribbon structures occur early, shortly after short-λ folds. Graben and fault scarp formation occurs late. Deposition of flood material occurred throughout the progressive deformation filling the troughs of all types of structural elements.

Structural wavelengths recorded for contractional and extensional structures for the detail map areas place estimates on layer thickness operative during structural-element formation; empirical λ:layer thickness ratios of 3 to 6 for contractional structures and 4 to 2 for extensional structures constrain the layer thickness estimates [10, 19-20]. Average layer thicknesses for short-λ folds and extensional ribbons structures show broadly overlapping average layer thicknesses,

ranging from range from 0.1 to 1.15 km, and 0.76 to 1.33 km, respectively. Average layer thickness estimates associated with intermediate-λ fold formation range from 1.0 to 2.15 km and 1.45 to 3.83 km, depending on location; whereas long-λ folds deformed layers ranging in thickness from ~5 to 15 km. All six areas record similar increases in layer thickness over time, as well as overlapping thickness estimate between short-λ folds and ribbon structures. The progression of structures based on layer thickness estimates is consistent with the broad structural temporal relationships interpreted across the entire plateau with short-λ structures forming early and long-λ structures forming later. An increasing layer thickness over time also places a strict requirement on the evolution of the rheological structure across the plateau [10]; the presence of a thin initial layer, with an increase of layer thickness over time, requires a sharp viscosity gradient with depth in order to form short-wavelength fold and ribbon structures.

Histories and Implications: A general evolution arises from the geologic histories interpreted from each map area. Short-λ folds formed early followed or accompanied with, ribbon structure formation, deforming a thin (0.1-1.3 km) layer with a sharp viscosity change at depth. Low-viscosity flood material locally flooded structural lows. Fold formation and local flooding resulted in an increase in layer thickness. These early formed structures and their respective basin fill, were uplifted during the formation of intermediate-λ folds. Troughs, limbs and crests of intermediate-λ folds preserve these previously formed structures. Intermediate-λ fold troughs were then filled by more flood material, resulting in further layer thickening. During formation of long-λ folds the previously deformed terrain was again uplifted (and down warped), the troughs of which were locally filled by flood material, locally experiencing major flooding. During the latest stage of surface evolution graben complexes, and similar trending fault scarps, cut all other structures, with late local flooding in the troughs of some graben complexes.

The temporal relations and spatial orientations of structures provide equally valuable information about the evolution of the surface, and possible mechanisms. The interpretation of the 2D bulk strain ellipses provide clues to how 2D bulk strain changed over time. During "thin-layer-time" all six map areas record different orientations of local 2D bulk strain, consistent with the interpretation that the early surface deformation recorded a high structural fluidity at a regional scale. As the structural wavelengths increased with time, the fluidity of the surface deformation decreased, and the area deformed in a more coherent manner. Overall the orientations, spatial relations and temporal relationships of structural elements over the entire southern Tellus Regio map area depict: 1) layer thickness increased over time, allowing for short-wavelengths and ribbons to form early and then progressively increase wavelengths; 2) deformation and flooding occurred broadly synchronously, locally preserving early-formed structures and thickening the layer over time; and 3) 2D bulk surface strain changed over time, recording an early regional-scale variations that record a sort of surface fluidity, which evolved to a regionally consistent pattern, reflecting a change in regional strength and coherence across the southern Tellus Regio. This sequence of events calls for a high geothermal gradient over the entire region that decreased over time. Even though the overall geothermal gradient decreased over time, it has to be initially high enough to allow for a sharp viscosity gradient beneath the initial thin layer, and to remain hot enough to allow low-viscosity material to fill structural lows [10, 21-22]. In addition, a high geothermal gradient would provide the surface with enough ductility to deform in a fluid-like manner across the regional map area, as evident in early 2D bulk strain ellipses. This fluidity in structural elements ceased as the geothermal gradient decreased and the layer thickness increased with time.

Evaluations of crustal plateau formation hypothesis: The pulsating continents, mantle downwelling and mantle upwelling formation hypotheses are somewhat difficult to reconcile with the geologic evolution documented herein and the implications for southern Tellus Regio. On the contrary, the lava pond hypothesis and, by the association the bolide impact hypothesis, depicts an environment that creates similar surface deformation and evolution as documented for southern Tellus Regio.

References: [1] Bindschadler D.L. & Parmentier M.E. (1990) JGR, 95, 21329-21344. [2] Bindschadler D.L. (1995) Rev. Geophys., 33, 459-467. [3] Bindschadler D.L. et al. (1992) JGR, 97, 13563-13577. [4] Herrick R.R. & Phillips R.J. (1992) JGR, 97, E16017. [5] Phillips R.J. & Hansen V.L. (1998) Science, 279, 1492-1497. [6] Hansen V.L. & Willis J.J. (1998) Icarus, 132, 321-343. [7] Ghent, R.R. & Hansen V.L. (1999) Icarus, 139, 116-136. [8] Hansen V.L. et al. (1999) Geol., 27, 1071-1074. [9] Romeo I. & Turcotte D.L. (2008) EPSL, 276, 85-97. [10] Hansen, V.L. (2006) JGR, 111, E10110. [11] Bindschadler D.L. & Tatsamura M.J. (1992) LPS XXII, 103-104. [12] Senske D. A. (2010) LPSC XLI, #1256. [13] Graupner M. (2011) GSA #191691. [14] Plaut J.J. (1993) Guide to Magellan Image Interp, 33-45. [15] Banks B.K. (2000) Masters Thesis, Southern Methodist Univeristy. [16] Banks B.K. & Hansen V.L. (2000) JGR, 105, 17655-17667. [17] Gilmore M.S. et al. (2010) LPSC XL, #2015. [18] Gilmore M.S. et al. (2011) LPSC XLI, #2053. [19] Huddleston P. & Lan L. (1995) P. Appl. Geophys., 145, 607-620. [20] Ghent R.R. & Tibulaec I.M. (2002) GRL, 29, 1 1-4. [21] Ghent R.R. et. al. (2005) JGR, 110, E11006. [22] Ruiz J. (2007) Science, 55, 2063-2070.

GEOLOGIC MAPPING OF THE NIOBE AND APHRODITE 1:10M MAP AREAS, VENUS: UPDATE 2013, INSIGHTS & IMPLICATIONS V. L. Hansen[1] and I. López[2], [1]University of Minnesota Duluth, Duluth, MN 55812 (vhansen@d.umn.edu), [2]Departamento de Biología y Geología. Universidad Rey Juan Carlos. 28933. Mostoles. Madrid (ivan.lopez@urjc.es).

Introduction: We are conducting a detailed and comprehensive geologic, structural, and volcanic synthesis of Niobe Planitia (0-57°N/60-180°E, *I-2467*), Aphrodite (0-57°S/60-180°E, *I-2476*), and the immediate surroundings, herein referred to as Niobe Map Area and Aphrodite Map Area, respectively, and Niobe-Aphrodite (NA), collectively. Geologic analysis uses NASA Magellan S-band synthetic aperture radar (SAR), altimetry data, gravity, and emissivity data [1].

Geologic mapping is compiled at 1:10 M-scale, although results are informed, at least locally, by full-resolution SAR data. To date we have focused mapping efforts on the delineation of suites of structural elements, as opposed to identifying geologic units [e.g. 2]. The emerging structural patterns provide a critical basis for identification of geologic units and tectonostratigraphic packages [e.g. 3]. We present the results to date of Niobe and Aphrodite map areas together given that regional-scale patterns of structures emerge across this broad region of Venus. We employ trajectories of structural element patterns to guide the audience toward visualization of coherent patterns across the entire NA. We summarize some first-order preliminary results as they from on-going regional and detailed geologic mapping; results are divisible into two major groups: 1) insights, and 2) implications.

Insights for geologic mapping methodology: A critical first step in mapping is delineation of the distribution and trends of different structural elements or suites of structural elements, particularly in lowland regions. For example, we recognize different suites of wrinkle ridges from the most regional extensive suite concentric to Artemis, defining a region >13,000 km in diameter [4], to suites concentric to individual coronae, to changes in wrinkle ridge trends spatially associated with deformation belts. Wrinkle ridge patterns can also be used to highlight or identify provinces of varying mechanical anisotropy, as well as to record the relative temporal evolution of regional-scale features, such as deformation belts, and regional strain field associated with spatially remote features, such as Artemis.

The regional distribution of suites of lineaments can be used to infer the nature of surface burial, including minimum spatial extent and thickness of cover material. The nature of lineament suites (including lineament character, spacing, length, etc.) can also provide clues about the mechanical nature of deformed cover material, even if the nature of material emplacement processes are elusive. Mapping of detailed structural elements may enable one to differentiate different mechanical units, which may or may not, in turn, correspond to geologic units.

Examples of structural reactivation are common, and occur across a range of scales, highlighting the important role that data resolution plays in both geologic mapping and geohistory interpretation.

In several regions across Niobe-Aphrodite there appears to be structural facies transition between suites of lineaments, including: fractures, graven, pit chains, and channels. Together these suites of structural elements may defined coherent patterns across regional scales that provide clues about magmatic processes, and might place limits on the subsurface patterns of magmatic sources, and as such provide clues to magmatic processes.

Implications for geologic relations and evolution: Detailed geologic mapping over regional scales leads to a host of emerging first-order observations and/or implications for geological relations and general evolutionary trends. Two major concepts emerge from our mapping. 1) The structural tectonic elements preserved on the Venus surface record both incredible details at the local level, and yet numerous tectonic suites extend over incredibly large regions—areas that would exceed the scale of continents on Earth. The scale of both individual elements and suites of structures is truly remarkable. 2) Venus records an incredibly rich surface history across the NA map area, and by extrapolation, presumably across its entire surface imaged by Magellan SAR. This recorded surface history likely greatly exceeds the nominal ~300-500 m.y. typically ascribed to being recorded on Venus.

Detailed mapping of lowland ribbon tessera terrain, Venus's locally oldest recognize surface terrain [5] reveals that RTT preserves (1) widespread coherence in structural trends between kipukas preserved over extensive regions, and, seemingly contradictory, (2) regions marked by relatively sharp, spatially localized, changes in structural fabric orientation. Similar patterns emerge from detailed structural mapping of RTT structural fabrics within, and along the margins of, crustal plateaus [e.g. 6, A. Slonecker unpubl. map].

Detailed mapping of RTT structural fabrics also reveals that more than one episode of ribbon structure formation may have occurred within some spatial locations, with relatively late formed suites of periodic

ribbon-like ridges and troughs displaying extremely length:width aspect ratios.

A possible cousin of RTT, lineated terrain (LT), marked by extremely penetratively-developed parallel-lineaments, is commonly (but not in all cases) spatially associated with lowland RTT. Unit LT (in some cases corresponds to densely lineated plains [5]), is defined as a terrain, rather than a material unit, given that it is defined by structural elements, which clearly formed after the material unit(s) fabric deformed [1]. Where unit LT occurs adjacent to RTT, the lineament fabric typically parallels one linear fabric trend in adjacent RTT. In some cases LT wraps around adjacent RTT; in other cases RTT and LT appear to represent gradational structural facies of one another. Genetic relations between RTT and LT are a topic of future study.

Shield terrain [7,8]—possibly genetically related to RTT and LT, occurs extensively across NA, and broadly post-dates the formation of adjacent RTT and LT, although lineaments parallel to RTT or LT fabric elements locally cut individual shield structures, presumably the result of structural reactivation. The formation of shield terrain remains elusive, yet critical to understanding Venus evolution.

Geologic mapping to date across the Niobe map area leads us to challenge the widely accepted proposal that lowland RTT represents collapsed crustal plateaus [9-12]. Although the structural fabric of RTT preserved in both crustal plateaus and lowland inliers is similar, as noted in numerous published studies, we have found no evidence and/or relationships that *require* lowland RTT to have once been elevated, or that indicate lowland RTT exposures experienced tectonic collapse. This point seems worth noting given that mechanisms to accommodate crustal plateaus collapse (to accommodate widespread RTT within the lowland) have eluded modeling efforts to date [13-15]. Thus, it is possible that lowland RTT inliers do not represent remnants of crustal plateaus; that is, it is possible that RTT inliers never resided in elevated regional-scale plateaus. This point has implications for models of both RTT and crustal plateau formation, and for Venus evolution. As previously noted [15], RTT occurs across the Niobe map area, including deep basins.

Detailed mapping of RTT reveals a possible new type of structure, concentric ring graben complexes. The best example to date is the structure we call the Haasttse-baad Tessera ring complex (HBRC) [17-18]. These structures, which define parts of circular structures (diameters of 100s to 1000s of km), are defined by steep-sided graben, mrked by singular scarps, which together define nested concentric graben that cut large lacks of lowland RTT. These structures are partially preserved, being visible in RTT fabric, and apparently buried, or otherwise destroyed in the adjacent regions.

Map relations across a wide range of scales indicates that at least across NA, Venus lacks thick (i.e., several km) regionally extensive burial; as a result, the Venus surface preserves an extremely rich geologic record, although delineating details of the local and regional surface histories is a challenging undertaking. As a related point, detailed mapping of fracture suites, graben, pit chains, channels, and flows may provide clues about geological mechanisms through which regional-scale resurfacing processes occur.

Several regionally defined suites of wrinkle ridges are emerging as a result of the mapping efforts. The regionally most extensive suite is concentric to Artemis (Artemis wrinkle ridge suite, AWRS), defining a suite >13000 km in diameter [4]. In northernmost Niobe wrinkle ridge patterns differ from those of the AWRS; the regional pattern of this suite is undefined as it lies mostly north of the NA map area. The AWRS generally postdates the formation of: lowland deformation belts (preserved in Niobe) and lowland circular lows (isolated corona defined by circular topographic lows [18]). Wrinkle ridge suites concentric to Bell Regio and Eastern Eistla Regio, respectively, postdate the formation of the AWRS.

The Diana-Dali coronae-chasmata chain preserves a rich history of interaction with the spatially extensively greater-Artemis structure. The deep chasmata generally post-date the AWRS, with clear evidence of regional truncation of AWRS trends, however, the AWRS deforms some flows mapped as coronae-related flows. Two north-trending coronae chains that extend north of the Diana-Dali corona-chasmata chain are deformed by, and thus predate formation of, AWRS. Volcanic rise Atla Regio, which lies too the east outside the map area, and forms the termination of the Diana-Dali chain, clearly post-dates the AWRS, as Atla-related flows bury AWRS structures.

References: [1] Ford J.P. et al. (1993) JPL Publ. *93-24.* [2] Hansen V.L. (2000) EPSL 527-542. [3] Tanaka K.L. et al. (2005) USGS SIM 2888. [4] Hansen V.L. & A. Olive (2010) Geol., 38, 467-470. [5] Basilevsky A.T. & J.W. Head (1998) *JGR 103,* 8531-8544. [6] Bergmann M. & Hansen V.L. (2013) LPSC, 44, #1542. [7] Aubele J. (1996) LSPC 27, 49-50. [8] Hansen V.L. (2005) GSAB 117, 08-822. [9] Phillips R.J. & V.L. Hansen (1994) AREPS 22, 597-654. [10] Ivanov M.A. & J.W. Head (1996) JGR 101, 14861-14908; [11] Hansen V.L. et al. (1997) Venus II, 797-844. [12] Phillips R.J. & V.L. Hansen (1998) Sci. 279, 1492-1497. [13] Kidder J.G. & R.J. Phillips (1996) JGR 101, 23181-23194. [14] Nunes D.C. et al. (2004) JGR 109(E1), E01006,10.1029/2003JE002119. [15] Hansen & Lopez, 2000. [16] Nunes D.C. & R.J. Phillips (2007) E10002, 10.1029/2006JE2861. [17] Hansen V.L. & López I. (2013) LPSC, 44, #2027. [18] López & Hansen, this vol. [19] Hansen V.L. (2009), USGS SIM 3025.

THE HAASTTSE-BAAD CONCENTRIC RING GRABEN COMPLEX, NORTHERN APHRODITE TERRA (VENUS): GEOLOGIC MAPPING AND MODELS OF ORIGIN. I. López[1] and V. L. Hansen[2], [1]Departamento de Biología y Geología. Universidad Rey Juan Carlos, 28933, Móstoles. Spain (ivan.lopez@urjc.es), [2]Department of Geological Sciences, 1114 Kirby Drive, University of Minnesota Duluth, Duluth, MN 55812 (vhansen@d.umn.edu).

Introduction: Ribbon Tessera Terrain (RTT) constitutes Venus's locally oldest surface unit [1], although globally not all RTT formed at the same time [2,3]. Unit RTT, marked by a distinctive tectonic fabric and high surface roughness, characterizes crustal plateaus but also occurs as lowland inliers—widely interpreted as remnants of collapsed crustal plateaus [4-5]. The RTT tectonic fabric commonly includes short- to long-wavelength folds (1–50 km) that record layer shortening, and orthogonal structures that record layer extension, so-called ribbon structures; flooding accompanies all stages of RTT evolution [6-7]. Graben complexes record the youngest deformation recorded in RTT, typically postdating formation of adjacent short- to long-wavelength folds and ribbons; graben complexes show local embayment, in some cases flooding marks intratessera graben, whereas in other cases graben flood units might be contiguous with adjacent lowland units, including shield terrain. Graben complexes in RTT can define broad orthogonal patterns [6], radial patterns [7], or parallel trends [9]. In this work we present the mapping of a suite of concentric ring graben that postdate, or formed during late stages of, ribbon tessera structure formation in Haasttse-baad Tessera, northern Aphrodite Terra; we provide a initial review of possible forming mechanisms.

Data: Geologic analysis was carried out using NASA Magellan S-band synthetic aperture radar (SAR) and altimetry data [10]. Data include: 1) full resolution (75-100 m/pixel) right- and left-illuminated SAR); 2) Magellan altimetry (8 km along-track by 20 km across-track, ~30-m average vertical accuracy); and 3) synthetic stereo images constructed after [11] using NIH-Image macros developed by D.A. Young. SAR data, obtained via USGS Map-a-Planet website, was viewed in normal and inverted modes.

Description of the feature: The concentric ring graben complex is partially located in Haasttse-baad Tessera (Fig. 1). The composite structure, herein informally referred to as the *Haasttse-baad ring complex (HBRC)*, is composed of a series of well-defined concentric, nested, arcuate troughs that cut local RTT structures, and maintain a spacing of ~10-50 km [12]. These concentric graben differ from RTT graben complexes in that the graben walls, or fault scarps, are singular structures, rather than suites of faults. In addition, the concentric graben, although curved in planform, have significantly larger length:width ratios than graben complexes; concentric graben length depends on the location of the graben, and the along-structure continuity—which is due, in part, to late flooding.

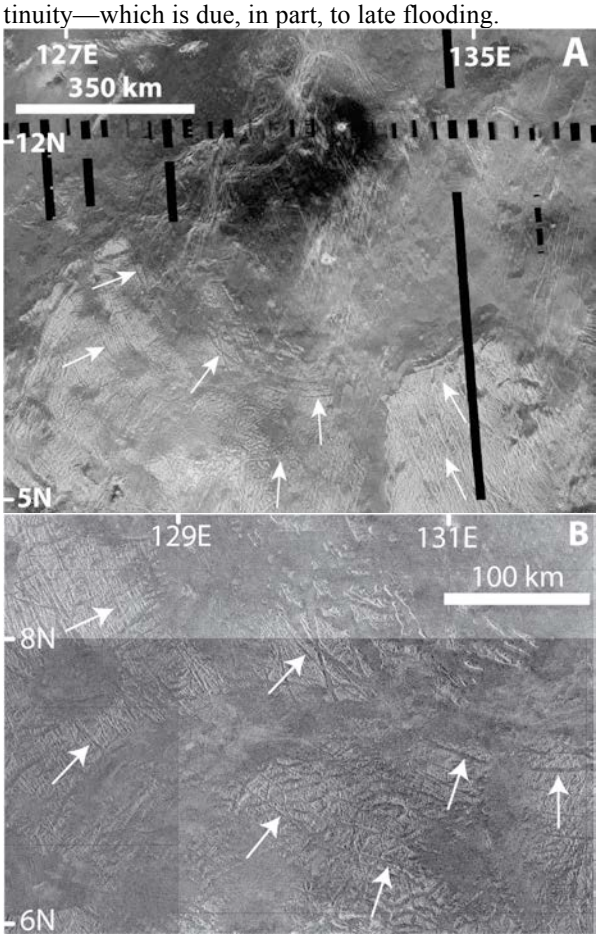

Fig. 1. SAR images of the Haasttse-baad ring complex, with arrows marking the positions of concentric graben; A) southern part; B) SW-quadrant, note simple graben structure.

The *HBRC*, with a diameter >1000 km, is well-defined within its southern half, which cuts Haasttse-baad Tessera (Fig. 1A), but poorly defined in its northern half, where RTT exposures occur only as isolated kipukas in the lowland. Some late, possibly concentric trough structures that cut RTT kipukas north of Haasttse-baad Tessera could be part of the *HBRC*, although the isolated nature of RTT kipukas prevents clear delineation of structural continuity. Concentric graben, which vary in number and spacing, are best developed, or preserved, in the SW and central sections of the structure. In the SE section concentric graben are narrower, discontinuous and are dissected by a suite of

NNW-trending graben that dominantly post-date formation of the concentric graben suite. Previously formed RTT structures in this section of Haasttse-baad Tessera, topographically sited above the central and west sections, also present different trends and degrees of preservation—likely also due to dissection by the NNW-trending graben suite that dominates this area.

Modes of origin: Models proposed for the formation of concentric ring graben structures observed in other planetary bodies can be grouped as related to magmatic (endogenic) and bolide impact (exogenic) processes.

Endogenic models. Concentric suites of extensional structures occur associated with coronae, widely accepted as the surface signature of magmatic mantle diapirs. Coronae, which likely form by this mechanism, occur mostly in chains, although lowland features exist [13]; Coronae are, however, uncommon in association with crustal plateaus, where the thickness of the lithosphere is thought to inhibit a surface manifestation of mantle diapirs [14]. Thus the *HBRC* could have formed after tessera lost subsurface support, or perhaps never had subsurface support to exist as a crustal plateau [15]; however, such coronae typically destroy local RTT fabrics (unpubl. mapping). Additionally, some coronae may represent impact features formed on thin lithosphere [16].

Similar suites of concentric fractures also occur, although at a different scale, related to the formation of volcanic calderas or paterae, wherein a crustal magmatic reservoir is depleted of magma, resulting in collapse of the central block and formation of a downsag caldera accompanied by formation of a concentric ring complex [e.g. Ardnamurchan; 17].

Exogenic models. Similar structures, so called Valhalla-type ring structures, preserved on Jupiter's icy satellites (e.g., Europa's Callanish and Tyre craters; Fig. 2), have been interpreted as multiring impact structures formed by bolide impact in a thin elastic layer that overlies a low-viscosity layer [18-20], which is further underlain by a strong substrate [21]. The number, spacing and morphology of the concentric graben are related to thickness and strength of the elastic layer and crater diameter [21-22].

Discussion: The *HBRC* differs in terms of morphology and size to concentric graben suites formed by endogenic processes. In the case of a corona-scenario, *HBRC* would be a new class of coronae formed exclusively on RTT. There is no evidence for volcanic materials spatially related to the *HBRC* as called for in the emptying of a huge magmatic chamber prior to caldera and volcanic ring complex formation.

On the other hand, formation of the *HBRC* as a multiring impact basin on a strong layer marked by a thin elastic layer above a low-viscosity channel, has strong implications for the geology and crustal structure of the target area, and therefore to the current debate on the origin of both ribbon tessera terrain and crustal plateaus. The possible recognition of a new type of impact crater on Venus is also important for the impact record and the geologic history of Venus.

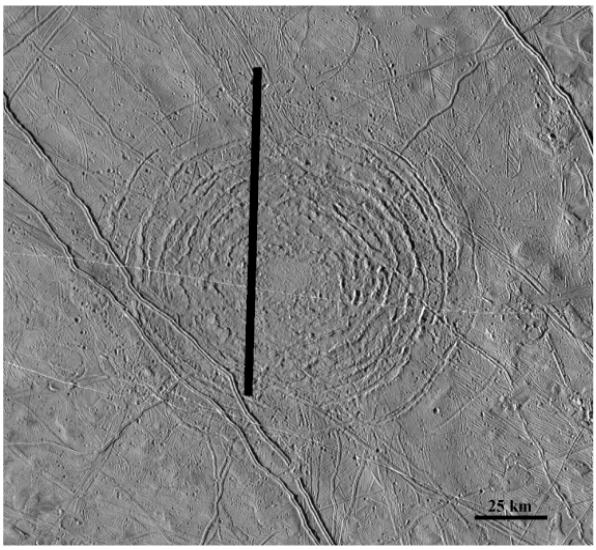

Fig. 2. Tyre crater. Europa.

Conclusions: A large (>1000 km) ring graben complex is located in Haasttse-baad Tessera, Venus. Models for its formation include: a) endogenic origin due to emplacement of a mantle diapir into earlier formed RTT, or caldera collapse on a huge scale, previously unrecognized; and b) exogenic origin by bolide impact on a crust that rheologically consists of a thin elastic layer overlying a low-viscosity (semi-molten?) layer above a strong substrate.

References: [1] Basilevsky A.T. & Head J.W. (1998) *JGR 103,* 8531-8544. [2] Bindschadler et al. (1992) *JGR, 97,* 13563-13577. [3] Hansen et al. (2000) *JGR 105,* 4135-4152. [4] Phillips R.J. & Hansen V.L. (1994) *AREPS 22,* 597-654. [5] Ivanov M.A. & Head J.W. (1996) *JGR 101,* 14861-14908. [6] Hansen V.L. & Willis J.J. (1996) *Icarus 123*, 296-312. [7] Hansen V.L. (2006) *JGR 111*. [8] Ghent R.R. & Hansen V.L. (1999) *Icarus 139*, 116-136. [9] Bergmann M. & Hansen V.L. (2013) LPSC, 44, #1542 [10] Ford et al. (1993) JPL Publ. *93-24.* [11] Kirk et al. (1992) *JGR 97,* 16371-16380. [12] Lang N.P. & Hansen V.L. (2010) *USGS SIM: I-3089*. [13] Stofan et al. (1992) *JGR 97,* 13347-13378. [14] Hansen V.L. & López I. (2013) LPSC, 44, #2027. [15] Bleamaster L.F. & Hansen V.L. (2004) *JGR 109*. [16] Vita-Finzi et al. (2005). *GSA SP 388, 815-823.* [17] Anderson E.M. (1936) *Proc. Roy. Soc. Edinburgh. 56,* 128-156. [18] Moore et al. (1998) *Icarus 135,* 127-145. [19] Moore et al. (2001) *Icarus 151,* 93-111. [20] McKinnon W.B. & Melosh, H.J. (1980) *Icarus, 44,* 454-471. [21] Melosh H.J. (1989) Impact Cratering p.177. [22] Mevél et al. (2001) *C. R. Acad. Sci. Paris, Sciences de la Terre et des planètes / Earth & Planetary Sciences 332,* 217–225.

HIGH-RESOLUTION GEOLOGIC MAPPING IN WEST CANDOR CHASMA, MARS: 2013 STATUS REPORT. C. H. Okubo, U.S. Geological Survey, Flagstaff, AZ 86001, cokubo@usgs.gov.

Introduction: Significant progress has been made on completing four high-resolution geologic maps in west Candor Chasma (Fig. 1). One map entitled, "Bedrock Geologic and Structural Map Through the Central Candor Colles Region of Mars" has been completed and is currently in revision. Results of this mapping are summarized in subsequent sections of this abstract. The remaining three maps are in various stages of completion, and these are planned to be submitted for review by the end of the 2013 calendar year. The majority of the structural orientations have been measured in the southwest Nia Tholus and central Candor Sulci maps. Structural orientations are currently being measured in the Ceti Mensa map. The next steps for the Nia Tholus and Candor Sulci maps are to delineate unit contacts. These units are allostratigraphic, and the bounding unconformities have been largely identified. Thus these two maps should be completed by August, and submitted for review shortly thereafter.

Summary of Candor Colles map: Candor Colles is a population of low, conical hills along the southeast flank of Ceti Mensa, in west Candor Chasma (Fig. 1). Previous geologic maps of the area utilized the relatively low-resolution Viking Orbiter photomosaics (20-150 m/pixel). Geologic maps covering west Candor Chasma were created at scales of 1:15,000,000 [1], 1:2,000,000 [2], and 1:500,000 [3].

The geology of this area has been mapped for the first time at a scale of 1:18,000, using imagery and stereo observations from the High Resolution Imaging Science Experiment (HiRISE) camera. This mapping effort employs high-resolution structural measurements in order to 1) refine the previous unit boundaries in this area established by [2], 2) revise the local stratigraphy where necessary, 3) characterize bedforms to help constrain depositional processes, and 4) determine the styles and extent of deformation to better inform reconstructions of the local geologic history.

Methods: The primary dataset is a pair of stereo HiRISE observations, PSP_001641_1735 and PSP_002063_1735. A digital elevation model (DEM) with 1-m post spacings and orthoimages were created following [4]. Mapping was conducted exclusively within the aerial extent of the DEM. Interpretations of stratigraphic relationships and structure were checked for consistency with other outcrops in the Candor Colles/south Ceti Mensa region using adjacent HiRISE and Context Imager (CTX) observations.

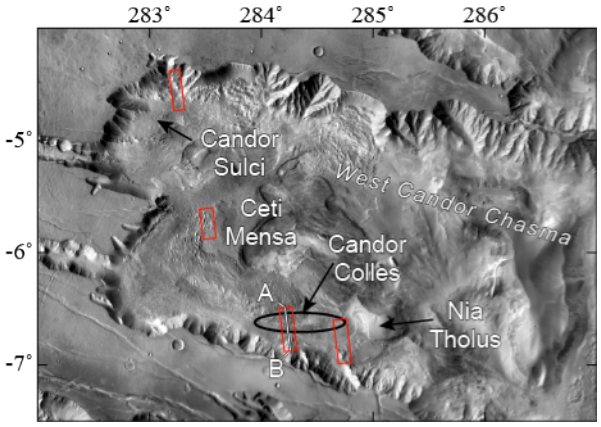

Fig. 1. Locations of the map areas are outlined in red.

Results: The oldest material exposed in the map area is the volcanic rock that constitutes the south wall of west Candor Chasma. The Ceti Labes unit (CeL) consists of landslide deposits derived from the south wall of west Candor Chasma (Fig. 2).

The Candor Colles unit (CaC) buries Ceti Labes. Accumulation of unit CaC occurred within a depositional environment that was at a sufficiently low energy that the primary landslide textures of Ceti Labes were preserved. No facies change between the initial and subsequent sediments of unit CaC is apparent at HiRISE resolution. Deposition was accompanied by occasional erosional events and the formation of numerous local unconformities, but this erosion did not cause extensive modification of unit CeL and apparently did not result in the formation of fluvial channels. Unit CaC was deposited in layers that show onlap and offlap relationships with preexisting topography. Away

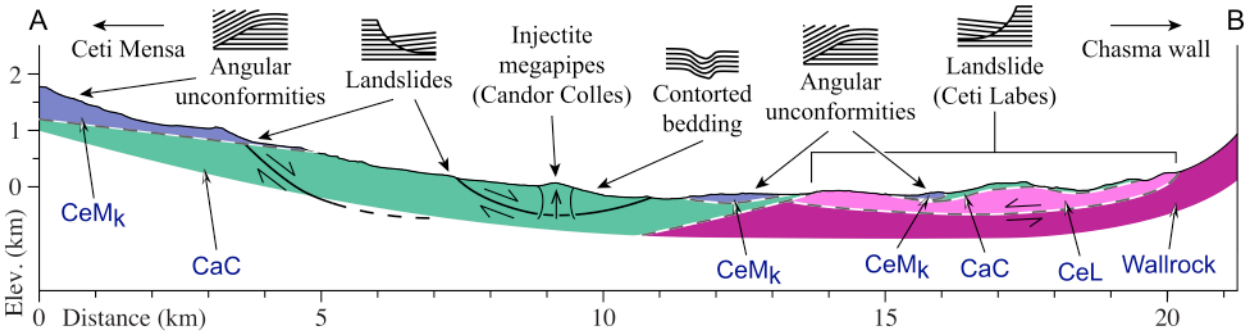

Fig. 2. Synoptic cross-section through the map area. Location of this profile, A-B, is given in figure 1.

from unconformities and deformational features, the layers generally dip toward the south at ~10° or less. Diagnostic fluvial and eolian bedforms at scales of one meter or more are not observed. These findings are consistent with recent interpretations that these deposits accumulated in a sabkha-like environment [5,6].

Unit CaC experienced soft-sediment deformation, leading to formation of contorted bedding and injectite megapipes (i.e., the Candor Colles) [7]. The lack of breccia incorporated into this soft-sediment deformation indicates that unit CaC was poorly lithified at the time of deformation. On Earth, soft-sediment deformation is typically the result of seismic shaking of water-saturated sediments and is common in sabkhas [8].

Unit CaC experienced deformation along major fault zones, which are now exhumed and exposed as high-standing ridges. Crosscutting relationships indicate that slip along these major fault zones was contemporaneous with the formation of the Candor Colles. Thus, these fault zones are the most likely source of the seismicity that drove the soft sediment deformation within unit CaC. The down to the south displacement directions of these fault zones is inconsistent with an origin as chasma-forming faults, which would show down to the north displacements in this part of the chasma (c.f., [9]). Instead, their geometries are most consistent with an origin through landsliding within unit CaC. These fault zones are interpreted as the failure surfaces of landslides that displaced material of unit CaC down toward the south.

The sense of landslide movement indicates that the paleo-topographic slope of unit CaC dipped toward the south at the time of landsliding. Therefore an ancient geomorphic moat between the layered deposits and the south wall of west Candor Chasma, analogous to the present-day moat, existed here when the landslides were active.

Deposition of unit CaC eventually ceased, and erosion of this unit ensued, resulting in the development of an upper bounding unconformity. On-lap relationships with the overlying Ceti Mensa knobby unit (CeM_k) indicate that some of the landslide faults were exhumed at this time as well. Unit CeL also appears to have been re-exposed at this time, because the Ceti Mensa knobby unit also unconformably overlies it. The primary ~2–3-m-scale landslide textures of unit CeL were preserved throughout this erosional episode. Evidence of either fluvial erosion or marine regression is not apparent along this unconformity.

Unit CeM_k was then deposited on top of the regional unconformity at the upper boundary of units CaC and CeL. The onset of deposition occurred in an environment where the sediments accumulated in layers that lap onto preexisting topography. As with unit CaC, this depositional environment was at a sufficiently low energy to preserve the primary landslide textures of Ceti Labes. Units CeM_k and CaC exhibit similar facies characteristics, suggesting that both units were deposited in comparable sabkha environments.

Discussion: The subaerial environment within which units CaC and CeM_k are inferred to have accumulated is consistent with the other inferred geologic processes in the area. Topographically forced wind circulation and eolian erosion is proposed to be the cause of the moats surrounding the mounds of layered deposits in impact craters elsewhere on Mars [10]. Thus an analogous process of eolian erosion within the basin of west Candor Chasma is a plausible mechanism for widespread erosion of these units and development of the proposed paleo-moat and the present-day moat. Such eolian excavation of this moat into unit CaC is a credible process by which extensive, oversteepened slopes could have developed and resulted in landsliding.

The transition from deposition of unit CaC to development of the paleo-moat, subsequent landsliding, and regional erosion can be ascribed to either, or a combination of, a change in wind regime, a decrease in sediment supply, or diminished sediment trapping due to lowering of the water table. This regime eventually reverted to a state that favored sediment deposition, allowing for the accumulation of unit CeM_k. Unlike the Candor Colles unit, major fault zones and soft sediment deformation are not observed within unit CeM_k, possibly because landsliding or other seismic events did not affect this unit while the local ground water table was high.

Deposition of unit CeM_k eventually ceased, and a predominantly erosional environment reemerged. Similar to the erosional event following deposition of the unit CaC, this event was widespread, with no evidence of a fluvial or marine component, and was at a sufficiently low energy to preserve the primary landslide textures of Ceti Labes. Again, eolian erosion is most plausible. This environment presumably persisted into the present-day given the apparent lack of subsequent layered deposits in the area.

Future work: Once all four geologic maps are completed, the collective results of this mapping effort will be used to construct a revised geologic history for west Candor Chasma.

References: [1] Scott, D.H. and Tanaka, K.L. (1986), *U.S. Geol. Surv. map 1802A*, [2] Witbeck, N.E. et al. (1991) *U.S. Geol. Surv. map 2010*, [3] Lucchitta, B.K. (1999) *U.S. Geol. Surv. map 2586*, [4] Kirk, R.L. et al. (2008) *JGR, 113,* E00A24, [5] Murchie, S.L. et al. (2009) *JGR, 114*, E00D05, [6] Andrews-Hanna, J.C. et al. (2010) *JGR, 115*, E06002, [7] Wheatley, D.F. et al. (2013) *LPSC*, abs. 1561, [8] Chan, M. et al. (2007) *AAPG Memoir 87*, [9] Schultz, R.A., and Lin J. (2001) *JGR, 106*, 16549-16566, [10] Kite, E.S. et al. (2013), *Geology, 41*, 543-546.